Cell

Resource

Long-term mesoscale imaging of 3D intercellular dynamics across a mammalian organ

Graphical abstract

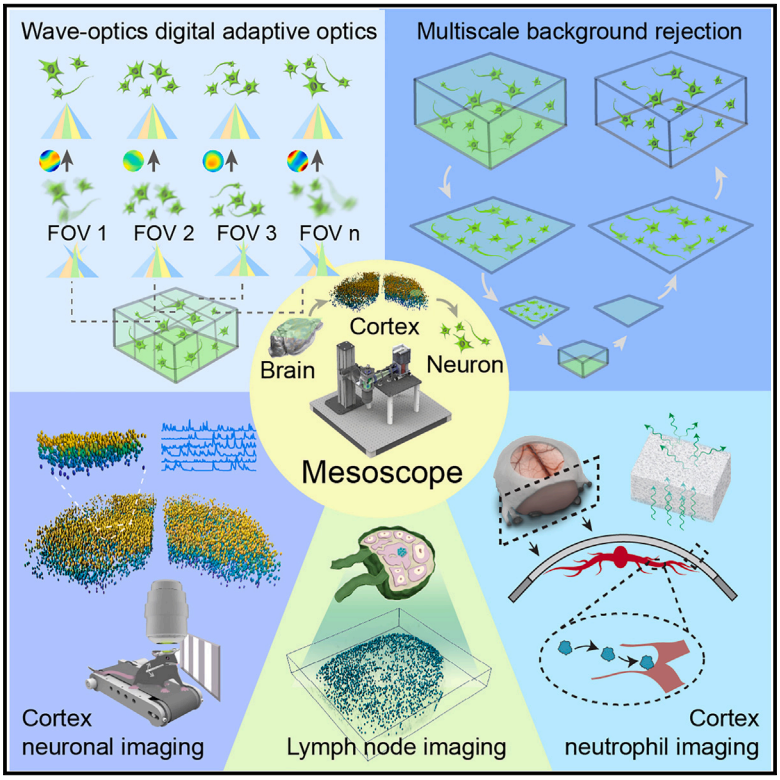

Highlights

- RUSH3D allows long-term, fast 3D imaging at centimeter-scale and single-cell resolution
- Compact, high-fidelity mesoscale imaging is achieved in native intravital environments
- Intercellular interactions across multiple mouse germinal centers are observed *in vivo*
- Cortex-wide multisensory, locomotion neural activities and immune responses are explored in mice

Authors

Yuanlong Zhang, Mingrui Wang, Qiyu Zhu, ..., Jiamin Wu, Zengcai V. Guo, Qionghai Dai

Correspondence

wujiamin@tsinghua.edu.cn (J.W.), guozengcai@tsinghua.edu.cn (Z.V.G.), daiqh@tsinghua.edu.cn (Q.D.)

In brief

RUSH3D, with the integration of multiple computational imaging methods based on a scanning light-field framework, facilitates long-term, high-speed, centimeter-wide mesoscale 3D imaging at single-cell resolution in a compact system for broad practical applications in understanding large-scale intercellular dynamics at the mammalian organ level. We have demonstrated cortex-wide large-population neural recording with cross-day registration during multisensory input, the formation and progression of multiple germinal centers in mouse inguinal lymph nodes, and cortex-wide heterogeneous immune responses after traumatic brain injury.

Zhang et al., 2024, Cell *187*, 6104–6122
October 17, 2024
https://doi.org/10.1016/j.cell.2024.08.026

CellPress

CellPress
OPEN ACCESS

Cell

Resource

Long-term mesoscale imaging of 3D intercellular dynamics across a mammalian organ

Yuanlong Zhang,[1,2,3,4,10] Mingrui Wang,[5,10] Qiyu Zhu,[4,6,7,10] Yuduo Guo,[5] Bo Liu,[6,7,9] Jiamin Li,[4,6,7] Xiao Yao,[4,6,7] Chui Kong,[8] Yi Zhang,[1,2,3,4] Yuchao Huang,[4,6,7] Hai Qi,[6,7,9] Jiamin Wu,[1,2,3,4,*] Zengcai V. Guo,[4,6,7,*] and Qionghai Dai[1,2,3,4,11,*]

[1]Department of Automation, Tsinghua University, Beijing 100084, China
[2]Institute for Brain and Cognitive Sciences, Tsinghua University, Beijing 100084, China
[3]Beijing Key Laboratory of Multi-dimension & Multi-scale Computational Photography (MMCP), Tsinghua University, Beijing 100084, China
[4]IDG/McGovern Institute for Brain Research, Tsinghua University, Beijing 100084, China
[5]Tsinghua Shenzhen International Graduate School, Tsinghua University, Shenzhen 518071, China
[6]School of Basic Medical Sciences, Tsinghua University, Beijing 100084, China
[7]Tsinghua-Peking Center for Life Sciences, Beijing 100084, China
[8]School of Information Science and Technology, Fudan University, Shanghai 200433, China
[9]Laboratory of Dynamic Immunobiology, Institute for Immunology, Tsinghua University, Beijing 100084, China
[10]These authors contributed equally
[11]Lead contact
*Correspondence: wujiamin@tsinghua.edu.cn (J.W.), guozengcai@tsinghua.edu.cn (Z.V.G.), daiqh@tsinghua.edu.cn (Q.D.)
https://doi.org/10.1016/j.cell.2024.08.026

SUMMARY

A comprehensive understanding of physio-pathological processes necessitates non-invasive intravital three-dimensional (3D) imaging over varying spatial and temporal scales. However, huge data throughput, optical heterogeneity, surface irregularity, and phototoxicity pose great challenges, leading to an inevitable trade-off between volume size, resolution, speed, sample health, and system complexity. Here, we introduce a compact real-time, ultra-large-scale, high-resolution 3D mesoscope (RUSH3D), achieving uniform resolutions of 2.6 × 2.6 × 6 μm^3 across a volume of 8,000 × 6,000 × 400 μm^3 at 20 Hz with low phototoxicity. Through the integration of multiple computational imaging techniques, RUSH3D facilitates a 13-fold improvement in data throughput and an orders-of-magnitude reduction in system size and cost. With these advantages, we observed premovement neural activity and cross-day visual representational drift across the mouse cortex, the formation and progression of multiple germinal centers in mouse inguinal lymph nodes, and heterogeneous immune responses following traumatic brain injury—all at single-cell resolution, opening up a horizon for intravital mesoscale study of large-scale intercellular interactions at the organ level.

INTRODUCTION

The grandeur of life is intricately woven by an orchestration of millions of cells, interconnected through a complex network of signaling pathways within their native environment. Observing these intercellular interactions broadens our understanding of the enigma of life at the mesoscale (Figure 1A). Examples abound, such as monitoring of interactions and migrations of immune cells for deciphering immunological responses,[1–3] or tracking of information flow across cortex[4,5] for understanding perception, cognition, and other complex behaviors.[6] Despite differences in morphologies and functions, these phenomena in mice similarly span across near-centimeter scales in three-dimensional (3D) space, weaving together thousands of micron-scale cells to orchestrate a symphony of life.[7] Thus, mesoscopes offering centimeter-scale field-of-view (FOV), single-cell resolution, and 3D imaging capability, along with a physiologically pertinent temporal resolution and low phototoxicity, stand at the fulcrum of intravital fluorescence imaging.[8,9]

However, the challenges are manifold, rooted in both physical limitations of optics and complicated intravital environments, leading to the lack of a generally accessible intravital mesoscope. Firstly, scale-related optical aberrations hinder the optical system's ability to achieve high resolution across a wide FOV.[10,11] Exhaustive optical engineering is required to surmount this physical barrier of space-bandwidth product for incoherent fluorescence imaging.[12–14] Moreover, these approaches remain unscalable to meet the rapidly escalating demand for inspecting larger tissue areas.[15] Secondly, nonuniform distributions of refractive index in tissue generate spatially variant dynamic aberrations, degrading imaging performance[16] and impeding accurate probing of cellular locations and functionality.[17] Conventional adaptive optics methods[18] can correct sample-dependent aberrations but are hard to apply in mesoscale imaging due

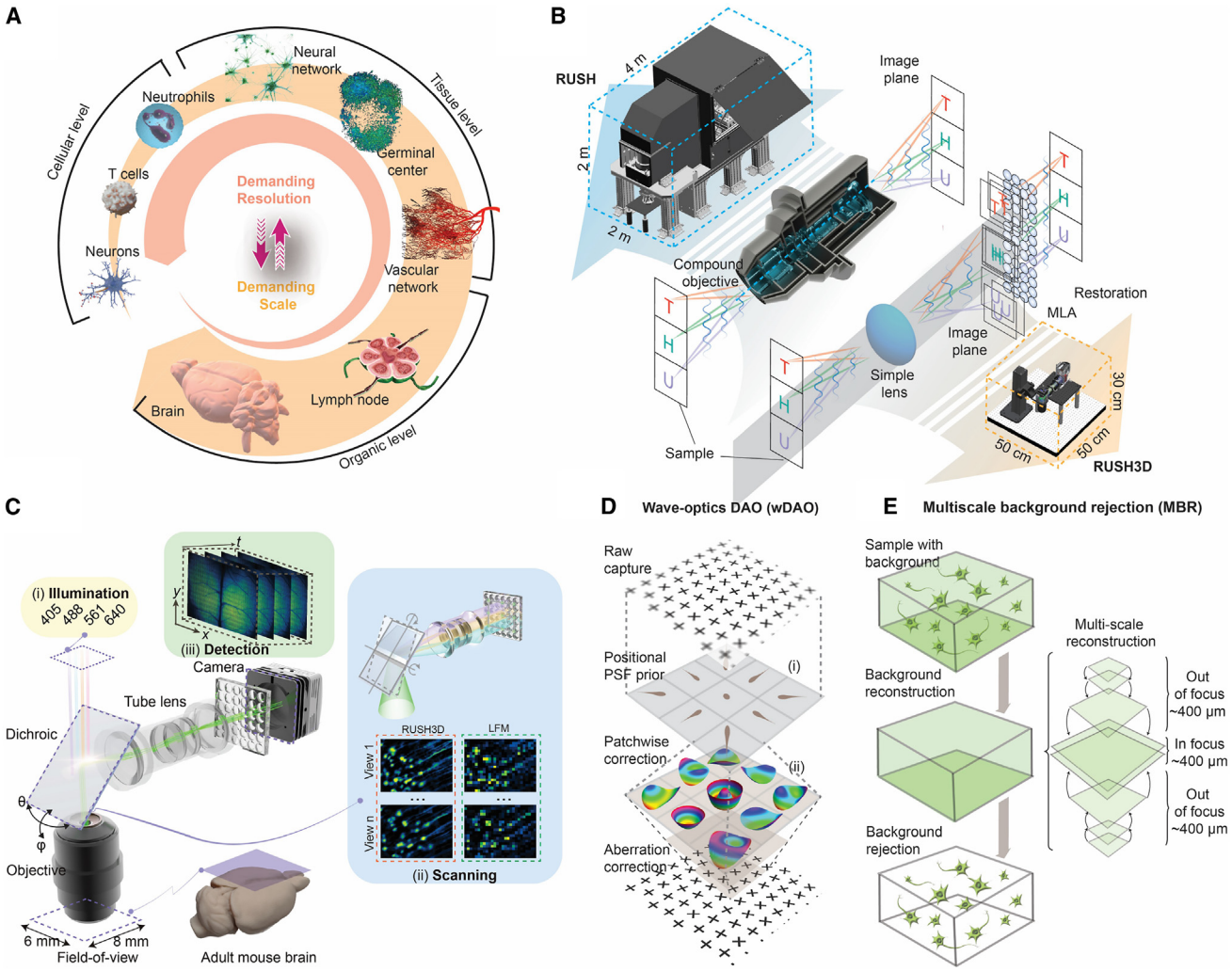

Figure 1. Principle of RUSH3D

(A) Illustration of intravital mesoscale imaging with both high resolution and large FOV.

(B) Comparisons between RUSH and RUSH3D systems.

(C) Optical schematic of RUSH3D.

(D) Implementation of wDAO for multi-site aberration correction.

(E) Pipeline of multiscale background rejection (MBR).

See also Figures S1 and S2 and Videos S1 and S2.

to the small isoplanatic region. Thirdly, background contamination arising from light scattering within piled cells reduces contrasts and fidelity. Although incorporating nonlinear excitations[19] or selective illuminations[7] can alleviate these contaminations, these additions either sacrifice physiologically relevant temporal resolution over large FOV[14] or are hard to be used in mammals.[20] Therefore, feasible design of accessible, reliable, and scalable 3D high-resolution mesoscopy remains a challenge, both conceptually and practically, for unveiling multiscale physiopathological regulations and interactions.

Here, we introduce RUSH3D, a computational intravital fluorescence mesoscope featuring centimeter-scale FOV, high spatiotemporal resolution, 3D resolvability, low phototoxicity, and aberration robustness in complicated environment within a compact, cost-effective framework (Figures 1 and S1; Video S1). Through a systemic integration of multiple techniques including scanning light-field imaging,[21] digital adaptive optics (DAO),[22] multiscale background rejection (MBR),[23] and automatic focus, RUSH3D achieves multiscale imaging in spatial and temporal domains for collective behaviors of thousands of cells across a mammalian organ during diverse physio-pathological states with orders-of-magnitude improvement in data throughput[13,14,24–32] (Figure S1A). Eschewing complex and expensive optical systems in our previous real-time, ultra-large-scale, high-resolution (RUSH) mesoscope,[12] RUSH3D employs ultra-fine measurement of the imaging process of four-dimensional (4D) light fields instead of 2D images with an integrated scanning light-field sensor using off-the-shelf

components[22] (Figure 1B). By developing wave-optics DAO (wDAO), spatially nonuniform system aberrations and environmental aberrations with the root mean square (RMS) error up to 6 wavelengths can be corrected simultaneously without reducing data-acquisition speed. Consequently, RUSH3D achieves a uniform single-cell resolution of about 2.6 × 2.6 × 6 μm^3 across a volume of 8 × 6 × 0.4 mm^3 at 20 Hz over extended periods with two-order-of-magnitude reduction in system size and cost compared with its mesoscopic predecessor.[12]

We demonstrated the fidelity and broad applications of RUSH3D across diverse species, including zebrafish, jellyfish, and mice. In neuroscience, we achieved cortex-wide 3D neural recording at single-cell resolution in mice and developed a sparse-seeded iteration demixing (SSID) algorithm for efficient aberration-corrected neuronal signal extraction. We observed diverse neural dynamics during multisensory interaction and behavior state transition, such as consistent preparatory activities predicting locomotion onset, and investigated cortex-wide representational drift over 3 days. In immunology, we visualized formation processes of multiple germinal centers (GCs) and identified migration of T cells across multiple GCs during immune response with high-speed tracking of tens of thousands of T cells and B cells over 10 h. In pathology, we characterized reverse transendothelial migration of neutrophils following traumatic brain injury (TBI) with cortex-wide aberration-corrected monitoring through a cleared skull. We believe RUSH3D could serve as a generally accessible tool for intravital mesoscale study of large-scale intercellular interactions across a mammalian organ.

RESULTS

Implementation of RUSH3D toward accessible intravital mesoscale 3D imaging

RUSH3D is generally based on the scanning light-field imaging framework[21] to fully exploit aberration robustness for wide-FOV high-resolution 3D imaging within a compact optical system, including an illumination module, a commercial wide-FOV macro objective with a numerical aperture (NA) of 0.5, a tube lens, and an integrated coded light-field sensor (Figures 1C and S1B; STAR Methods). All the lenses are off-the-shelf with optimized separations to reduce the field curvature, making full use of high NA across centimeter-scale FOV.

Since the overall assembly is notably more compact and accessible than previous mesoscope designs,[12] it results in substantial aberrations across the FOV, with wavefront errors exceeding 6 wavelengths RMS in marginal areas (Figure S1C). Such strong spatially nonuniform aberrations are untenable in traditional microscopy, leading to severe degradation in resolution and signal-to-noise ratio (SNR). RUSH3D addresses this problem by ultra-fine measurement and synthesis of 4D spatial-angular light fields instead of 2D images through a coded microlens array integrated on a 48-megapixel complementary metal-oxide semiconductor (CMOS) camera.[22] Rather than shifting the microlens array with a piezo stage, we attached a dichroic mirror on a piezo tip/tilt actuator for high-speed periodic drifting of the image plane, leading to much higher spatial resolution than traditional light-field microscopy (LFM) (Figures 1C and S1B). Temporal resolution can be maintained up to camera frame rate with a temporal sliding window used during 3D reconstruction, as verified before.[21] In this case, RUSH3D can not only achieve high-speed, high-resolution 3D imaging with an extended depth of field but also estimate and correct aberrations at different local regions based on disparities of different angular views after pixel realignment (Video S1). Compared with hardware adaptive optics methods, DAO facilitates multi-site aberration correction in postprocessing without reducing data-acquisition speed, which has been validated in both microscopy[21,33] and photography.[22] Here, we further developed a wDAO pipeline that increases accuracy and efficiency for multi-site aberration correction through a divide-and-conquer strategy (Figures 1D and S1D). Initially, FOV-dependent system aberrations are calibrated via a customized non-rigid registration algorithm, which are incorporated into RUSH3D's wave-optics point spread function (PSF) modeling (Video S2). Subsequently, intravital captures are divided into small patches and deconvolved utilizing aberration-aware PSFs in conjunction with a tailored iterative DAO reconstruction algorithm, effectively removing residual environmental aberrations caused by living tissue (Figure S1E; STAR Methods). wDAO is crucial for high-performance RUSH3D imaging due to its ability to handle large static system aberrations with a single pre-calibration. Compared with our previous geometric-optics DAO, wDAO enhances wavefront-sensing accuracy, reducing RMS wavefront error by over 6 times (Figure S1F), and improves reconstruction fidelity across various noise conditions (Figure S1G).

To mitigate motion artifacts during scanning, we employed the time-weighted algorithm (STAR Methods) based on the prior of spatiotemporal continuity.[21] The effectiveness has been validated by imaging a freely swimming jellyfish, markedly reducing motion artifacts and preserving structural integrity (Figure S1H).

Another factor degrades the imaging performance of intravital mesoscopy is the contamination of background fluorescence. Tilted or coded illuminations in mesoscopes can mitigate these effects but at the cost of axial imaging range[10] or speed.[34] Our previous work has shown that light-field detection facilitates computational optical sectioning by keeping photons focused along different angles with extended depth of fields, which helps distinguish out-of-focus signals from in-focus signals.[23] RUSH3D takes this approach to filter out background contaminations, which we call MBR (Figures 1E and S2A). Given that background signals are primarily low frequency (Figures S2B and S2C), raw measurements are initially down-sampled for a quick large-volume 3D reconstruction to estimate spatially nonuniform backgrounds (Figure S2A). These background signals are then re-propagated to light-field space and subtracted from original images, generating a light-field frame with removed background. MBR can increase data fidelity with enhanced signal-to-background ratios (SBRs), especially for neural activities (Figures S2D–S2H), while maintaining system compactness and high data parallelization for high speed and low phototoxicity.

Characterization of RUSH3D for uniform high-fidelity 3D mesoscopic imaging

Integrating these techniques, RUSH3D offers high-resolution high-speed 3D imaging across an FOV of 8 × 6 mm^2 and a

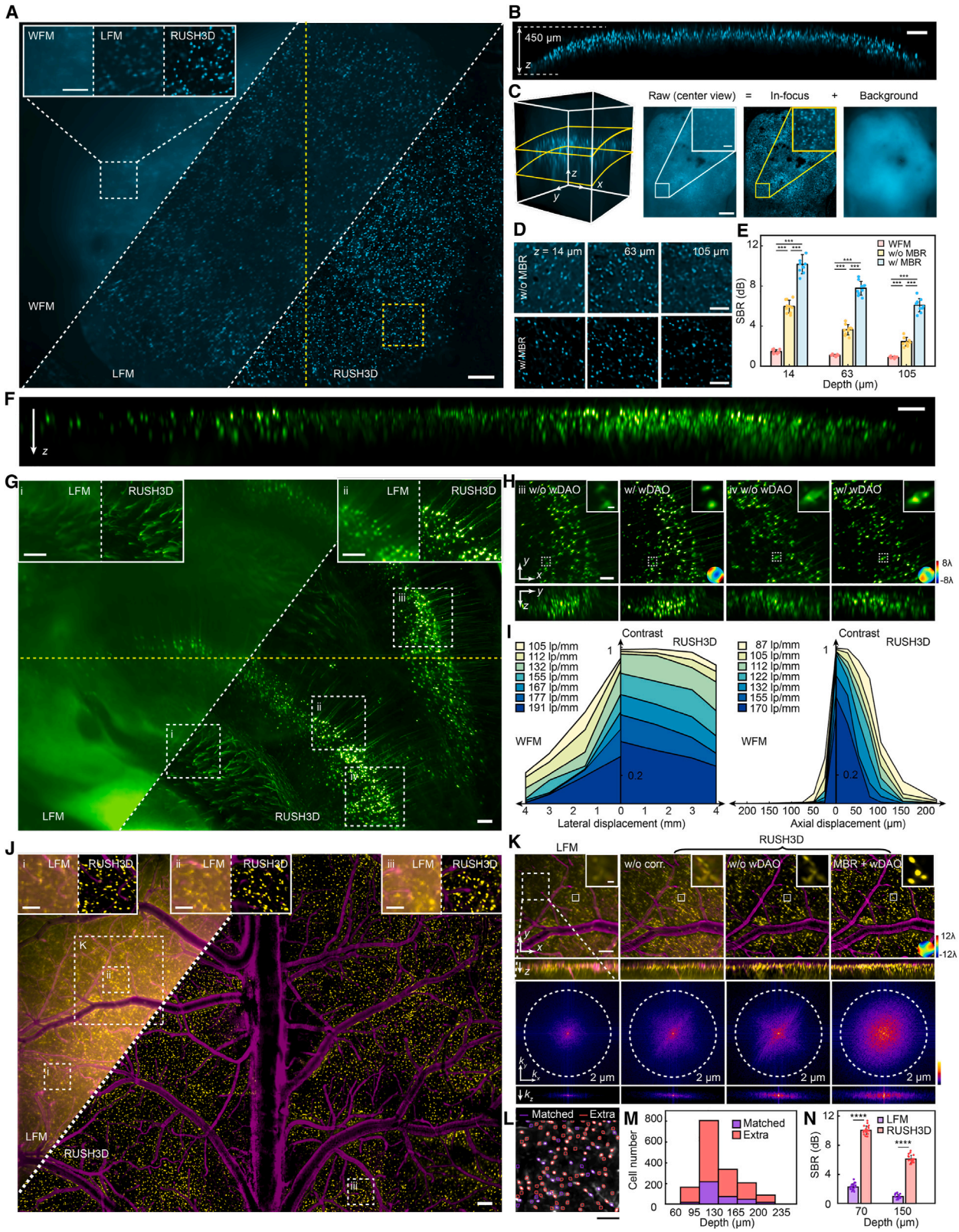

(legend on next page)

0.4-mm effective depth of field in a compact optical system (Figure S2I). We then characterized system performance and fidelity in diverse samples with comparisons among RUSH3D, LFM,[13] wide-field microscopy (WFM), and two-photon microscopy.

We first characterized resolutions by imaging 3D-distributed 500-nm fluorescence beads (Figure S3A). Both lateral and axial resolutions of LFM degrade quickly at the marginal FOV with the increase of system aberrations. Contrastingly, wDAO can effectively correct aberrations and maintain a uniform resolution of 2.6 × 2.6 × 6 μm^3 across the centimeter-scale FOV (Figure S3B). Specifically, considering the effective depth of field as the range within which both lateral and axial resolutions remain within 2-fold of their optimal values, RUSH3D achieved an effective depth of field extending to 400 μm (Figure S3C). Similar performance can be maintained when we injected the beads in mouse brain tissue (Figure S3D). This large depth of field leading to an effective data throughput of 7.4×10^{10} voxels/s, about 13 times higher than our previous RUSH system. To further verify the resolution, we imaged the Siemens star resolution chart with dense structures and calculated modulation transfer functions (MTFs), which accorded well with beads results (Figures S3E–S3G).

Then we compared RUSH3D with WFM and LFM in imaging dense, turbid lymph node tissues, comprising 3D-packed B cells *in vivo* (Figures 2A and 2B). While strong background fluorescence blurred in-focus acquisition of WFM, RUSH3D increased SBR by about 8 dB and achieved better resolution than LFM to resolve single cells across a large depth of field (Figures 2C–2E and S3H). When combined with wDAO, immune cells were well restored even with substantial aberrations of 2.4 wavelengths in RMS (Figure S3H).

We further validated RUSH3D's capability of aberration correction in optically cleared brain tissues labeled with dendrites and axons.[35,36] RUSH3D with wDAO enhanced visibility of subtle structures compared with LFM (Figures 2F and 2G). Without wDAO, both lateral and axial resolutions degraded quickly with reconstruction artifacts (Figure 2H). Analysis on RUSH3D's MTF demonstrated a 32-fold enhancement at the marginal FOV compared with WFM (Figures 2I and S3G). To quantitatively evaluate the accuracy of aberration estimation, we fabricated phase plates and placed them at the pupil plane during imaging of a biological sample to mimic aberrations with known phases. Our findings affirm RUSH3D's proficiency in accurately retrieving the phase distribution, thereby reconstructing specimen's complex structures as if additional aberrations were not present (Figure S3I).

Later, we compared RUSH3D with LFM by imaging vessels and microglia across mouse cortex *in vivo* (Figure 2J). While LFM suffered from strong background and aberrations, RUSH3D overcame these challenges, resolving closely packed cells in 3D (Figure 2K). The analysis of Fourier ring correlation shows similar resolution characterized by fluorescence beads (Figure 2K). Compared with LFM, RUSH3D identified more numbers of microglia by 4 times (Figures 2L and 2M) with improved SBR (Figure 2N). The versatility of RUSH3D extends beyond the aforementioned samples, demonstrated by its efficacy in imaging jellyfish and zebrafish[37,38] (Figures S3J and S3K).

Finally, to perform direct quantitative validation of imaging fidelity, we integrated a two-photon microscope with our RUSH3D (Figure S4A) and conducted temporally interleaved RUSH3D detection with planar two-photon imaging, allowing us to obtain small-FOV two-photon groundtruth data within RUSH3D's axial range (STAR Methods). While RUSH3D captured a much larger volume on the same samples than two-photon microscopy at the same speed, similar structures could be resolved with a structural similarity index (SSIM) over 0.8, indicating strong concordance with two-photon microscopy (Figures S4B–S4D). Both structural and functional fidelities have been validated across different kinds of samples including immunostaining brain slice (Figure S4B), cleared brain tissue over 700-μm depth (Figure S4C), zebrafish larvae (Figure S4D), and

Figure 2. Experimental characterizations and benchmarking of RUSH3D

(A) Comparisons among mesoscopic wide-field imaging (WFM, left), mesoscopic light-field imaging (LFM, middle), and RUSH3D (right) over GFP-labeled B cells in the inguinal lymph node *in vivo*.

(B) The maximum intensity projections (MIPs) of the yellow line marked in (A) (300-μm projection toward *x* direction).

(C) Illustration of MBR procedure. The region of interest (ROI) is identified by the yellow dashed box shown in (A).

(D) Comparisons of reconstructed axial slices with and without MBR in RUSH3D of the yellow box marked in (A).

(E) Bar plots of signal-to-background ratios (SBRs) of WFM (pink), RUSH3D without MBR (w/o MBR, yellow), and RUSH3D with MBR (w/MBR, blue). Mean ± SD. $^{*}p < 0.05$, $^{**}p < 0.01$, $^{***}p < 0.001$, $^{****}p < 0.0001$; ns, not significant; two-sided Wilcoxon rank-sum test. $n = 10$ regions for each.

(F) MIP of *xz* view of yellow fluorescent protein (YFP)-labeled neurons in an optically cleared brain slice with the thickness of about 300 μm obtained by RUSH3D.

(G) Comparisons of *xy* MIPs of the same sample in (F) obtained by LFM and RUSH3D with two zoom-in views.

(H) Comparisons of two zoom-in regions marked in (G) with (w/) and without (w/o) wDAO. Estimated wavefront errors are accordingly overlaid in the bottom right corner.

(I) Modulation transfer functions (MTFs) of WFM and RUSH3D at different lateral displacements (left) and axial displacements (right).

(J) Comparisons of *xy* MIPs of microglia (yellow) and vessels (magenta) in mice obtained by LFM (left) and RUSH3D (right).

(K) Comparisons of a zoom-in region marked in (J) obtained by LFM, RUSH3D without MBR and wDAO (w/o correction), RUSH3D without wDAO (w/o wDAO), and full RUSH3D (MBR + wDAO). Both *xy* and *xz* MIPs are shown with their corresponding Fourier transforms at the bottom.

(L) Comparison of cell segmentation based on the volumes obtained by LFM and RUSH3D. The overlapping cell segments are depicted in purple (matched), whereas cells exclusively segmented by RUSH3D are colored red, denoting additional identification (extra).

(M) Histogram of extra and matched neurons at different depths.

(N) Statistical comparison of SBR of microglia obtained by LFM (purple) and RUSH3D (red) at different depths. Mean ± SD. $^{****}p < 0.0001$, two-sided Wilcoxon rank-sum test. $n = 10$ cells for each method at each depth.

Scale bars: 200 μm (A, B, F, G, and J), 500 μm (C), 100 μm (D, H, L, and zoom-in area in A, C, and J), 20 μm (zoom-in area in H and K), and 150 μm (K).

See also Figures S2 and S3 and Video S1.

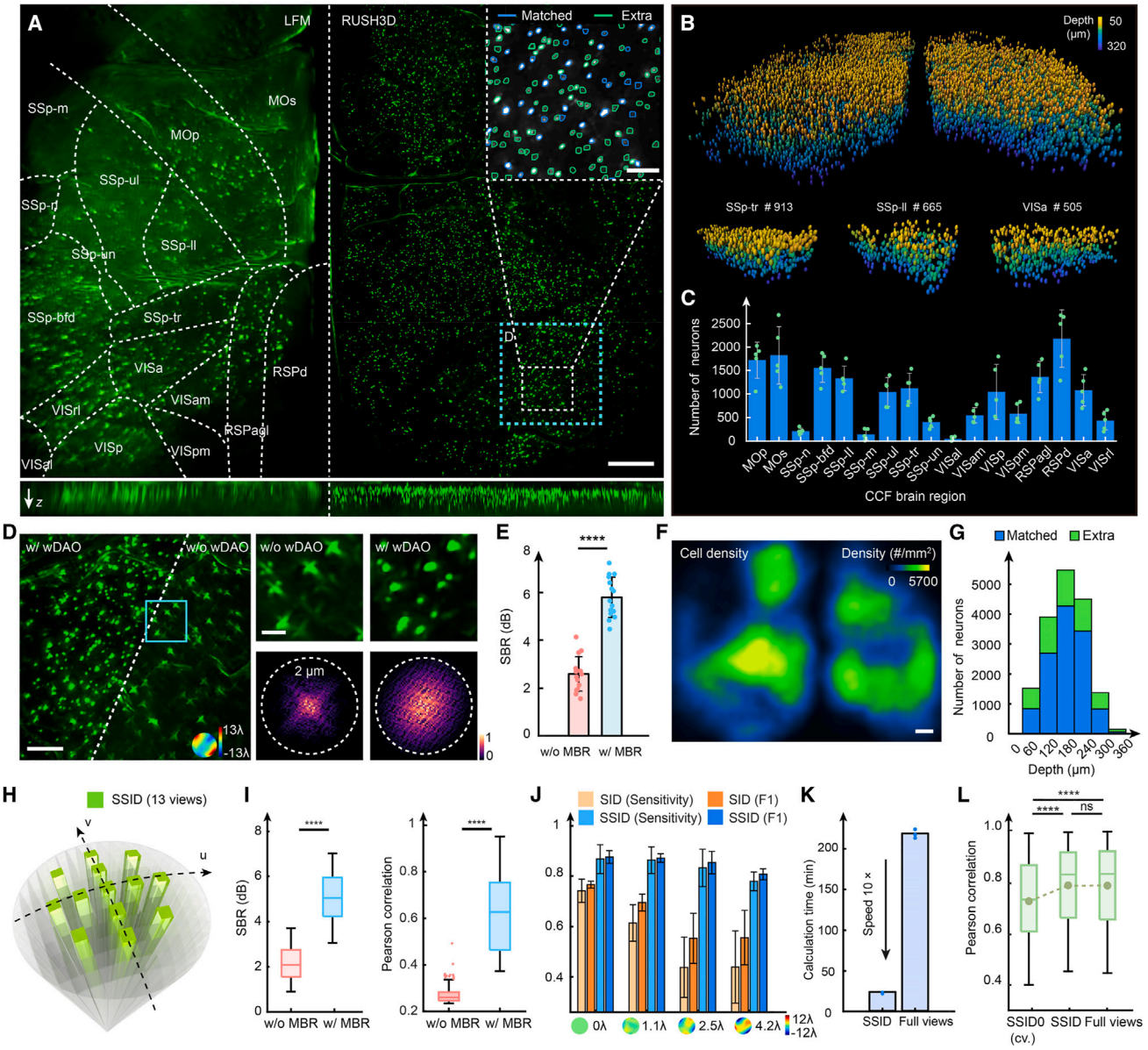

Figure 3. RUSH3D enables efficient large-scale 3D recording of calcium activities at single-neuron resolution

(A) Comparisons of orthogonal MIPs of neuronal population obtained by LFM (left) and RUSH3D (right) in transgenic mice expressing GCaMP6f in layer 2/3 (Rasgrf-dCre/Ai148d). The blue contours in the top right corner breakout represent neurons that are both detected by LFM and RUSH3D (matched), while the green contours represent neurons that are only detected by RUSH3D (extra).

(B) 3D rendering of extracted neurons from (A) by RUSH3D with zoom-in views for three brain regions. Neurons are colored by depth.

(C) Histogram of extracted neuron numbers across 17 cortical regions (n = 5 mice). Mean ± SD.

(D) Comparisons of the zoom-in region marked by the blue box in (A) obtained by RUSH3D with (w/) and without (w/o) wDAO. The estimated wavefront aberration is shown below. Further zoom-in regions for comparison are shown with the Fourier transforms.

(E) Bar plots of SBRs of the reconstructed volume with (w/, blue) and without MBR (w/o, red). ****$p = 3.39 \times 10^{-6}$, two-sided Wilcoxon rank-sum test. n = 15 randomly selected neurons for each. Mean ± SD.

(F) Neuron density map (numbers per mm^2) obtained by RUSH3D.

(G) Histogram of extracted neuron numbers across different depths. The blue bars denote neurons that were identified both in LFM and RUSH3D (matched), whereas the green bars denote neurons that were exclusively identified in the RUSH3D (extra).

(H) Illustration of sparse SID (SSID) neuron extraction algorithm utilizing only sparse views.

(I) Signal-to-background ratio (SBR, left) and correlation score (right) characteristics of SSID improvement with MBR. n = 20 and 357 neurons for SBR and correlation comparison, respectively. ****$p < 0.0001$, two-sided Wilcoxon rank-sum test. Central line inside the box: median. Box: interquartile range. Whiskers: maximum and minimum. Outliers: individual data points.

(legend continued on next page)

neural activities in mice cortex (Figures S4E–S4N), underscoring RUSH3D's capability in high-fidelity imaging with much higher data throughput.

Efficient large-scale cortex-wide 3D neuron extraction

Inter-area communications in mammalian neocortex are crucial for information processing.[39,40] Given that different cortical regions receive and transmit diverse synaptic inputs and outputs, long-term 3D simultaneous measurement of cortex-wide neural activities is critical.[41] Yet, achieving this with high fidelity has been hindered by aberrations, background fluorescence, low resolution, and phototoxicity. We demonstrate that RUSH3D can overcome these limitations, enabling high-throughput, high-speed single-neuron 3D recording of most dorsal cortex with low excitation power.

We conducted head-fixed imaging on layer-2/3-specific transgenic mice with GCaMP6f labeling across 17 cortical regions, delving to a depth of 320 μm beneath the dura at 20 Hz (Figures 3A–3C; Video S3). RUSH3D with wDAO effectively achieved single-neuron resolution at high fidelity across cortex-wide FOV (Figure 3D), while LFM suffered from low resolution, leading to strong crosstalk for densely labeled neurons (Figures S5A and S5B). Moreover, RUSH3D's MBR further increased SBR in both spatial (Figure 3E) and temporal (Figure S5C) domains, reducing crosstalk between adjacent cells and allowing identification of 3.6 times larger number of neurons (Figures 3F, 3G, and S5D). Such comprehensive neuronal access at single-trial level across different brain regions is vital for the study of coding mechanisms of neuron populations,[42] learning,[43] and memory.[44]

Given RUSH3D's simultaneous recording for tens of thousands of neurons, conventional frame-by-frame LFM reconstruction would require substantial computational resources. The recently developed seeded iteration demixing (SID) algorithm[13,45] extracts neuronal signals in unreconstructed light-field space, refining neural footprints and temporal traces iteratively. Yet, SID heavily relies on unbiased neuron reconstructions for seed generation, making it susceptible to aberration-induced errors (Figure S5B), and still requires large computational costs. For instance, a 10-min RUSH3D recording took over 80 h with SID processing in a standard workstation. To bypass these limitations, we developed a sparsity-enhanced algorithm, termed SSID, to increase performance and efficiency of large-scale 3D neuron extraction (Figure S5E). Rather than using complete phase-space representations for extraction, we harnessed an optimized dilated seed generation pattern, exploiting the inherent data redundancy in phase space (Figure 3H). MBR is performed initially, followed by motion correction and wDAO for precise estimations of high-resolution 3D footprints (Figures S5B–S5D).

We first assessed the performance of SSID pipeline in virtual realistic brain imaging by neural anatomy and optical microscopy (NAOMi) simulator[46] for quantitative validation, where we identified the increase in SBR and correlation scores compared with previous method (Figure 3I). Furthermore, we incorporated optical aberrations inferred from *in vivo* imaging of mouse brains across an 8 × 6 mm^2 FOV to align simulations with practical data closely. We found SSID greatly reduced background disturbances and aberrations across all FOV (Figure S5F). As a result, SSID outperformed SID in neuronal segmentation precision (0.87 ± 0.03 compared with 0.79 ± 0.04, mean ± SD, n = 12) and sensitivity (0.83 ± 0.06 compared with 0.56 ± 0.16, mean ± SD, n = 12, Figure 3J). High fidelity can be maintained with fewer views used in SSID, thereby enhancing processing speed by nearly 10 times (Figures 3K and S5G). Extracted neuronal traces correlated highly with the ground truth (0.79 ± 0.15 correlation scores, mean ± SD, n = 1,237 neurons, Figure 3L).

To further evaluate SSID's fidelity in experimental data, we used our hybrid RUSH3D and two-photon microscope to image transgenic animals expressing layer-2/3-specific GCaMP6f calcium indicators (Figures S4A and S4E), where fast alternation between one and two-photon excitation enabled nearly simultaneous acquisition of RUSH3D signals and two-photon groundtruth data (STAR Methods). Results showed high consistency in neuron locations and temporal traces across both modalities (Figure S4E), with a temporal correlation of 0.86 ± 0.12 (mean ± SD, n = 1.361 neurons, Figure S4F). Such high fidelity of RUSH3D is consistent across multiple cortical regions (Figures S4F–S4H).

Additionally, we integrated an electrically tunable lens into the two-photon path to evaluate the fidelity at various cortical depths without changing the focal position of RUSH3D (Figure S4I; STAR Methods). The analysis revealed a decrease in temporal correlation with increasing penetration depths but maintained a correlation score of 0.83 ± 0.17 (n = 430 neurons, mean ± SD) with the two-photon groundtruth ranging from 100 to 200 μm and RUSH3D focusing at 150 μm (Figure S4J). The accuracies of RUSH3D's neuronal detection across these depths were also quantified as 0.81 ± 0.05 (n = 5 sessions across 2 animals, mean ± SD, Figure S4K), and the proportion of neurons identified compared with the two-photon data indicated a sensitivity mean of 0.73 ± 0.09 (n = 5 sessions across 2 animals, mean ± SD).

We further compared orientation-tuning characteristics of visual cortical neurons captured by RUSH3D and two-photon imaging simultaneously (216 paired neurons across n = 3 animals in the V1 region). Of these, 44 neurons (20.4%, which is similar to previous study using GCaMP6f[47]) were significantly tuned to drifting-angle stimuli (p < 0.05, two-sided Wilcoxon

(J) Statistical analysis comparing the sensitivity (shallow color) and F1 score (deep color) of neuronal segmentation between SSID (blue) and SID (orange) across four distinct aberration conditions, each indicative of varying positions from the center to the periphery of the FOV. n = 3 samples for each condition. Symbols as in (E).

(K) Characteristics of calculation time reduction through SSID. Mean ± SD.

(L) Characteristics of signal fidelity of SSID. Three boxes represent neuronal demixing only with the central view (cv., SSID0, left), with SSID (middle), and with full views (right). ****p < 0.0001, ns, not significant, two-sided Wilcoxon rank-sum test. n = 1,237 neurons from 3 simulated movies. Symbols as in (I).

Scale bars: 500 μm (A and F), 200 μm (D), 100 μm (zoom-in area in A), 50 μm (zoom-in area in D).

See also Figures S4 and S5 and Video S3.

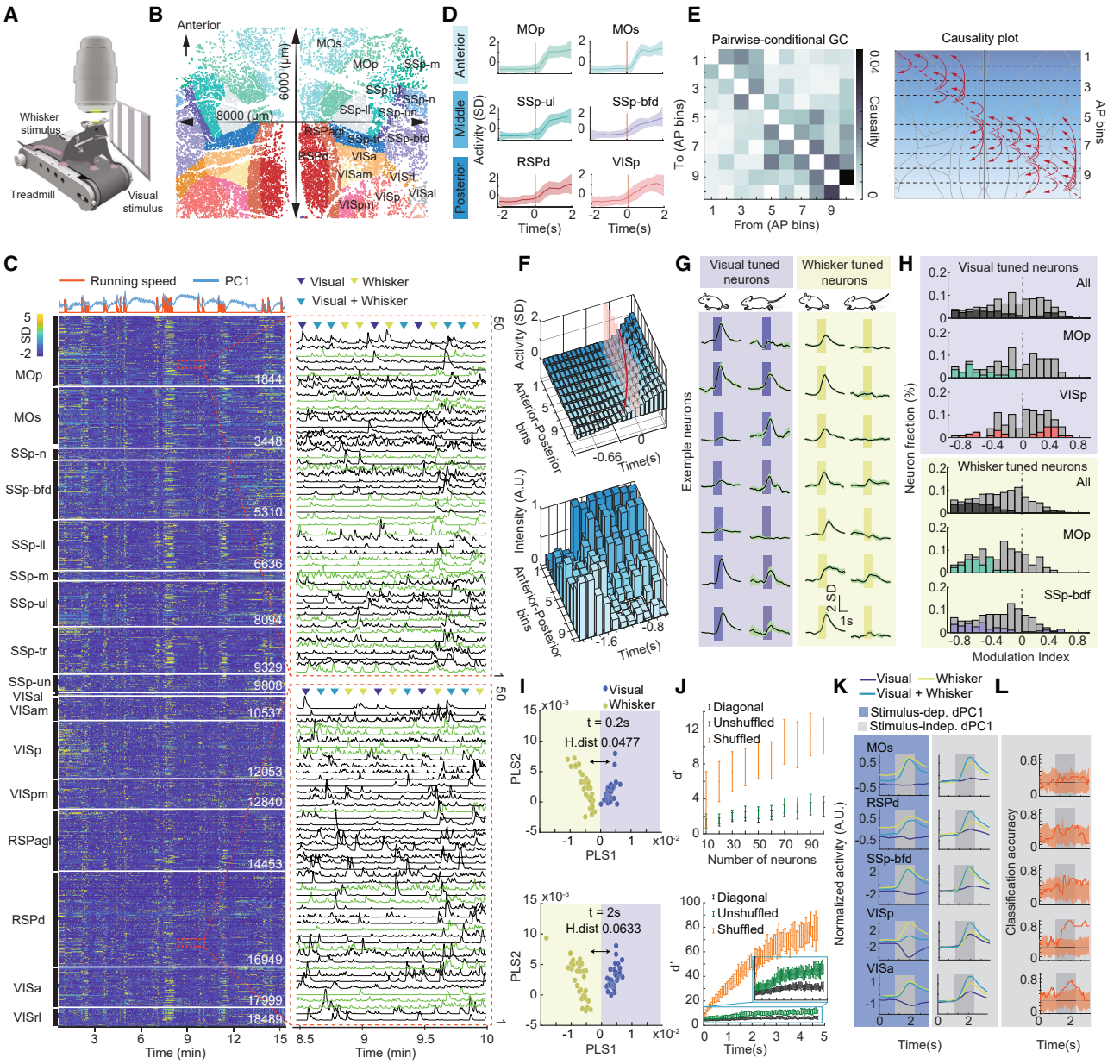

Figure 4. Preparatory processing and visual-tactile responses across multiple brain regions

(A) Experimental schematic showing calcium imaging during self-initiated running with visual and whisker stimulation.

(B) Example spatial footprints of extracted sources with RUSH3D. Different colors represent different cortical regions.

(C) Heatmaps of temporal signals extracted from a 15-min recording. Top traces are the animal speed (running speed, red) and the first principal component of neuronal activities (PC1, blue). Two zoom-in panels show example calcium traces (each with 50 neurons). Inverted triangles mark the delivery of the stimulus.

(D) Peri-running time histograms (PRTHs) of 6 cortical regions from the anterior (top), middle (middle), and posterior (bottom) sections of the cortex. Trials are aligned to locomotion onset (red vertical line). n = 12 episodes. Shaded area represents mean ± SD.

(E) Left, matrix of Granger causality between each pair of 10 cortical bins during the running state (n = 33 episodes from 3 mice). The first column is the causality from the most anterior bin to the other 9 bins. Causality with $p < 0.05$ (Granger F test) was shown after correction for multiple comparisons to control false discovery rate. Right, summary of causality between cortical bins. Red arrows indicate inferred causality direction.

(F) Top, bar plots of neuronal activities at each time point and anterior-posterior position. The red line is cubic interpolation of (bin, time) coordinates, which represents the normalized neuronal activities of a bin reached 0.3. The transparent pink wall marks the start of running. Bottom, bar plots of spatiotemporal motifs calculated by seqNMF (cross-validation significance test, $p < 0.05$). x axis is time aligned to the running onset.

(legend continued on next page)

rank-sum test). Both methods show similar tuning curves at the single-cell level (Figure S4L). Orientation amplitudes, calculated from averaged stimulus-evoked activities, were also highly correlated (Figure S4M). Additionally, the histogram of orientation selection index (OSI) by both methods showed similar distributions for these neurons (Figure S4N).

Both numerical and experimental validations, spanning from neuronal spatial locations, temporal responses, and neural functional statistics, demonstrate that RUSH3D can capture cortex-wide large-scale neural population dynamics with high fidelity comparable to two-photon microscopy in layer-2/3 cortex.

Cortex-wide neural responses at single-cell level with multisensory input

With the capability of multi-regional chronic neural recording, we explored cortical patterns of genetically defined populations of neurons underlying multiple behavioral conditions. We first employed RUSH3D to image cortical activities in awake, head-fixed mice that exhibited brief spontaneous locomotion on a treadmill (Figure 4A). Mice were presented whisker and visual stimuli separately or in combination. Leveraging the increased speed of SSID, RUSH3D proficiently accomplished 3D neuronal extraction of 18,489 cortical layer-2/3 neurons across 17 cortical areas from 14,000 frames in an example mouse within several hours (Figure 4B). Strong correlations between neuronal activities and animal behavioral states (e.g., running) can be observed (Figure 4C).

We examined the impact of locomotion activity on neural activities across various cortical regions, with a focus on fluorescence changes tied to the running initiation. Peri-running time histograms (PRTHs) showed several regions experienced substantial increases in calcium activities even before the running onset (Figures 4D and S6A). The quick rise of pre-running activity in posterior areas (primary visual cortex, retrosplenial cortex, etc.) indicated that these areas might receive strong excitatory inputs prior to running (Figure S6B). Granger causality analysis[48] showed that activity in posterior regions preceded activity in other areas (Figure 4E), suggesting their possible role in initiating cortex-wide preparatory activity for driving spontaneous locomotion. To corroborate this, we examined average activities across different cortical positions (Figure 4F) and employed seqNMF[49]—an unsupervised algorithm for temporal sequence discovery—to uncover repeated spatiotemporal patterns (“motifs”) of cortical population activity fluctuations and waves. We discovered a major motif originating from the posterior side and spreading toward the anterior side during preparatory processing (Figure 4F). This indicates that the posterior cortical regions might play a crucial role in initiating cortical waves during this stage.

We then investigated how locomotion modulated sensory processing and how visual and tactile stimuli interacted in different cortical areas (Figures S6C–S6F). We identified a considerable number of stimulus-activated neurons that were substantially inhibited during locomotion, particularly in the primary motor cortex (Figures 4G, 4H, and S6E). Conversely, visually tuned neurons in primary visual cortex demonstrate opposing distributions, with the majority showing enhanced activity (Figure 4H). Following stimulus presentation, whisker and visual stimulus-evoked ensembles are increasingly distinguishable, as analyzed through partial least squares (PLS, Figure 4I). The discriminability index d'[24] plateaued quickly both in time (2 s after stimulus onset) and size of neuron ensemble (50-neuron ensemble, Figure 4J), with shuffled datasets even more distinguishable, indicating that correlated noise degrades stimulus representations in the unshuffled data.[24] In our analysis of neurons modulated by both whisker and visual stimuli, we discovered their responses were generally inhibited during coincident stimulus events, as demonstrated in whisker-tuned neurons during visual trials and vice versa (Figure S6F). We further applied demixed principal-component analysis (dPCA)[50] on single-trial data (Figure S6G), revealing distinct response patterns in certain brain regions (Figure 4K). Specifically, we found that the primary visual cortex (VISp) showed the maximum difference in time-dependent classification accuracies during simultaneous visual and whisker stimuli, suggesting asymmetric sensory processing roles in different brain areas (Figure 4L).

In conclusion, RUSH3D has revealed that cortical activity waves contingent on locomotion onset propagate from the posterior cortical regions toward anterior regions (Figures 4A–4F). The study also differentiated dynamic circuit ensembles in cortical areas corresponding to whisker and visual input, which were modulated by running state or sensory interaction

(G) Examples of visual (left) and whisker (right) tuned neurons responding to running modulation. Visual and whisker stimuli are presented as purple and yellow shaded regions, respectively. Trial numbers involving visual stimuli during locomotion and quiescence were 7 and 34, respectively, while those involving whisker stimuli during these conditions were 14 and 37, respectively. Shaded area represents mean ± SD. 7 example neurons are presented for each stimulus.

(H) Top, histogram of running modulation index of visual-tuned neurons in all imaged cortical regions (top), MOp (the primary motor cortex, middle), and VISp (bottom). The shallow gray bars represent all neurons that are activated by the stimulus (n = 625 cells in total across 3 mice), while color bars indicate activated neurons significantly modulated by running ($p < 0.05$, two-sided Wilcoxon rank-sum test). Bottom is the same as the top but for whisker-tuned neurons (n = 1,516 cells in total across 3 mice).

(I) Neural ensemble responses at 0.2 s (top) and 2 s (bottom) after stimulus onset in the two-dimensional space derived by partial least squares (PLS) analysis. Blue and red dots represent individual trials (34 trials per stimulus). The Hausdorff distances (H.dist) of different stimulus are labeled.

(J) Top, the mean values of discriminability index d' over the number of cells. The d' was calculated at 1 s after stimulus onset. Bottom, d' for experimental data (green), trial-shuffled data (orange), and diagonal discrimination (black, which ignores response correlations between neurons) are calculated by cumulative decoding over time after stimulus onset. n = 280 neurons. Error bars: SD.

(K) The first demixed principal components (dPC1) of visual (purple), whisker (yellow), and combined visual whisker stimulus (blue) of 4 cortical regions (4 rows). The left column represents stimulus-dependent dPCs, and the right column represents stimulus-independent dPCs.

(L) Cross-validated time-dependent classification accuracies of linear classifiers (black lines) given by the first visual stimulus dPC in each cortical region (rows). Shaded gray regions show the distribution of classification accuracies expected by chance as estimated by 100 iterations of the shuffling procedure.

Scale bars: 2 SD (G) and 1 s (G).

See also Figure S6.

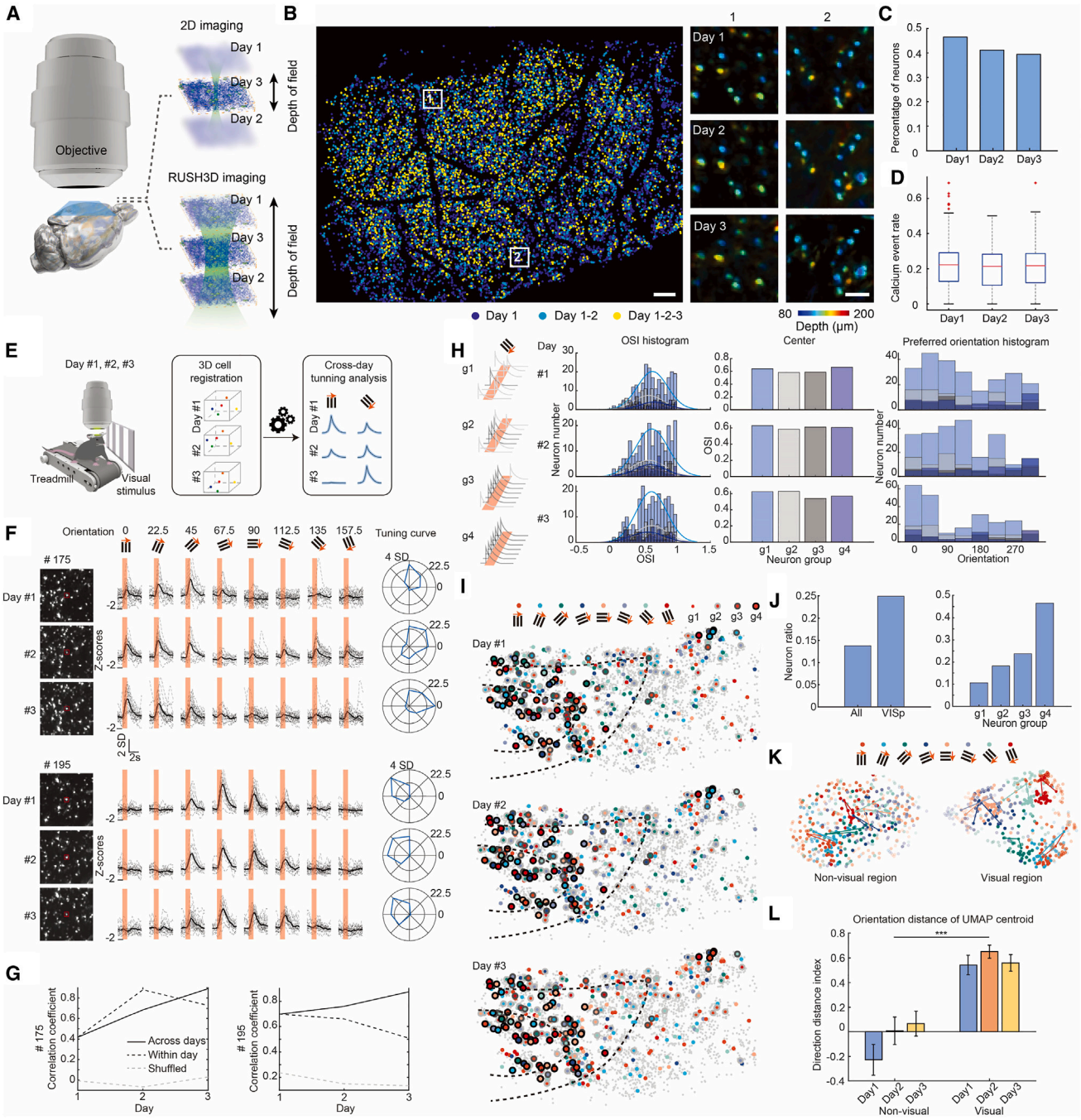

Figure 5. Cross-day visual representational drift across multiple brain regions

(A) Illustration of cross-day neuron tracking ability of RUSH3D due to the extended depth of field, in contrast to traditional WFM.

(B) Distribution of registered neurons across days. Left, neurons that were tracked on different days are colored differently. Right, two zoom-in regions outlined by white boxes in the left showing depth-color-coded neurons registered across 3 days (3 rows).

(C) Bar plot of the fraction of tracked neurons on each day of 3 consecutive days.

(D) Boxplot of calcium event rates of all tracked cells at different days. Central line inside the box: median. Box: interquartile range. Whiskers: maximum and minimum. Outliers: individual data points.

(E) Experimental setup showing calcium imaging in head-fixed mice during self-initiated running with structured visual stimulation in consecutive 3 days.

(F) Moving grating stimulus-evoked activities across 3 days of 2 exemplary neurons. Left: MIP of tracked neurons in 3 days. Middle: grating stimuli-evoked activity in 3 days. Dotted lines show activity in each trial, and the solid line shows average activity. Orange shaded area indicates the stimulus epoch. Right: radar plot of tuning properties of exemplary neurons in 3 days. The outer ring represents 4 SD.

(legend continued on next page)

(Figures 4G–4L). Our study underscores RUSH3D's superior ability to simultaneously capture cortex-wide and high-resolution neural dynamics, which may provide invaluable insights into long-standing questions surrounding sensory-motor coordination, perceptual learning, decision-making, etc.

Cross-day visual representational drift across multiple brain regions

Neural activities exhibit notable plasticity, adjusting in response to variations in internal states and environmental stimuli. Thus, tracking the neural dynamics of the same set of neurons across sessions spanning multiple days is highly desirable in neuroscience research. Equipped with 3D imaging capabilities across a large FOV, RUSH3D facilitates cross-day tracking of the same set of neurons, regardless of incidental axial shifts due to animal positioning (Figure 5A). An example experiment was performed to track over 3,000 neurons in the half-hemispheric cortex across a 3-day period (Figure 5B). Detection of these neurons demonstrated noteworthy stability across this duration (Figure 5C), and their firing rates displayed consistency (Figure 5D), suggesting that mice maintained analogous physiological states.

Employing this capability for cross-day and cross-session neuronal registration, we further examined visual-stimuli-evoked responses across multiple days (Figure 5E). Neuronal responses exhibited varying degrees of consistency across days, demonstrating both similarity and dissimilarity (see two representative neurons, Figure 5F). We randomly split trials into two halves and calculated their correlation, and discovered that the grating responses within a day (r_{within}) and across days (r_{across}) were marginally alike, signifying that visual responses exhibit temporal stability (albeit there was inherent representational drift over time, Figure 5G). To further scrutinize the stability across days, we partitioned the responsive neurons into four groups, ranging from low to high response stability to grating stimuli (g1–g4 in Figures 5H and S6H). We observed that each group of neurons exhibited a mean OSI situated around 0.5, irrespective of daily drifts (Figure 5H).

Benefiting from the large FOV of RUSH3D, we tracked responsive neurons distributed throughout cortical areas, not only confined to the visual cortex. We observed daily variations in the distribution of orientation-preferred neurons (Figure 5I). Statistically, visual stimuli activated a higher proportion of neurons in the primary visual area (25.0%, which is similar to previous study using GCaMP6f[47]) compared with all regions together (14.3%) (Figure 5J), and neurons with robust responses to visual stimuli are concentrated in the primary visual area (Figure 5J). To compare the population decoding capability of responsive neurons in the visual and non-visual areas, we reduced the dimension of trials using uniform manifold approximation and projection (UMAP) (Figure 5K). Neurons responsive in the visual area unambiguously differentiated individual grating trials that persist across 3 days, in sharp contrast to neurons in the non-visual area. We noted that the orientation distance index based on UMAP distribution, a key measure of decoding capability, was substantially higher in the visual area compared with the non-visual area, further emphasizing the distinction between the visual and non-visual regions (Figure 5L). The efficacy of RUSH3D in documenting cell population change reveals regional heterogeneity in visual responses across multiple days.

Long-term, high-speed 3D observations of multiple GCs at single-cell resolution

Interactions between T cells and B cells play a pivotal role in shaping most humoral immune responses, demonstrating protective attributes in response to vaccination or infection, or alternatively, inducing detrimental effects such as autoimmunity, allergy, or transplant rejection. For the establishment of enduring humoral immunity, GCs function as indispensable foci within secondary lymphoid organs, accommodating mitotically active cells wherein B cell clonal expansion, somatic hypermutation, and affinity-based selection transpire. Recent strides in intravital observation of GCs have unveiled the potential for direct examination of key dynamic characteristics of each GC. However, the correlation between cellular movement and affinity maturation across multiple GCs at the lymph node level remains elusive, attributable to the lack of mesoscale high-speed 3D imaging devices. RUSH3D proficiently fills in this gap.

To investigate mesoscopic dynamics of immune cells, we imaged the inguinal lymph node with RUSH3D over a long term.[51,52] Due to the morphological changes of the lymph node during immune response, we developed an auto-focus algorithm to compensate focal drifting with real-time depth estimations

(G) Correlation coefficients of the exemplary neurons in (F), derived by comparing visual response to moving gratings on odd and even trials from a single recording session (black dot line), two recording sessions from different days (black solid line), or after shuffling the stimulus order (gray dot line).
(H) Orientation selectivity index (OSI) and the preferred orientation distribution of 4 responsive neuron groups (g1–g4) across 3 days. The four distinct groups of neurons are selected based on their response reliability to grating stimuli. The "g4" neuronal group displayed the highest consistency in response, while the "g1" group exhibited the lowest. Left: OSI histogram of 4 groups of neurons. Middle: mean OSI value for the 4 groups of neurons. Right: distribution of neurons that were preferentially activated by gratings at each moving orientation in 4 groups.
(I) Distribution of orientation-selective neurons across 3 days. Gray dots are cross-day registered non-responsive neurons. Colors indicate the preferred orientation of responsive neurons. Circle sizes indicate different neuron groups. Dashed lines outline the primary visual cortex (the inner one) and the boundary between the visual and non-visual areas (the outer one).
(J) Fraction of visual-responsive neurons. Left: fraction across all recorded cortical areas versus that in the primary visual cortex. Right: fraction for the 4 groups of neurons in the primary visual cortex.
(K) UMAP distribution of decoded orientation based on population activity in non-visual areas (left) or in visual (primary and higher-order) areas (right). Color transparency indicates different days, with the first day having the lowest transparency. The connected dots were decoded centroids of each orientation trials from 3 days.
(L) Orientation distance index decoded based on activity of responsive neurons in the visual areas or in the non-visual areas, $^{***}p = 2.16 \times 10^{-32}$. One-way ANOVA test.
Scale bars: 50 μm (zoom-in area in B), 400 μm (B), 2 SD (F), and 2 s (F).
See also Figure S6.

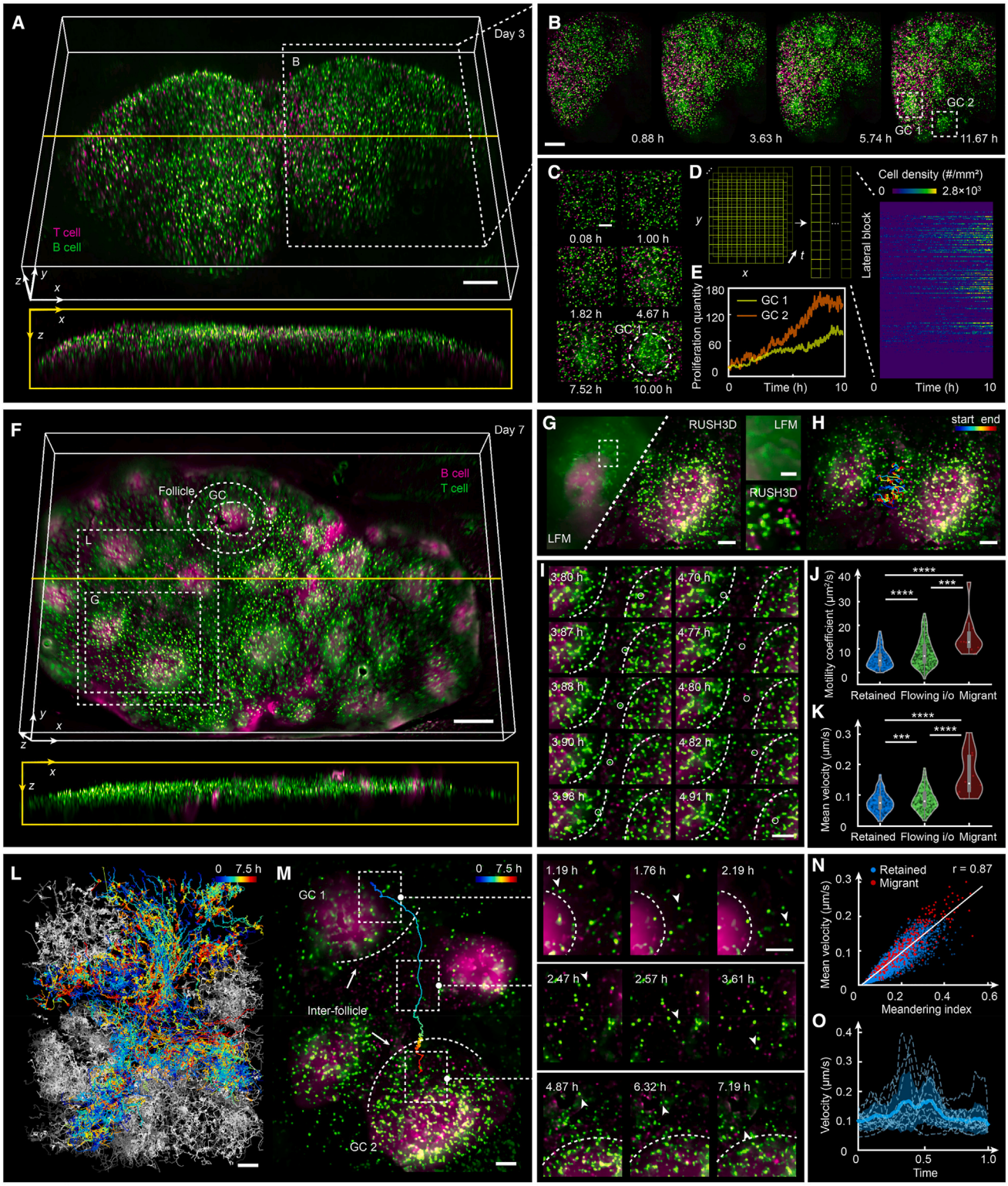

Figure 6. Long-term imaging of large-scale immune cells covering multiple germinal centers in inguinal lymph nodes

(A) 3D rendering of inguinal lymph node across 4 mm × 3 mm × 450 μm in the beginning stage of forming germinal centers (GCs) obtained by RUSH3D. B cells (green) and T cells (magenta) are labeled by dsRed and GFP, respectively.

(B) Zoom-in MIPs of the region marked in (A) at 4 time points to show B cells clustering.

(legend continued on next page)

based on multi-view data obtained by RUSH3D, which is essential for long-term imaging across several hours (Figure S7A; Video S4). Average depth estimation error can be maintained within 2 μm even with strong aberrations (Figures S7B and S7C). In this case, we uninterruptedly observed the clustering of immune cells in MD4/OT-II co-transfer systems across a 4 × 3 × 0.45 mm^3 volume at single-cell resolution over 15 h *in vivo* (Figure 6A). Through continuous 3D imaging with a large depth range of 450 μm to cover the 3D lymph node surface (Video S5), we managed to track individual cells that are sparsely labeled, comprising about 10% of total responding B cells and T cells, thereby characterizing formation processes of multiple GCs simultaneously (Figures 6B and 6C). Our recordings have identified multiple GCs dispersed across the lymph node (Figures S7E–S7G), each of which progressively densifies due to an increasing number of cell proliferation (Figures 6D, 6E, and S7H–S7K).

Previous studies have proposed that follicular helper T (T_{FH}) cells can traverse across GCs in relatively small FOV, as discerned through hours-long interval imaging.[53] Capitalizing on large FOV (Figure 6F), robust imaging quality (Figure 6G), and low phototoxicity of RUSH3D, we tried to corroborate this hypothesis via continuous imaging across an ensemble of tens of GCs over 13 h (145–158 h post-immunization, Video S6). Through analysis, we identified multiple T cells that traversed across GCs, delineating cross-GC trajectories (Figures 6H and 6I). We found a majority of these "messenger" cells exhibit a significant acceleration while navigating between GCs compared with lingering or transitioning into or out of a GC (Figures 6J and 6K, $p < 0.001$, two-sided Wilcoxon rank-sum test).

Through the analysis of large-scale tracked T cells encompassing the breadth of the lymph node (Figure 6L), we also distinguished T cells exhibiting long-distance migration through a specific pathway (Figure 6M). These cells were not ensnared by proximate GCs they encountered en route but instead navigated toward a distant GC. From a statistical standpoint, we discerned substantial correlations between the meandering index and the mean velocity of both lingering and migrating T cells (Figure 6N) and observed an acceleration in migrating T cells during their inter-GC journey (Figure 6O). Looking forward, the extensive, long-term, and reliable 3D imaging capabilities of RUSH3D will facilitate a more exhaustive analysis of GC formation and development through large-scale cellular interactions.

Cortex-wide monitoring of neutrophil dynamics after TBI

TBI usually occurs when a sudden force damages the brain and leads to profound physical, psychological, cognitive, emotional, and social effects.[54] Better understanding the timing and complexity of immune responses following TBI may lead to more effective immunomodulatory therapies.[55] However, cortex-wide responses of immune cells remain poorly grasped and are challenging to be studied for intertwined reasons. Applying cranial windows or thinned skulls for optical interrogation before TBI will break the stability of skull structures during the force damage. Contradictorily, applying them after the TBI alters the native immune response. Moreover, many immune

(C) Further zoom-in MIPs of the marked GC1 region in (B) at 6 time points.
(D) The heatmap of the local cell density versus the time. The whole FOV is divided into 2,000 blocks (50 along *x* axis and 40 along *y* axis, as illustrated in the left).
(E) Characteristics of cell proliferation quantity in two GCs (GC1 and GC2 in B).
(F) 3D rendering of inguinal lymph node across 6.2 × 3.8 × 0.45 mm^3 after formation of multiple GCs. B cells (magenta) and T cells (green) are labeled by GFP and dsRed, respectively.
(G) Comparison of the MIPs obtained by LFM (left) and RUSH3D (right) of the zoom-in region marked in (F). Further zoom-in regions for comparisons are shown on the right.
(H) Trajectories of multiple T cells flow across two adjacent GCs (the same region as G), delineated by colors for time variation.
(I) Examples of T cells flowing across two GCs spanning 1 h. The T cell of interest is outlined by white circles, and two adjacent GCs are outlined by white dashed lines.
(J) Violin plot of motility coefficients for three types (retained, flowing i/o [flowing in or out], and migrant) of T cells. Retained type: T cells maintain their position within a germinal center (GC), devoid of flow in or out. Flowing i/o: T cells are mandated to traverse the GC boundary once, albeit they do not migrate to alternate GCs. Migrant: T cells are necessarily in transit toward other GCs. Motility coefficients (μm^2/min) were calculated for individual tracks by linear regression of displacement versus time point. ***$p < 0.001$, ****$p < 0.0001$, two-sided Wilcoxon rank-sum test. $n = 462$ (retained), 351 (flowing i/o), and 14 (migrant). White circle: median. Thick gray vertical line: interquartile range. Thin vertical lines: upper and lower proximal values. Transparent disks: data points. Transparent violin-shaped areas: kernel density estimate of data distribution.
(K) Violin plot of mean velocity for three categories (retained, flowing i/o and migrant) of T cells. Mean velocity (μm/s) was calculated for individual tracks by linear regression of trajectory lengths versus time points. ***$p < 0.001$, ****$p < 0.0001$, two-sided Wilcoxon rank-sum test. $n = 462$ (retained), 351 (flowing i/o), and 14 (migrant). Symbols are the same as in (H).
(L) Overlay of 3D tracked T cell traces across 7.5 h. Traces across follicles are represented by the colored lines (representing different time points), while other T cell traces are represented by white lines.
(M) Tracking of a T cell flowing across two distinct GCs, whose trajectory is delineated by colors for time variation. Right, time-lapse rendering of the T cell migration in different time points, as marked by white arrows.
(N) Scatterplot of meandering index versus mean velocity of tracked T cells. Two categories of T cells (retained and migrant) are plotted. The meandering index for a cell track was computed as the displacement between the initial and final points on each track divided by the total length of the random path. The thick black line represents the linear regression between the meandering index and mean velocity of tracked T cells, with $r = 0.87$.
(O) Characteristics of T cell velocity during cross-GC migration. T cells whose tracking lengths are longer than 200 frames are selected. For each T cell, its trajectory is normalized into [0, 1] intervals where 0 indicates the commencement of migration, and 1 indicates the culmination of migration. Each dashed line represents a single T cell. Thick line: mean. Shaded area, SD.
Scale bars: 300 μm (A, B, and F), 100 μm (C, G–I, L, and M), and 30 μm (zoom-in area in G).
See also Figure S7 and Videos S4, S5, and S6.

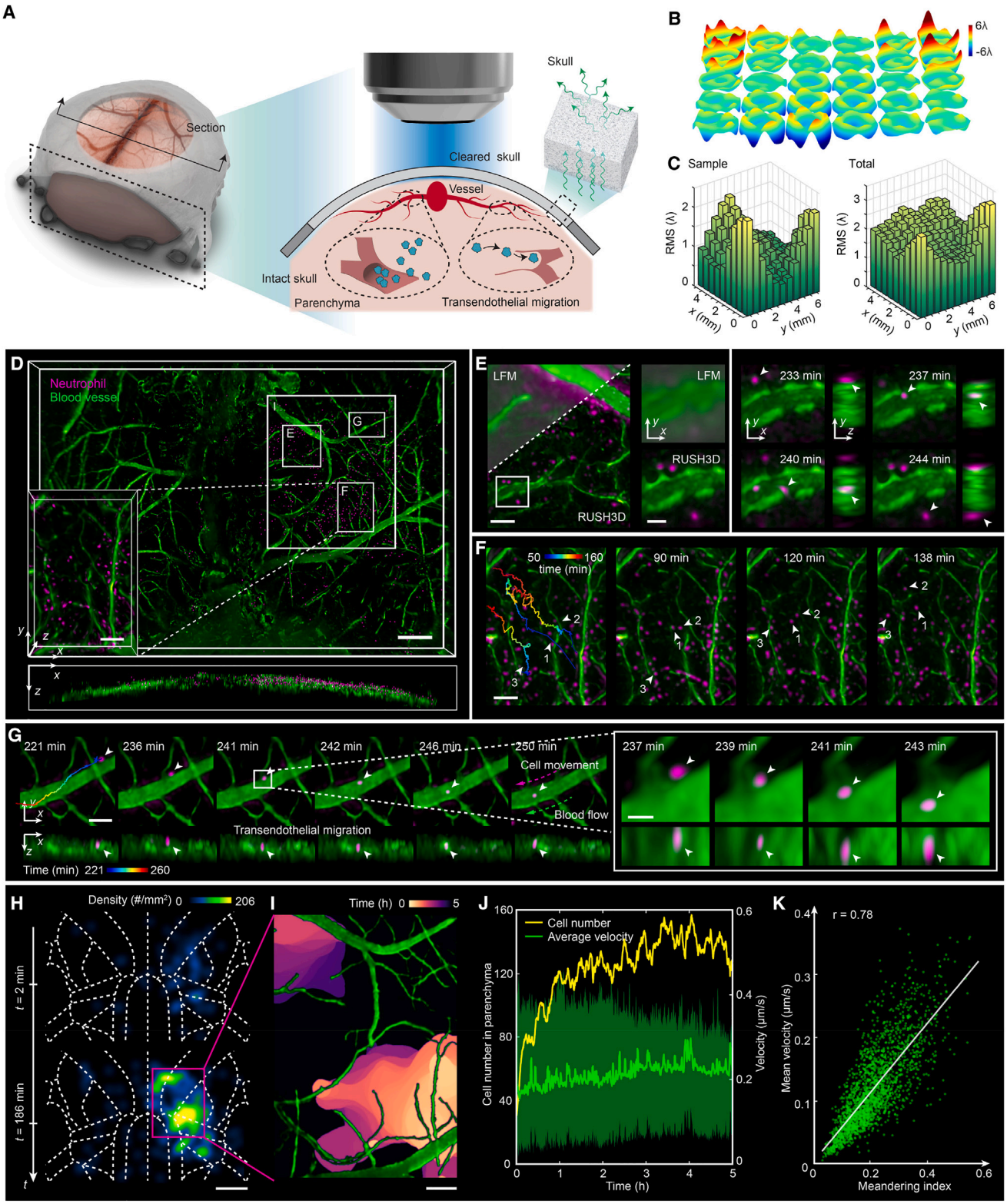

Figure 7. Large-scale immune response of neutrophils during traumatic brain injury

(A) Experimental schematic for the observation of traumatic brain injury (TBI) by RUSH3D in conjunction with the through-intact-skull (TIS) window.

(B) Strong nonuniform aberrations across the cleared TIS window estimated by wDAO.

(legend continued on next page)

responses such as transendothelial migrations are rare events that happen randomly across whole cortex. Cortex-wide monitoring with single-cell resolution is necessary to capture these rare events at single trial.

RUSH3D precisely fills this niche by combining with a through-intact-skull (TIS) window.[56] We established a closed head-injury model in mice that replicates certain pathological features commonly observed in humans with mild TBI.[57–59] Moreover, we optically cleared an 8-mm diameter window in the skull to avoid additional brain injury or inflammation after recovery (Figure 7A). The compact skull still introduces substantial aberrations to optical observations across the whole FOV. We found the induced wavefront errors reached 3 wavelengths in RMS (Figures 7B and 7C), leading to strong degradation in resolution and SBR that prevents wide-field and light-field imaging from resolving single cells (Figures S7L–S7N). By contrast, RUSH3D corrected these aberrations and restored clear structures of both cells and micropillars with wDAO (Figure 7D), especially those that were previously submersed under the strong background and aberrations (Figures 7E and S7N).

With two-color imaging of both vessels and neutrophils, RUSH3D captured the influx of large-scale meningeal neutrophils from the peripheral immune system into the parenchyma, a response to acute brain injury (Figure 7F; Video S7). We observed that most neutrophils did not come from the vessels but originated from other structures around the vessels. Owing to the large FOV, RUSH3D captured rare events such as reverse transendothelial migration of neutrophils, a phenomenon previously documented in other body regions[60] (Figure 7G). Following that, we meticulously tracked individual cells using RUSH3D to analyze diffusion trajectories of neutrophils, detailing their concentrations throughout the observation period post-TBI (Figures 7H and 7I). We noted a consistent amplification in the quantity of neutrophils within the parenchyma, an escalation outpacing the increased velocity of neutrophil movement (Figure 7J). Furthermore, we discerned a substantial correlation between the meandering index of neutrophils and their average velocity, suggesting that swifter neutrophils adhere to a more directed trajectory compared with their slower counterparts (Figure 7K). These large-scale observations of the TBI-modulated brain environment in its pristine state may augment our understanding of the regulatory mechanisms governing the neuroimmune surveillance system.

DISCUSSION

In conclusion, RUSH3D emerges as a compact solution for the study of large-scale intercellular interactions across a mammalian organ during native physio-pathological states, delivering mesoscopic rapid high-resolution 3D imaging in turbid tissues with low phototoxicity and high throughput.

Spatially variant optical aberrations, originating from both optical engineering and tissue heterogeneity, pose a fundamental challenge on mesoscopic intravital imaging. Rather than capturing images, RUSH3D captures the whole imaging process with ultra-fine measurement of light fields and adopts flexible manipulation of the light rays in post processing for multi-site aberration correction and 3D reconstruction, enabling a generally accessible system for mesoscale 3D imaging with high resolution. Thereby, RUSH3D overcomes traditional trade-off between system size and imaging throughput in previous mesoscopes. Furthermore, since the imaging framework is highly scalable, multiple cameras can be added in a straightforward way to further increase effective pixel numbers without using complicated systems. High-frame-rate cameras can also extend RUSH3D's potential, capturing high-temporal dynamics such as genetically encoded voltage indicators[61,62] across large volumes.

With the multiscale imaging capability in both spatial and temporal domains, RUSH3D provides a panoramic view for tissue heterogeneity, which is critical for unbiased investigation of diverse cellular behaviors. For example, intravital drug screen can be conducted with a huge improvement of efficiency at single-trial level. Cross-animal variance can be alleviated with enough data for statistical analysis in a single experiment. Various rare events such as tumor metastasis that happened randomly in the spatiotemporal domain will become common events during RUSH3D observation. Long-distance intercellular communications can be visualized simultaneously. Long-term tracking of millions of cells may reveal the basic physics of emergent functions of collective cellular behaviors *in vivo*. In addition, the integration of RUSH3D with advanced spatial

(C) Root mean square (RMS) wavefront errors across the FOV induced by the cleared TIS window (left) and total wavefront errors (induced by cleared TIS window and system aberration, right).
(D) 3D rendering of vessels (green) and neutrophils (magenta) in mouse cortex across 6.5 × 5 × 0.45 mm^3 after TBI.
(E) Comparison of the MIPs of the zoom-in region marked in (D) obtained by LFM (top left) and RUSH3D (bottom right), with further zoom-in MIP of the marked box. Examples of neutrophils (designated by white arrows) entering and departing from vessels at different time points are shown on the right with orthogonal MIPs.
(F) Tracking of neutrophils flowing across vessel network marked in (D). Three neutrophils tracked in this area are highlighted by white arrows. Color-coded neutrophil traces are overlaid in the left panel.
(G) Tracking of a neutrophil marked by the arrows flowing from parenchymal tissues to vessels marked in (D).
(H) The density map of neutrophils across the whole FOV at two example time points.
(I) Diffusion chronicle of neutrophils over 5 h. Areas manifesting a neutrophil density over 60 cells/mm^2 are designated as "diffused." Hues signify disparate moments when the neutrophil density was achieved. Segmented vessels are delineated in green.
(J) Characteristics of neutrophil number (yellow) in the parenchymal tissues as well as neutrophil moving velocity (green) during 5-h observation. Thick line: mean. Shaded area: SD.
(K) Scatterplot of meandering index versus mean velocity of tracked neutrophils. Thick line represents linear regression (r = 0.78).
Scale bars: 500 μm (D), 100 μm (E–G, and zoom-in area in D), 30 μm (zoom-in area in E), 20 μm (zoom-in area in G), 1,000 μm (H), and 200 μm (I).
See also Figure S7 and Video S7.

transcriptomics technology[63,64] may offer broad insights to correlate large-scale cellular dynamics with the organization and connectivity of diverse cell types, circuit dynamics, behaviors, and diseases. We believe the general accessibility of RUSH3D could lead to broad discoveries in complex biological processes like neural computation,[65,66] immune responses,[67] and neuroinflammation.[59,68]

Limitations of the study

RUSH3D encounters challenges across multiple dimensions. Firstly, we now utilize a camera with a large active area but only a 12-bit depth, restricting its application in samples of extremely varied brightness. With advancements in fabrication techniques, cameras with higher dynamic ranges (e.g., 16-bit) or faster speeds can be used in the future. Secondly, resolution of RUSH3D slightly decays with increase of the distance from native objective plane. Incorporating wavefront coding can mitigate this problem with further increased depth of field.[69] Thirdly, as neuron density escalates, the effectiveness of algorithmic demixing (e.g., SSID) may decay due to sensor quantization limits. Slit confocal configuration[70,71] can be integrated to further increase the fidelity of RUSH3D. Fourthly, our current motion correction algorithm operates under the assumption that most biological samples change at speeds lower than the high imaging frame rate. However, sudden movements, such as those induced by respiration, can still result in residual motion artifacts, as observed in burst motions in Video S7. Fifthly, since RUSH3D is still a one-photon imaging method, the operational imaging volume *in vivo* is also constrained by tissue scattering and targeted feature size. Multi-photon excitation with both spatial and angular sampling such as two-photon synthetic aperture microscopy may increase the penetration depth with other capabilities remained. Finally, current 3D reconstruction demands iterative processing for aberration-corrected large volumes, which can be time-consuming for thousands of frames. Future application of learning-based algorithms could lessen computational demands with better computing devices.[72,73] Moreover, the development of more sophisticated and efficient downstream analysis algorithms becomes crucial for the huge mesoscale data.

RESOURCE AVAILABILITY

Lead contact

Further information and requests for resources and reagents should be directed to and will be fulfilled by the lead contact, Qionghai Dai (daiqh@tsinghua.edu.cn).

Materials availability

This study did not generate new unique reagents.

Data and code availability

The codes generated during this study with example data are available at GitHub with the following link: https://github.com/yuanlong-o/RUSH3D. RUSH3D-2P validation data are available with the following link: https://doi.org/10.5281/zenodo.12789868. The published article includes all data generated during this study and all the raw data is also available from the corresponding author upon request. Any additional information required to reanalyze the data reported in this paper is available from the lead contact upon request.

ACKNOWLEDGMENTS

We would like to acknowledge Z. Jiang for providing the zebrafish larvae used in this research. We would like to acknowledge K. Li and G. Qi for providing the Oxtr-Ai148d mice used in this research. We would like to acknowledge D. Zhu for providing the through-intact-skull (TIS) reagent and techniques. We would like to acknowledge M. Li and M. Tong for their supporting analysis. We further thank the support from the Beijing Laboratory of Brain and Cognitive Intelligence, the Beijing Municipal Education Commission, and the Tsinghua-Peking Joint Center for Life Sciences. Y.Z., M.W., Q.Z., Y.G., B.L., J.L., X.Y., C.K., J.W., Z.V.G., and Q.D. were supported by the National Natural Science Foundation of China (62088102, 62222508, 62071272, 61831014, 62125106, and 32170998), the STI2030-Major Projects (2021ZD0203600), and the "Bio-Brain + X" Advanced Imaging Instrument Development Seed Grant.

AUTHOR CONTRIBUTIONS

Conceptualization: J.W. and Q.D.; methodology: J.W., Yuanlong Zhang, M.W., and Y.G.; biological experiments: Z.V.G., M.W., Q.Z., B.L., J.L., Yi Zhang, Y.H., and H.Q.; investigation: Yuanlong Zhang, M.W., J.W., Q.Z., X.Y., C.K., and Z.V.G.; visualization: Yuanlong Zhang, M.W., and Q.Z.; funding acquisition: Q.D., J.W., and Z.V.G.; project administration: Q.D., J.W., and Z.V.G.; supervision: Q.D., J.W., and Z.V.G.; writing – original draft: Yuanlong Zhang, M.W., J.W., Q.Z., Z.V.G., and Q.D.; writing – review & editing: Yuanlong Zhang, M.W., Q.Z., J.W., Z.V.G., and Q.D.

DECLARATION OF INTERESTS

The authors declare the following competing interests: Q.D. and J.W. are founders and equity holders of Zhejiang Hehu Technology LLC. Q.D., J.W., M.W., and Yuanlong Zhang submitted patent applications related to the RUSH3D technology described in this work.

STAR★METHODS

Detailed methods are provided in the online version of this paper and include the following:

- KEY RESOURCES TABLE
- EXPERIMENTAL MODEL AND STUDY PARTICIPANT DETAILS
  - Animals
  - Neural imaging in mouse
  - Mouse lymph node imaging
  - Mouse TBI model and imaging
  - Zebrafish imaging
  - Mouse brain slice clearing, immunohistochemical staining, and imaging
- METHOD DETAILS
  - Experimental setup
  - Pixel realignment
  - Wave-optics digital adaptive optics (wDAO)
  - Multiscale background rejection (MBR)
  - Motion corrections
  - Sparse seeded iteration demixing (SSID) pipeline
  - Simultaneous RUSH3D and two-photon joint validation
  - RUSH3D operation protocols
  - Apparatus for stimulus delivery and behavioral tracking in mouse neural imaging
  - Data management and hardware of RUSH3D computational pipeline
- QUANTIFICATION AND STATISTICAL ANALYSIS
  - Statistical analysis

SUPPLEMENTAL INFORMATION

Supplemental information can be found online at https://doi.org/10.1016/j.cell.2024.08.026.

Received: January 5, 2024
Revised: June 6, 2024
Accepted: August 13, 2024
Published: September 13, 2024

REFERENCES

1. Germain, R.N., Robey, E.A., and Cahalan, M.D. (2012). A decade of imaging cellular motility and interaction dynamics in the immune system. Science *336*, 1676–1681. https://doi.org/10.1126/science.122106.
2. Victora, G.D., Schwickert, T.A., Fooksman, D.R., Kamphorst, A.O., Meyer-Hermann, M., Dustin, M.L., and Nussenzweig, M.C. (2010). Germinal Center Dynamics Revealed by Multiphoton Microscopy with a Photoactivatable Fluorescent Reporter. Cell *143*, 592–605. https://doi.org/10.1016/j.cell.2010.10.032.
3. Gonzalez-Figueroa, P., Roco, J.A., Papa, I., Núñez, V.L., Stanley, M., Linterman, M.A., Dent, A., Canete, P.F., and Vinuesa, C.G. (2021). Follicular regulatory T cells produce neuritin to regulate B cells. Cell *184*, 1775–1789.e19. https://doi.org/10.1016/j.cell.2021.02.027.
4. Ebrahimi, S., Lecoq, J., Rumyantsev, O., Tasci, T., Zhang, Y., Irimia, C., Li, J., Ganguli, S., and Schnitzer, M.J. (2022). Emergent reliability in sensory cortical coding and inter-area communication. Nature *605*, 713–721. https://doi.org/10.1038/s41586-022-04724-y.
5. Driscoll, L.N., Pettit, N.L., Minderer, M., Chettih, S.N., and Harvey, C.D. (2017). Dynamic Reorganization of Neuronal Activity Patterns in Parietal Cortex. Cell *170*, 986–999.e16. https://doi.org/10.1016/j.cell.2017.07.021.
6. Li, K., Nakajima, M., Ibañez-Tallon, I., and Heintz, N. (2016). A Cortical Circuit for Sexually Dimorphic Oxytocin-Dependent Anxiety Behaviors. Cell *167*, 60–72.e11. https://doi.org/10.1016/j.cell.2016.08.067.
7. Keller, P.J., Schmidt, A.D., Wittbrodt, J., and Stelzer, E.H.K. (2008). Reconstruction of zebrafish early embryonic development by scanned light sheet microscopy. Science *322*, 1065–1069. https://doi.org/10.1126/science.1162493.
8. Chen, B.C., Legant, W.R., Wang, K., Shao, L., Milkie, D.E., Davidson, M.W., Janetopoulos, C., Wu, X.S., Hammer, J.A., 3rd, Liu, Z., et al. (2014). Lattice light-sheet microscopy: imaging molecules to embryos at high spatiotemporal resolution. Science *346*, 1257998. https://doi.org/10.1126/science.1257998.
9. Li, D., Shao, L., Chen, B.C., Zhang, X., Zhang, M., Moses, B., Milkie, D.E., Beach, J.R., Hammer, J.A., 3rd, Pasham, M., et al. (2015). ADVANCED IMAGING. Extended-resolution structured illumination imaging of endocytic and cytoskeletal dynamics. Science *349*, aab3500. https://doi.org/10.1126/science.aab3500.
10. Werley, C.A., Chien, M.P., and Cohen, A.E. (2017). Ultrawidefield microscope for high-speed fluorescence imaging and targeted optogenetic stimulation. Biomed. Opt. Express *8*, 5794–5813. https://doi.org/10.1364/BOE.8.005794.
11. Zheng, G., Horstmeyer, R., and Yang, C. (2013). Wide-field, high-resolution Fourier ptychographic microscopy. Nat. Photonics *7*, 739–745. https://doi.org/10.1038/nphoton.2013.187.
12. Fan, J., Suo, J., Wu, J., Xie, H., Shen, Y., Chen, F., Wang, G., Cao, L., Jin, G., He, Q., et al. (2019). Video-rate imaging of biological dynamics at centimetre scale and micrometre resolution. Nat. Photonics *13*, 809–816. https://doi.org/10.1038/s41566-019-0474-7.
13. Nöbauer, T., Zhang, Y., Kim, H., and Vaziri, A. (2023). Mesoscale volumetric light-field (MesoLF) imaging of neuroactivity across cortical areas at 18 Hz. Nat. Methods *20*, 600–609. https://doi.org/10.1038/s41592-023-01789-z.
14. Sofroniew, N.J., Flickinger, D., King, J., and Svoboda, K. (2016). A large field of view two-photon mesoscope with subcellular resolution for in vivo imaging. eLife *5*, e14472. https://doi.org/10.7554/eLife.14472.
15. Kim, T.H., and Schnitzer, M.J. (2022). Fluorescence imaging of large-scale neural ensemble dynamics. Cell *185*, 9–41. https://doi.org/10.1016/j.cell.2021.12.007.
16. Ji, N., Milkie, D.E., and Betzig, E. (2010). Adaptive optics via pupil segmentation for high-resolution imaging in biological tissues. Nat. Methods *7*, 141–147. https://doi.org/10.1038/nmeth.1411.
17. Park, J.H., Kong, L., Zhou, Y., and Cui, M. (2017). Large-field-of-view imaging by multi-pupil adaptive optics. Nat. Methods *14*, 581–583. https://doi.org/10.1038/nmeth.4290.
18. Ji, N. (2017). Adaptive optical fluorescence microscopy. Nat. Methods *14*, 374–380. https://doi.org/10.1038/nmeth.4218.
19. Denk, W., Strickler, J.H., and Webb, W.W. (1990). Two-photon laser scanning fluorescence microscopy. Science *248*, 73–76. https://doi.org/10.1126/science.2321027.
20. Bouchard, M.B., Voleti, V., Mendes, C.S., Lacefield, C., Grueber, W.B., Mann, R.S., Bruno, R.M., and Hillman, E.M.C. (2015). Swept confocally-aligned planar excitation (SCAPE) microscopy for high speed volumetric imaging of behaving organisms. Nat. Photonics *9*, 113–119. https://doi.org/10.1038/nphoton.2014.323.
21. Wu, J., Lu, Z., Jiang, D., Guo, Y., Qiao, H., Zhang, Y., Zhu, T., Cai, Y., Zhang, X., Zhanghao, K., et al. (2021). Iterative tomography with digital adaptive optics permits hour-long intravital observation of 3D subcellular dynamics at millisecond scale. Cell *184*, 3318–3332.e17. https://doi.org/10.1016/j.cell.2021.04.029.
22. Wu, J., Guo, Y., Deng, C., Zhang, A., Qiao, H., Lu, Z., Xie, J., Fang, L., and Dai, Q. (2022). An integrated imaging sensor for aberration-corrected 3D photography. Nature *612*, 62–71. https://doi.org/10.1038/s41586-022-05306-8.
23. Zhang, Y., Lu, Z., Wu, J., Lin, X., Jiang, D., Cai, Y., Xie, J., Wang, Y., Zhu, T., Ji, X., et al. (2021). Computational optical sectioning with an incoherent multiscale scattering model for light-field microscopy. Nat. Commun. *12*, 6391. https://doi.org/10.1038/s41467-021-26730-w.
24. Rumyantsev, O.I., Lecoq, J.A., Hernandez, O., Zhang, Y., Savall, J., Chrapkiewicz, R., Li, J., Zeng, H., Ganguli, S., and Schnitzer, M.J. (2020). Fundamental bounds on the fidelity of sensory cortical coding. Nature *580*, 100–105. https://doi.org/10.1038/s41586-020-2130-2.
25. Lu, R., Liang, Y., Meng, G., Zhou, P., Svoboda, K., Paninski, L., and Ji, N. (2020). Rapid mesoscale volumetric imaging of neural activity with synaptic resolution. Nat. Methods *17*, 291–294. https://doi.org/10.1038/s41592-020-0760-9.
26. Orth, A., and Crozier, K. (2012). Microscopy with microlens arrays: high throughput, high resolution and light-field imaging. Opt. Express *20*, 13522–13531. https://doi.org/10.1364/OE.20.013522.
27. Demas, J., Manley, J., Tejera, F., Barber, K., Kim, H., Traub, F.M., Chen, B., and Vaziri, A. (2021). High-speed, cortex-wide volumetric recording of neuroactivity at cellular resolution using light beads microscopy. Nat. Methods *18*, 1103–1111. https://doi.org/10.1038/s41592-021-01239-8.
28. McConnell, G., Trägårdh, J., Amor, R., Dempster, J., Reid, E., and Amos, W.B. (2016). A novel optical microscope for imaging large embryos and tissue volumes with sub-cellular resolution throughout. eLife *5*, e18659. https://doi.org/10.7554/eLife.18659.
29. Xue, Y., Davison, I.G., Boas, D.A., and Tian, L. (2020). Single-shot 3D wide-field fluorescence imaging with a Computational Miniature Mesoscope. Sci. Adv. *6*, eabb7508. https://doi.org/10.1126/sciadv.abb7508.
30. Tsai, P.S., Mateo, C., Field, J.J., Schaffer, C.B., Anderson, M.E., and Kleinfeld, D. (2015). Ultra-large field-of-view two-photon microscopy. Opt. Express *23*, 13833–13847. https://doi.org/10.1364/OE.23.013833.
31. Zheng, G., Ou, X., Horstmeyer, R., and Yang, C. (2013). Characterization of spatially varying aberrations for wide field-of-view microscopy. Opt. Express *21*, 15131–15143. https://doi.org/10.1364/OE.21.015131.
32. Yu, C.H., Stirman, J.N., Yu, Y., Hira, R., and Smith, S.L. (2021). Diesel2p mesoscope with dual independent scan engines for flexible capture of dynamics in distributed neural circuitry. Nat. Commun. *12*, 6639. https://doi.org/10.1038/s41467-021-26736-4.
33. Zhao, Z., Zhou, Y., Liu, B., He, J., Zhao, J., Cai, Y., Fan, J., Li, X., Wang, Z., Lu, Z., et al. (2023). Two-photon synthetic aperture microscopy for

minimally invasive fast 3D imaging of native subcellular behaviors in deep tissue. Cell *186*, 2475–2491.e22. https://doi.org/10.1016/j.cell.2023.04.016.

34. Mertz, J., and Kim, J. (2010). Scanning light-sheet microscopy in the whole mouse brain with HiLo background rejection. J. Biomed. Opt. *15*, 016027. https://doi.org/10.1117/1.3324890.

35. Murakami, T.C., Mano, T., Saikawa, S., Horiguchi, S.A., Shigeta, D., Baba, K., Sekiya, H., Shimizu, Y., Tanaka, K.F., Kiyonari, H., et al. (2018). A three-dimensional single-cell-resolution whole-brain atlas using CUBIC-X expansion microscopy and tissue clearing. Nat. Neurosci. *21*, 625–637. https://doi.org/10.1038/s41593-018-0109-1.

36. Lai, H.M., Liu, A.K.L., Ng, H.H.M., Goldfinger, M.H., Chau, T.W., DeFelice, J., Tilley, B.S., Wong, W.M., Wu, W., and Gentleman, S.M. (2018). Next generation histology methods for three-dimensional imaging of fresh and archival human brain tissues. Nat. Commun. *9*, 1066. https://doi.org/10.1038/s41467-018-03359-w.

37. Zhang, F., Berg, M., Dierking, K., Félix, M.A., Shapira, M., Samuel, B.S., and Schulenburg, H. (2017). Caenorhabditis elegans as a Model for Microbiome Research. Front. Microbiol. *8*, 485. https://doi.org/10.3389/fmicb.2017.00485.

38. MacRae, C.A., and Peterson, R.T. (2015). Zebrafish as tools for drug discovery. Nat. Rev. Drug Discov. *14*, 721–731. https://doi.org/10.1038/nrd4627.

39. Stringer, C., Pachitariu, M., Steinmetz, N., Carandini, M., and Harris, K.D. (2019). High-dimensional geometry of population responses in visual cortex. Nature *571*, 361–365. https://doi.org/10.1038/s41586-019-1346-5.

40. Stringer, C., Pachitariu, M., Steinmetz, N., Reddy, C.B., Carandini, M., and Harris, K.D. (2019). Spontaneous behaviors drive multidimensional, brain-wide activity. Science *364*, 255. https://doi.org/10.1126/science.aav7893.

41. Mao, T., Kusefoglu, D., Hooks, B.M., Huber, D., Petreanu, L., and Svoboda, K. (2011). Long-range neuronal circuits underlying the interaction between sensory and motor cortex. Neuron *72*, 111–123. https://doi.org/10.1016/j.neuron.2011.07.029.

42. Abbott, L.F., and Dayan, P. (1999). The effect of correlated variability on the accuracy of a population code. Neural Comput. *11*, 91–101. https://doi.org/10.1162/089976699300016827.

43. Makino, H., Ren, C., Liu, H., Kim, A.N., Kondapaneni, N., Liu, X., Kuzum, D., and Komiyama, T. (2017). Transformation of Cortex-wide Emergent Properties during Motor Learning. Neuron *94*, 880–890.e8. https://doi.org/10.1016/j.neuron.2017.04.015.

44. Pinto, L., Rajan, K., DePasquale, B., Thiberge, S.Y., Tank, D.W., and Brody, C.D. (2019). Task-Dependent Changes in the Large-Scale Dynamics and Necessity of Cortical Regions. Neuron *104*, 810–824.e9. https://doi.org/10.1016/j.neuron.2019.08.025.

45. Nöbauer, T., Skocek, O., Pernía-Andrade, A.J., Weilguny, L., Traub, F.M., Molodtsov, M.I., and Vaziri, A. (2017). Video rate volumetric Ca^{2+} imaging across cortex using seeded iterative demixing (SID) microscopy. Nat. Methods *14*, 811–818. https://doi.org/10.1038/nmeth.4341.

46. Song, A., Gauthier, J.L., Pillow, J.W., Tank, D.W., and Charles, A.S. (2021). Neural Anatomy and Optical Microscopy (NAOMi) Simulation for evaluating calcium imaging methods. J. Neurosci. Methods *358*, 109173. https://doi.org/10.1016/j.jneumeth.2021.109173.

47. Chen, T.W., Wardill, T.J., Sun, Y., Pulver, S.R., Renninger, S.L., Baohan, A., Schreiter, E.R., Kerr, R.A., Orger, M.B., Jayaraman, V., et al. (2013). Ultrasensitive fluorescent proteins for imaging neuronal activity. Nature *499*, 295–300. https://doi.org/10.1038/nature12354.

48. Barnett, L., and Seth, A.K. (2014). The MVGC multivariate Granger causality toolbox: a new approach to Granger-causal inference. J. Neurosci. Methods *223*, 50–68. https://doi.org/10.1016/j.jneumeth.2013.10.018.

49. Mackevicius, E.L., Bahle, A.H., Williams, A.H., Gu, S., Denisenko, N.I., Goldman, M.S., and Fee, M.S. (2019). Unsupervised discovery of temporal sequences in high-dimensional datasets, with applications to neuroscience. eLife *8*, e38471. https://doi.org/10.7554/eLife.38471.

50. Kobak, D., Brendel, W., Constantinidis, C., Feierstein, C.E., Kepecs, A., Mainen, Z.F., Qi, X.L., Romo, R., Uchida, N., and Machens, C.K. (2016). Demixed principal component analysis of neural population data. eLife *5*, e10989. https://doi.org/10.7554/eLife.10989.

51. Liu, D., Xu, H., Shih, C., Wan, Z., Ma, X., Ma, W., Luo, D., and Qi, H. (2015). T-B-cell entanglement and ICOSL-driven feed-forward regulation of germinal centre reaction. Nature *517*, 214–218. https://doi.org/10.1038/nature13803.

52. Liu, B., Lin, Y., Yan, J., Yao, J., Liu, D., Ma, W., Wang, J., Liu, W., Wang, C., Zhang, L., et al. (2021). Affinity-coupled CCL22 promotes positive selection in germinal centres. Nature *592*, 133–137. https://doi.org/10.1038/s41586-021-03239-2.

53. Shulman, Z., Gitlin, A.D., Targ, S., Jankovic, M., Pasqual, G., Nussenzweig, M.C., and Victora, G.D. (2013). T follicular helper cell dynamics in germinal centers. Science *341*, 673–677. https://doi.org/10.1126/science.1241680.

54. Loane, D.J., and Kumar, A. (2016). Microglia in the TBI brain: The good, the bad, and the dysregulated. Exp. Neurol. *275*, 316–327. https://doi.org/10.1016/j.expneurol.2015.08.018.

55. Jassam, Y.N., Izzy, S., Whalen, M., McGavern, D.B., and El Khoury, J. (2017). Neuroimmunology of Traumatic Brain Injury: Time for a Paradigm Shift. Neuron *95*, 1246–1265. https://doi.org/10.1016/j.neuron.2017.07.010.

56. Li, D., Hu, Z., Zhang, H., Yang, Q., Zhu, L., Liu, Y., Yu, T., Zhu, J., Wu, J., He, J., et al. (2022). A Through-Intact-Skull (TIS) chronic window technique for cortical structure and function observation in mice. eLight *2*, 15. https://doi.org/10.1186/s43593-022-00022-2.

57. Flierl, M.A., Stahel, P.F., Beauchamp, K.M., Morgan, S.J., Smith, W.R., and Shohami, E. (2009). Mouse closed head injury model induced by a weight-drop device. Nat. Protoc. *4*, 1328–1337. https://doi.org/10.1038/nprot.2009.148.

58. Grutzendler, J., Kasthuri, N., and Gan, W.B. (2002). Long-term dendritic spine stability in the adult cortex. Nature *420*, 812–816. https://doi.org/10.1038/nature01276.

59. Rustenhoven, J., Drieu, A., Mamuladze, T., de Lima, K.A., Dykstra, T., Wall, M., Papadopoulos, Z., Kanamori, M., Salvador, A.F., Baker, W., et al. (2021). Functional characterization of the dural sinuses as a neuroimmune interface. Cell *184*, 1000–1016.e27. https://doi.org/10.1016/j.cell.2020.12.040.

60. Kim, Y.R., Kim, Y.M., Lee, J., Park, J., Lee, J.E., and Hyun, Y.M. (2020). Neutrophils Return to Bloodstream Through the Brain Blood Vessel After Crosstalk With Microglia During LPS-Induced Neuroinflammation. Front. Cell Dev. Biol. *8*, 613733. https://doi.org/10.3389/fcell.2020.613733.

61. Abdelfattah, A.S., Kawashima, T., Singh, A., Novak, O., Liu, H., Shuai, Y., Huang, Y.C., Campagnola, L., Seeman, S.C., Yu, J., et al. (2019). Bright and photostable chemigenetic indicators for extended in vivo voltage imaging. Science *365*, 699–704. https://doi.org/10.1126/science.aav6416.

62. Villette, V., Chavarha, M., Dimov, I.K., Bradley, J., Pradhan, L., Mathieu, B., Evans, S.W., Chamberland, S., Shi, D., Yang, R., et al. (2019). Ultrafast Two-Photon Imaging of a High-Gain Voltage Indicator in Awake Behaving Mice. Cell *179*, 1590–1608.e23. https://doi.org/10.1016/j.cell.2019.11.004.

63. Bao, F., Deng, Y., Wan, S., Shen, S.Q., Wang, B., Dai, Q., Altschuler, S.J., and Wu, L.F. (2022). Integrative spatial analysis of cell morphologies and transcriptional states with MUSE. Nat. Biotechnol. *40*, 1200–1209. https://doi.org/10.1038/s41587-022-01251-z.

64. Crainiciuc, G., Palomino-Segura, M., Molina-Moreno, M., Sicilia, J., Aragones, D.G., Li, J.L.Y., Madurga, R., Adrover, J.M., Aroca-Crevillén, A., Martin-Salamanca, S., et al. (2022). Behavioural immune landscapes of inflammation. Nature *601*, 415–421. https://doi.org/10.1038/s41586-021-04263-y.

65. Li, T., Fu, T.M., Wong, K.K.L., Li, H., Xie, Q., Luginbuhl, D.J., Wagner, M.J., Betzig, E., and Luo, L. (2021). Cellular bases of olfactory circuit assembly

revealed by systematic time-lapse imaging. Cell *184*, 5107–5121.e14. https://doi.org/10.1016/j.cell.2021.08.030.

66. Kasai, H., Ziv, N.E., Okazaki, H., Yagishita, S., and Toyoizumi, T. (2021). Spine dynamics in the brain, mental disorders and artificial neural networks. Nat. Rev. Neurosci. *22*, 407–422. https://doi.org/10.1038/s41583-021-00467-3.
67. Pittet, M.J., Garris, C.S., Arlauckas, S.P., and Weissleder, R. (2018). Recording the wild lives of immune cells. Sci. Immunol. *3*, eaaq0491. https://doi.org/10.1126/sciimmunol.aaq0491.
68. Masuda, T., Amann, L., Monaco, G., Sankowski, R., Staszewski, O., Krueger, M., Del Gaudio, F., He, L., Paterson, N., Nent, E., et al. (2022). Specification of CNS macrophage subsets occurs postnatally in defined niches. Nature *604*, 740–748. https://doi.org/10.1038/s41586-022-04596-2.
69. Cohen, N., Yang, S., Andalman, A., Broxton, M., Grosenick, L., Deisseroth, K., Horowitz, M., and Levoy, M. (2014). Enhancing the performance of the light field microscope using wavefront coding. Opt. Express *22*, 24817–24839. https://doi.org/10.1364/OE.22.024817.
70. Lu, Z., Zuo, S., Shi, M., Fan, J., Xie, J., Xiao, G., Yu, L., Wu, J., and Dai, Q. (2024). Long-term intravital subcellular imaging with confocal scanning light-field microscopy. Published online May 27, 2024. Nat. Biotechnol. https://doi.org/10.1038/s41587-024-02249-5.
71. Zhang, Z., Bai, L., Cong, L., Yu, P., Zhang, T., Shi, W., Li, F., Du, J., and Wang, K. (2021). Imaging volumetric dynamics at high speed in mouse and zebrafish brain with confocal light field microscopy. Nat. Biotechnol. *39*, 74–83. https://doi.org/10.1038/s41587-020-0628-7.
72. Wagner, N., Beuttenmueller, F., Norlin, N., Gierten, J., Boffi, J.C., Wittbrodt, J., Weigert, M., Hufnagel, L., Prevedel, R., and Kreshuk, A. (2021). Deep learning-enhanced light-field imaging with continuous validation. Nat. Methods *18*, 557–563. https://doi.org/10.1038/s41592-021-01136-0.
73. Wang, Z., Zhu, L., Zhang, H., Li, G., Yi, C., Li, Y., Yang, Y., Ding, Y., Zhen, M., Gao, S., et al. (2021). Real-time volumetric reconstruction of biological dynamics with light-field microscopy and deep learning. Nat. Methods *18*, 551–556. https://doi.org/10.1038/s41592-021-01058-x.
74. McInnes, L., Healy, J., and Melville, J. (2018). UMAP: Uniform Manifold Approximation and Projection for Dimension Reduction. Preprint at arXiv. https://doi.org/10.48550/arXiv.1802.03426.
75. Brainard, D.H. (1997). The Psychophysics Toolbox. Spat. Vis. *10*, 433–436. https://doi.org/10.1163/156856897x00357.
76. Qi, H., Cannons, J.L., Klauschen, F., Schwartzberg, P.L., and Germain, R.N. (2008). SAP-controlled T-B cell interactions underlie germinal centre formation. Nature *455*, 764–769. https://doi.org/10.1038/nature07345.
77. Victora, G.D., and Nussenzweig, M.C. (2022). Germinal Centers. Annu. Rev. Immunol. *40*, 413–442. https://doi.org/10.1146/annurev-immunol-120419-022408.
78. Liu, B., and Qi, H. (2022). In vivo migration and Tfh cell interactions. Methods Mol. Biol. *2380*, 99–109. https://doi.org/10.1007/978-1-0716-1736-6_9.
79. Kauvar, I.V., Machado, T.A., Yuen, E., Kochalka, J., Choi, M., Allen, W.E., Wetzstein, G., and Deisseroth, K. (2020). Cortical Observation by Synchronous Multifocal Optical Sampling Reveals Widespread Population Encoding of Actions. Neuron *107*, 351–367.e19. https://doi.org/10.1016/j.neuron.2020.04.023.
80. Broxton, M., Grosenick, L., Yang, S., Cohen, N., Andalman, A., Deisseroth, K., and Levoy, M. (2013). Wave optics theory and 3-D deconvolution for the light field microscope. Opt. Express *21*, 25418–25439. https://doi.org/10.1364/OE.21.025418.
81. Pnevmatikakis, E.A., and Giovannucci, A. (2017). NoRMCorre: An online algorithm for piecewise rigid motion correction of calcium imaging data. J. Neurosci. Methods *291*, 83–94. https://doi.org/10.1016/j.jneumeth.2017.07.031.
82. Cichocki, A., Zdunek, R., and Amari, S. (2007). Hierarchical ALS algorithms for Nonnegative Matrix and 3D Tensor Factorization. In International Conference on Independent Component Analysis and Signal Separation.
83. Syeda, A., Zhong, L., Tung, R., Long, W., Pachitariu, M., and Stringer, C. (2024). Facemap: a framework for modeling neural activity based on orofacial tracking. Nat. Neurosci. *27*, 187–195. https://doi.org/10.1038/s41593-023-01490-6.

STAR★METHODS

KEY RESOURCES TABLE

REAGENT or RESOURCE	SOURCE	IDENTIFIER
Antibodies		
Alexa Fluor 488 anti-mouse Ly6G	Biolegend	Cat# 127626; RRID: AB_2561340
Chemicals, peptides, and recombinant proteins		
Carboxylate-Modified Microspheres, 0.5 μm	BEISILE	6-3-0050
Critical commercial assays		
Siemens star resolution chart	Shangchen Optics	Siemens star resolution chart
Deposited data		
RUSH3D-2P validation data (this publication)	Zenodo	https://doi.org/10.5281/zenodo.12789868
Experimental models: Organisms/strains		
Zebrafish: Tg(gata1:DsRed)	Anming Meng laboratory (Tsinghua University)	N/A
Zebrafish: Tg(fli:EGFP)	Anming Meng laboratory (Tsinghua University)	N/A
CX3CR1-GFP transgenic mice	The Jackson Laboratory	RRID:IMSR_JAX:008451
Rasgrf2-2A-dCre;Ai148d mice	The Jackson Laboratory	RRID:IMSR_JAX:022864
Oxtr-2A-dCre;Ai148d mice	The Jackson Laboratory	RRID:IMSR_JAX:031303
Vip-IRES-Cre;Ai148d mice	The Jackson Laboratory	RRID:IMSR_JAX:031628
Thy1-YFP-H transgenic mice	The Jackson Laboratory	RRID:IMSR_JAX:003782
Mouse: C57BL/J	The Jackson Laboratory	RRID:IMSR_JAX:000664
Mouse: C57BL/J	Charles River Laboratories	N/A
Mouse: green fluorescent protein (GFP)-expressing	The Jackson Laboratory	RRID:IMSR_JAX:004353
Mouse: dsRed-expressing	The Jackson Laboratory	RRID:IMSR_JAX:006051
Mouse: OVA323–339-specific T cell-receptor transgenic OT-II	The Jackson Laboratory	RRID:IMSR_JAX:004194
Mouse: HEL-specific Ig-transgenic MD4	The Jackson Laboratory	RRID:IMSR_JAX:002595
Software and algorithms		
Image J	NIH Image for the Macintosh	https://imagej.nih.gov/ij/index.html; RRID:SCR_003070
MATLAB	Mathworks	https://www.mathworks.com/products/matlab.html; RRID:SCR_001622
Imaris	Oxford Instruments	https://imaris.oxinst.com/; RRID:SCR_007370
MVGC Multivariate Granger Causality Matlab Toolbox (version mvgc_v1.2)	Barnett and Seth[48]	https://github.com/SacklerCentre/MVGC1/; RRID:SCR_015755
seqNMF	Mackevicius et al.[49]	https://github.com/FeeLab/seqNMF/; RRID:SCR_017068
Demixed PCA (dPCA)	Kobak et al.[50]	https://github.com/machenslab/dPCA
Uniform Manifold Approximation and Projection (UMAP)	McInnes et al.[74]	N/A
PsychToolbox-3	Brainard[75]	http://psychtoolbox.org/; RRID:SCR_002881
3D reconstruction algorithm with wDAO and MBR	This paper	https://github.com/yuanlong-o/RUSH3D
Neuron calcium signal extraction algorithm SSID	This paper	https://github.com/yuanlong-o/RUSH3D

(*Continued on next page*)

Continued

REAGENT or RESOURCE	SOURCE	IDENTIFIER
Other		
2×/0.5 NA Air immersion objective	Olympus	MVPLAPO 2XC
Dichroic mirror	Chroma	ZT405/488/561/640xv2
Excitation filter	Chroma	ZET405/488/561/640xv2
Emission filter	Chroma	ZET405/488/561/640mv2
Microlens array	N/A	Pitch69μm/f=393.3mm/F-num=5.7
Camera	CMOSIS	CMV50000
Tubelens	Thorlab/Edmund/New port	LA1779 (Thorlabs) KCP067 (Newport) LC1315 (Thorlabs) LA1740 (Thorlabs)
RUSH3D body	Thorlabs	CFB1500
Optical table and supports	Thorlabs	B3030F, MB3030_M, P250_M, PH40E_M, etc
Objective arm	Thorlabs	CSA1500, ZFM1020
Tube and cage system	Thorlabs	SM2M20, SM2T10, LC6W, etc.
Linear stage	Thorlabs	LNR25M_M
GPU	Nvidia	RTX3090
CPU	Intel	10900K
SSD	HGST	SN260 SSD ULTRASTAR 7.6TB
RAM	KingSton	32G×32
ThermoStar body temperature maintenance instrument	RWD	https://www.rwdls.com/product/operative/case1/804.html
Multicolor LED	89 North	LDI-488
Two-dimensional piezo actuator	Coremorrow	P33-T2S
Passive grating screen	RaspberryPI	11.6 inch
Silicon APD	Thorlabs	APD430A

EXPERIMENTAL MODEL AND STUDY PARTICIPANT DETAILS

Animals

All the experimental procedures were approved by the Use Committee and Institutional Animal Care at Tsinghua University, Beijing, China.

Neural imaging in mouse

Adult mice (male or female without randomization or blinding) at 8–16 postnatal weeks were housed in an animal facility (24 °C and 50% humidity) under a reverse light cycle in groups of one to five. All imaging experiments were performed with our RUSH3D on head-fixed, awake mice. For functional imaging of neural activity, we used transgenic mice hybridized between Rasgrf2-2A-dCre mice and Ai148 (TIT2L-GC6f-ICL-tTA2)-D mice expressing Cre-dependent GCaMP6f genetically encoded calcium indicator. Briefly, mice were first anesthetized with 1.5% (by volume in oxygen) isoflurane, and an 8.0-mm-diameter craniotomy was made with a skull drill. After removing the skull piece, a coverslip was implanted on the craniotomy region, and a titanium headpost was then cemented to the skull for head fixation. After the surgery, 0.25 mg per gram (body weight) trimethoprim was injected intraperitoneally to induce the expression of GCaMP6f in layer 2/ layer 3 cortical neurons across the whole brain. After inflammation was gone and the cranial window became clear (~2 weeks after surgery), mice were ready for imaging. For RUSH3D imaging, animals were head-fixed on a home-built treadmill underneath the MVPLAPO 2XC mesoscope objective. The head bar clamp pair was mounted on a two-axis goniometer stage for precision tip/tilt adjustment. Using this goniometer, the cranial window was adjusted to be orthogonal to the optical axis of the RUSH3D objective. The treadmill was mounted on a high-precision, three-axis motorized stage (M-VP- 25XA-XYZL, Newport) for sample translation. Calcium imaging at 20 Hz was then performed on awake mice without anesthesia *in vivo*.

Mouse lymph node imaging

C57BL/6 (Jax 0664), yellow fluorescent protein (YFP)-expressing mice (Jax 3782), green fluorescent protein (GFP)-expressing mice (Jax 4353), dsRed-expressing mice (Jax 6051), OT-II mice with $OVA_{323–339}$-specific T cell-receptor transgenes (Jax 4194), and MD4

mice with HEL-specific Ig-transgenes (Jax 2595) were all sourced from the Jackson Laboratory. Relevant mice were interbred to obtain dsRed-expressing and MD4 and GFP-expressing MD4 mice, dsRed-expressing and GFP-expressing OT-II mice. Six to twelve-week-old, age- and sex-matched mice were used for the experiments. For the cell isolation and adoptive transfer, OT-II T and MD4 B cells were isolated from OT-II and MD4 mice, respectively, using the negative CD4 T cell or B cell isolation kit (Miltenyi Biotec).

To examine GC formation by MD4 B cells with the help from OT-II T cells, C57BL/6J mice received a mixture of freshly isolated cells that consisted of GFP-expressing OT-II T cells (0.8×10^5 per recipient), OT-II T cells (3.2×10^5 per recipient), dsRed-expressing MD4 B cells (0.4×10^5 per recipient) and MD4 B cells (3.6×10^5 per recipient). B6 recipients were subcutaneously immunized with 130 μg HEL–OVA conjugated antigen emulsified in 50% alum (Thermo Scientific) with 0.5 μg lipopolysaccharide (LPS, Sigma). HEL-OVA conjugated antigens were made by chemical crosslinking with a HydraLink conjugation kit (SoluLink) as previously described.[76,77]

To examine the migration of OT-II T cells after GC formation, B6 mice received a mixture of freshly isolated cells that consisted of dsRed-expressing OT-II T cells (0.8×10^5 per recipient), OT-II T cells (3.2×10^5 per recipient) and GFP-expressing MD4 B cells (4×10^5 per recipient). Then B6 recipients were immunized as previously described.

The surgical procedure for intravital imaging of the inguinal lymph node was then performed as previously described at the indicated time points.[76,78] Finally, we put the mouse under the RUSH3D for imaging.

Mouse TBI model and imaging

C57BL/6 (8-12 weeks) were anesthetized using isoflurane (2-3%) to incise the scalp for appropriate exposure of the bony skull. For simultaneous imaging of TBI-induced neutrophil-microglia interactions, 10 μl PE-Ly-6G/Ly-6C (eBioscience, 12-5931-82) dissolved in 200 μl physiological saline were injected into the mice by intravenous injection. After that, the anesthetized mice were situated under a device consisting of a metal tube (inner diameter 13 mm) placed vertically over the animal's head. A sponge immobilization board supported the head to allow some head movements during the injury, analogously to the movements occurring during closed head injury in car accidents. The injury was induced by dropping a 25-gram-weight metal from 80-cm height down through the metal tube, striking the skull.

The TIS window was formulated using a trio of reagents: S1, a concentrated supernatant solution comprised of 75% (vol/vol) ethanol (Sinopharm, China) and urea (Sinopharm, China) at ambient temperature; S2, an elevated concentration of sodium dodecylbenzenesulfonate solution, derived from combining a 0.7 M NaOH solution (Aladdin, China) with dodecylbenzenesulfonic acid (Aladdin, China) at a volume-mass ratio of 24:5; and S3, a UV-curable adhesive, notably ergo 8500 (Kisling, Switzerland). The refractive index of S1, S2, and S3 are 1.399 ± 0.0008, 1.364 ± 0.0003, and 1.513 ± 0.0016, respectively. Mice were sedated using a concoction of 2% α-chloralose and 10% urethane, administered at a dosage of 8 mL/kg. Subsequently, S1 was administered to the revealed skull for a duration of 10 minutes, serving to disintegrate the collagen present therein. Following the removal of S1, S2 was liberally applied to effectuate the eradication of lipids. Post S2 elimination, S3 was sparingly applied to achieve refractive index matching, providing a protective sheen to the exposed skull, atop which a 1-mm coverslip was delicately placed. Concluding this procedure, the specified skull region underwent UV LED exposure for a span of 2 minutes, culminating in the solidification of S3.

Zebrafish imaging

Zebrafish from the transgenic line Tg(gata1:DsRed) and Tg(fli: EGFP) were used in this study for blood cell and blood vessel imaging, respectively. The embryos were raised at 28.5 °C in Holtfreter's solution (NaCl 59 mM, KCl 0.67 mM, $CaCl_2$ 0.76 mM, $NaHCO_3$ 2.4 mM) until 4 dpf. Larval zebrafish were paralyzed by ethyl 3-aminobenzoate methanesulfonate salt (100 mg/ L). After being paralyzed, the larval were embedded in 1% low-melting-temperature agarose in a Glass Bottom Dish (35 mm Dish with 20 mm Bottom Well, Cellvis) for live imaging. We maintained the specimen at room temperature and imaged the zebrafish larval at 20 Hz.

Mouse brain slice clearing, immunohistochemical staining, and imaging

Adult mice were anesthetized with 2.5% Avertin solution (0.15 mL/10 g body weight), and transcardially perfused with 0.1 M PBS. After PBS, mice were perfused with 4% paraformaldehyde (PFA) in 0.1M PB. Brains were dissected and post-fixed in 4% PFA overnight at 4°C. After washing in PBS for 1 day (solution changed at 6 h and 12 h), brain samples were embedded in 4% agarose, then were cut into 300 μm∼700 μm brain slices using a vibrating microtome. For slice clearing, brain slices were delipidated with CUBIC-1 solution (25 wt% urea, 5 wt% Quadrol, 15 wt% Triton X-100 in distilled water) for 3 days at room temperature (solution changed at day 2)[35]. Following washing in PBS for 1 day (solution changed at 6 h and 12 h), brain slices were immersed in refractive index matching solution OPTIClear (20 wt% N-methyl-D-glucamine, 32 wt% Histodenz, 25 wt% 2,2-Thiodiethano in distilled water) for 1 day at room temperature[36]. After refractive index matching, a brain slice was mounted on a glass slide and covered with a coverslip for imaging. For immunohistochemical staining, the brain slices were then pre-incubated in 0.5% Triton X-100 in PB for 30 min, and blocked in 5% bovine serum albumin and 0.5% Triton X-100 in PB for 1 h at room temperature (22 °C). Sections were then incubated overnight at 4 °C and two more hours at room temperature in 0.1% Triton X-100 containing primary antibodies. After washing with 0.1 M PBS, sections were incubated for 2 h at room temperature in 0.1% Triton X-100 containing secondary antibodies.

METHOD DETAILS

Experimental setup

The RUSH3D excitation path consists of a mounted multicolor LED (LDI-488, 89 North), adjustable asphere collimator (F240SMA-532, Thorlabs), an iris aperture for adjusting illumination NA, an illumination tube lens (Thorlabs AC508-75-A), an excitation filter (ZET405/488/561/640xv2, ⌀ 2", Chroma), and a macro objective (MVPLAPO 2XC, Olympus). A two-dimensional piezo actuator (P33_T2S, Coremorrow) is centrally positioned on a 50 × 70mm dichroic mirror (ZT405/488/561/640, 50 × 70 mm, Chroma) to manipulate the dichroic for emission beam scanning, resulting in a sub-microlens scale shift. The excitation beam was strategically placed off the optical axis of the objective to avoid obstruction by the piezo actuator (Figure S1B). This arrangement provides near-homogeneous illumination in the focal plane in the sample. Maximum illumination power was about 58 mW post-objective, which corresponds to about 1.2 mW/mm^2, a value comparable to our previous LFM imaging methods and typical wide-field imaging protocols for low-phototoxicity imaging[79] (Figure S1B).

The RUSH3D emission path consists of a customized tube lens (Figure S1B), an emission filter (ZET405/488/561/640mv2, ⌀ 2", Chroma), microlens array (square grid, 69-μm pitch size, 393.3-μm focal length, F-number 5.7), and 12-bit camera (CMV50000, 7,920 × 6,004 pixels, 4.6-μm pixel pitch, 30-Hz full frame rate, CMOSIS). The custom-designed tube lens was specifically optimized to correct its inherent aberrations, based on the telecentric incident rays. The pitch size of the MLA is set to match the size of 15 × 15 sensor pixels, corresponding to 225 angular measurements. The centimeter FOV is characterized by the diagonal length of the FOV spanning 8 by 6 mm. A part list of RUSH3D can be found in key resources table.

Pixel realignment

Pixel realignment functions as an essential preprocessing operation, transforming the unprocessed measurements of the RUSH3D into phase space. A procured frame can be characterized as $F(x,y,u,v,t)$, where (u,v) indicate the relative position of sensor pixels after each microlens, corresponding to the angular coordinates, and (x,y) signify the center position of each microlens, corresponding to the spatial coordinates.

Limited by the physical size constraints, the minimum sampling step on the sample side of a conventional LFM is restricted to the diameter of the microlens.[80] Therefore, we proposed a scanning light-field imaging (sLFM) framework to address the frequency aliasing problem, which can recover the resolution of LFM up to the diffraction limit, while maintaining the high 3D imaging speed.[21] In the context of sLFM, samplings from an identical view (u,v) within a scanning duration are collated to yield high-resolution spatio-angular measurements $F_h(x,y,u,v,t)$. This aforementioned protocol is designated as pixel realignment. Only 3 × 3 scanning is required to recover the full resolution with the angular resolution of 15 × 15. The sliding window technique was incorporated in the temporal domain, ensuring the preservation of the majority of temporal information,[21] contingent on a window size equivalent to the scanning period (for instance, 9 frames for a 3 × 3 scanning).

Prior to realignment, the raw light-field image undergoes resizing and rotation to ensure each microlens encompasses 15 × 15 sensor pixels. This rectification process is critical in calibrating systemic discrepancies induced by alignment and microlens fabrication, thereby augmenting the robustness of subsequent image processing. Collectively, rectification and pixel realignment of a single frame within a 3 × 3 scanning configuration of RUSH3D require approximately 0.3 seconds on a standard desktop computer furnished with a graphical processing unit (AMD EPYC 7H12 CPU 2.60 GHz, 64 cores, 1 TB RAM, NVIDIA GeForce RTX3090).

Wave-optics digital adaptive optics (wDAO)

To address the spatially nonuniform optical aberrations induced either by imperfect optical systems or by heterogeneous intravital environment, RUSH3D employed wDAO.

The wDAO correction in RUSH3D can be divided into 3 steps. In the first step, we calibrated the shift map of the RUSH3D optical system (Figure S1Di). The system's positional aberration can be reflected in the disparity of a 2D planar sample (such as a resolution chart) in different views (i.e., after pixel realignment). To calibrate these aberrations, we employed a non-rigid registration algorithm in each tile of the field of view (FOV) (Figure S1Di). During each iteration round, we initially measured the disparities between the central view and a non-central view of a planar calibration chart. Consequently, for each view, a 2D vector would represent the relative shifts between it and the central view. The collection of these 2D vectors is referred to as the shift map, spanning a size of $N_{tx} \times N_{ty} \times 2 \times V \times V$, where N_{tx} and N_{ty} represent the tiling setups, and $V \times V$ denotes the view numbers. To reduce discontinuity between adjacent tiles, we up sampled the shift maps, changing their dimensions from $N_{tx} \times N_{ty} \times 2 \times V \times V$ to $N_x \times N_y \times 2 \times V \times V$, where $N_x \times N_y$ signifies the global pixel number of the RUSH3D. Subsequently, the shift maps were inversely applied to the captures of each view on a pixelwise basis, and correlations between each view and the central view were measured. If the correlation exceeded a predetermined threshold (θ), the algorithm would terminate and output the shift map; otherwise, it would proceed to the next iteration to reduce the errors in disparity estimation. The calibrated shift map of RUSH3D can be found in Figure S1Di.

In the second step, we calibrated the system aberrations of RUSH3D and generated aberrated PSF (Figure S1Dii). We partitioned the shift map into $N_{tx} \times N_{ty}$ tiles (in our experiment, $N_{tx} = 4$ and $N_{ty} = 3$), calculated the mean values across these tiles for each view to procure a $N_{tx} \times N_{ty} \times V \times V$ subset, and subsequently employed a shift-to-wavefront-gradient function to compute the initial guess of phase gradients for each $N_{tx} \times N_{ty}$ tile.[16] Following this, the aberrated phase was ascertained for each tile. Throughout every iteration, we initially integrated the phase gradients *PGra* in the spatial domain to derive an estimate of the aberrated phase, followed by a fitting

of the phase using Zernike polynomials to smooth the phase distribution. We proceeded to generate the point spread function (PSF) predicated on the fitted phase and light field imaging model. In consequence, we assessed the shift $S(v)$ of the PSF at the focal plane ($z = z_0$) between different views, and correspondingly generated phase gradients to estimate the residual phase gradients for an iterative update. The iteration ceases once the residual phase gradient is less than the threshold for a specific tile. The aberrated phase of each tile serves as the output of the second step, with the corresponding aberrated PSF subsequently being generated and incorporated into the reconstruction phase (Figure S1Dii).

In the third step, we employ the previously estimated aberrated PSF and DAO algorithm to reconstruct the captured volume (Figure S1Diii). This iterative process chiefly adheres to the phase-space deconvolution with DAO.[21] Differently, for each FOV tile, the aberrated PSFs are utilized to update the estimated volume. Ultimately, the twelve sub-patches of each region of interest are seamlessly amalgamated. The above procedure can be described through following calculations:

$$Vol^{k}_{j+1}(x,z) \leftarrow w_{v_j}\frac{Vol^{k}_{j}(x,z)\cdot G_{corr}(x,z)}{J * H^{T}(x,z,v_j)} + (1 - w_{v_j})Vol^{k}_{j}(x,z) \quad \text{(Equation 1)}$$

$$G_{corr}(x,z) = \frac{M(x,v_j)}{P(x+ShiftMap^{k-1}(x,v_j))} * H^{T}(x,z,v_j) \quad \text{(Equation 2)}$$

$$P(x) = \int_{z} Vol^{k}_{j-1}(x,z) * H(x,z,v_j)dz \quad \text{(Equation 3)}$$

where j corresponds to the index of the angular component v_j, $\cdot$ represents the dot product process, $*$ represents the 2D convolution process in the lateral domain (applied only to x), $Vol^{k}_{j}(x,z)$ is the estimated volume, J represents the all-ones matrix, $M(x,v_j)$ is the angular measurement, $ShiftMap^{k-1}(x,v_j)$ represents estimated disparities in view v_j, and w_{u_j} is the weight used to balance the different shot noise for different spatial frequency components. $H(x,z,v)$ and $H^{T}(x,z,v)$ respectively represent the PSF and its transposition of the angular component. In addition, w_{v_j} is calculated based on the energy distribution of the PSFs along different angles:

$$w_{u_j} = c\frac{\|H(x,z,u_j)\|_1}{\sum_{u_k=u_1}^{u_N}\|H(x,z,u_j)\|_1} \quad \text{(Equation 4)}$$

where c is the coefficient to balance the convergence rate and performance, which depends on the number of angular components. We chose $c = 1.0$ for all of our experiments because the number of angular components in our setup is 225.

Multiscale background rejection (MBR)

Since light-field measurement can provide accurate estimation of the spatially nonuniform background fluorescence due to the extended depth of field, we use a multiscale model here to achieve computational optical sectioning as our previous work describes.[23] Considering the reduced resolution far from the native objective plane, the raw phase-space measurements were firstly down sampled for initiating a quick yet axially extended 3D reconstruction to adequately model only the background without foreground signals. Within this reconstruction, the signal planes are centrally located, characterized by higher intensity (solid blue lines in Figure S2A), while the background planes reside on either side, marked by comparatively lower intensity (dashed blue lines in Figure S2A). Subsequently, these background planes are back-propagated into the light field space, resulting in background-only views. Then, those background views were differentiated with the original defiled captures to generate background-removed light field frame, facilitating the genuine 3D reconstruction of samples combined with wDAO.

Motion corrections

For highly dynamic samples moving during the scanning process of RUSH3D, motion artefacts arise after pixel realignment. We adopted previously developed temporal correction algorithms, i.e. time-weighted algorithm,[21] for RUSH3D.

The time-weighted algorithm[21] leveraging a spatiotemporal smoothness prior, facilitates the removal of such artifacts. The underlying assumption of this prior is that most biological specimens exhibit smooth changes at moderate time scale, ensuring spatiotemporal continuity, especially given the high volumetric imaging rate of RUSH3D. After realigning pixels for each timestamp, the high-resolution angular measurements consist of nine (assuming a 3 × 3 scanning matrix) low-resolution subimages from different scanning positions. For instances of minimal motion, the pixel values of the frame are directly utilized. Conversely, in scenarios of significant motion, the pixel values for each frame are estimated using adjacent sampling points, a method frequently employed in geographic studies with discrete samplings. The effectiveness of the time-weighted algorithm has been demonstrated in capturing images of freely swimming jellyfish (Figure S1H), markedly reducing motion artifacts and preserving structural integrity.

Sparse seeded iteration demixing (SSID) pipeline

The SSID workflow bifurcates into two segments: initial seed generation and ensuing iterative demixing. In the seed generation stage, all frames are initially aligned according to scanning angles (v coordinate), followed by temporal alignment (t coordinate) without using temporal sliding window, which is denoted as the low-temporal resolution and high-spatial resolution (LTHS). Primarily, raw recordings undergo MBR to mitigate background interference. The enhanced footage is subsequently subjected to motion correction via the open-source NormCorre algorithm.[81] A standard deviation projection across the temporal channel of the adjusted footage is then implemented to compose a summary image, further reconstructed with the enhancement of wDAO. The bright neurons within the reconstructed expanse are subsequently subjected to morphological segmentation, establishing initial seeds for the impending optimization process:

$$\max_{(ij)} \frac{I_S * d|(i,j)}{I_S * d_S|(i,j)} \quad \text{(Equation 5)}$$

where $d = e^{-\frac{x^2+y^2}{\sigma_1^2}}$, $d_S = e^{-\frac{x^2+y^2}{\sigma_2^2}} - e^{-\frac{x^2+y^2}{\sigma_1^2}}$, σ_1 is expected neuron radius and $\sigma_2 > \sigma_1$ is the radius of the surrounding region. Temporal activities of these seeds are initialized through the examination of pixel fluctuations within the enhanced footage.

For iterative demixing, all frames are assembled and a sliding window is imposed to optimize temporal resolution, which is denoted as the high-temporal resolution and low-spatial resolution (HTLS). Similar to the prior process, raw recordings first undergo MBR for background elimination. Following this, the enhanced footage is subjected to motion correction via the open-source NormCorre algorithm. An optimized iterative demixing step, involving only 13/255 of the comprehensively captured angular data, was subsequently implemented with the aforementioned seeds. The spatial and temporal components were alternately updated whilst maintaining the other constant, following the non-negative matrix factorization (NMF)[82]

$$\mathbf{M_j} = [A_1, \ldots, A_N] \cdot [F_1, \ldots, F_N]^T \quad \text{(Equation 6)}$$

where $\mathbf{M_j}$ is the MBR-enhanced measurement from each view, $A_1, \ldots, A_N$ are the estimated spatial footprints from segmentation, and $F_1, \ldots, F_N$ are the corresponding temporal signals. Signals from core and shell components are demixed based on the following optimization

$$\min_{c_i, s_i} \|F_i - s_i * k_i - c_i N_i\|_2^2 + \lambda \|s_i\|_0 \quad \text{(Equation 7)}$$

where F_i is the activity trace from i-th neuron soma, N_i is the trace from the neuropil region surrounding the i-th neuron, s_i is a binary time series containing the underlying action potential events and k_i is the GECI response kernel to an action potential. The coefficients c_i are introduced to allow matching the amplitude of neuron and neuropil traces. The above non-convex optimization problem attempts to obtain minimal loss by finding the correct s_i and c_i. The demixed spatial footprints and temporal activities of the neurons are finally output for analysis.

Simultaneous RUSH3D and two-photon joint validation

To verify the proposed RUSH3D in achieving correct structure and signals, we built a joint two-photon and RUSH3D imaging system. The system was modified from RUSH3D system, where we added a 920-nm centered two-photon excitation and detection path in the system.

For the two-photon excitation path, a titanium-sapphire laser system (MaiTai HP, Spectra-Physics) served as the two-photon excitation source (920 nm central wavelength, pulse width <100 fs, 80 MHz repetition rate). A half-wave plate (AQWP10M-980, Thorlabs) and an electro-optic modulator (350-80LA-02, Conoptics) were used to modulate the excitation power. A 4f system (AC508-200-B and AC508-400-B, Thorlabs) with a 2x magnification was used to expand the laser beam to a resonant scanner (8315K/CRS8K, Cambridge Technology). The scanned beam went through a scan lens (SL50-2P2, Thorlabs) and a tube lens (TTL200MP, Thorlabs) and formed a tight focus through the objective of RUSH3D.

To separate the two-photon excitation beam with original RUSH3D excitation beam and fluorescent emission path, a long-pass dichroic mirror (DMLP650L, Thorlabs) was introduced. Then, we put the second dichroic, which is the RUSH3D dichroic after the two-photon long-pass dichroic. In RUSH3D path, we replace the original 4-color dichroic by a long pass dichroic (DMLP505L, Thorlabs), while keeping the other setup consistent.

To jointly record RUSH3D excitation and two-photon excitation, a 50:50 (reflectance: transmission) non-polarizing plate beam splitter (BSW27, Thorlabs) was placed after the RUSH3D dichroic to separate fluorescent signals for PMT (PMT1001, Thorlabs) and camera, respectively. A pair of fluorescence filters (MF525-39, Thorlabs; ET510/80M, Chroma) was configured in front of both the PMT and the camera to fully block both femtosecond laser and RUSH3D excitation beam. The back aperture of the objective was optically conjugated to the detection surface of the PMT with a 4f system (TTL200-A and AC254-050-A, Thorlabs).

To avoid excitation crosstalk and protect PMT from high-flux RUSH3D emission photons, we added a linear galvo that served as an optical shutter for the PMT detection path, which deflected RUSH3D fluorescent photons when LDI source was on. We further configured the EOM to be blocked during RUSH3D imaging. The LDI source was in trigger mode with a typical rising and falling time less than 1 ms, with further reduced duration time to avoid PMT overexposure. Both two-photon and RUSH3D captures were at 10 Hz.

To introduce an offset between the two-photon focal plane and the RUSH3D focal plane for investigating RUSH3D performance across different cortical depths, we incorporated an electrically tunable lens (El-16-40-tc-lens, Optotune) before the resonant galvo, which decoupled the position of the two-photon focal plane from the RUSH3D focal plane, thus enabling us to sweep the two-photon plane across different cortical depths while keeping the RUSH3D detection volume fixed at a given axial position in the mouse brain. For each imaging session, we conducted five sub sessions; within each sub session, we maintained the RUSH3D focal plane at 150 μm below the dura, while shifting the two-photon focal plane using the electrically tunable lens to depths below the dura of 100 μm, 125 μm, 150 μm, 175 μm, and 200 μm. We rapidly alternated between one- and two-photon excitation to acquire two-photon and RUSH3D signals nearly simultaneously on the timescale of calcium indicator dynamics. In this manner, we could directly evaluate RUSH3D's performance across different imaging depths.

RUSH3D operation protocols

Assembly and data acquisition guidance

Camera and MLA assembly ● Timing 1–2 h

Step 1. Begin by disassembling the CMOS sensor and removing its protective cover glass. Attach a CNC-machined arm, which holds the microlens array (MLA), to a 5-axis mechanical stage (Thorlabs PY005/M), ensuring the MLA aligns parallel to the sensor surface. It is crucial to handle the MLA with care, given its focal length is under 400 μm, to avoid damaging the sensor's surface. All pertinent mechanical design files are accessible via the provided GitHub link.

Step 2. Precisely adjust the 5-axis mechanical stage to achieve exact parallel alignment of the MLA with the sensor surface, which is important for the subsequent acquisition and reconstruction processes. Utilize a camera lens to capture an image for adjusting. By adjusting the tip and tilt of the MLA, ensure the image remains focused across the entire field of view (FOV). The circle pattern produced by each microlens serves as a criterion for assessing focus sharpness, which should be neither overlapped nor separated. Furthermore, modify the MLA's rotational angle to align the MLA grid with the camera pixel grid. Minor adjustments to the distance between the camera and the MLA can fine-tune each microlens to precisely cover a 15 × 15 sensor pixel area.

Step 3. Inspect the MLA and camera sensor for dust particles. Should any be found, clean the MLA using a gas duster (Thorlabs CA4-US) and the camera either with the same gas duster or cotton swabs lightly moistened with ethanol. Dust and debris may cause dark points on the image identified as 'outliers', which can be mitigated through median filtering techniques.

Optical alignment ● Timing 2–4 h

Step 4. Construct the optical path following the CAD file. It is recommended to start by assembling the support rail and camera platform breadboard, then proceed with establishing the excitation pathway, and conclude with the detection pathway assembly.

Step 5. To fabricate the excitation pathway, initially machine the specifically designed holder for the 2D piezo actuator (P33_T2S, Coremorrow) utilizing CNC technology. Subsequently, affix the multicolor dichroic mirror (ZT405/488/561/640, 50x70 mm, Chroma) centrally to the actuator using optical adhesive. Proceed to assemble the microscope arm, cage system, and actuator-dichroic assembly. Integrate fiber illumination (LDI-488, 89 North), ensuring the excitation beam's path remains unobstructed by the actuator. Position a fluorescent microscope slide (FSK3, Thorlabs) on the microscope as a calibration sample. Fine-tune the illumination fiber's height to achieve uniform light distribution across the slide.

Step 6. For the detection pathway construction, start by assembling the tube lens as shown in Figure S1. Align the tube lens concentrically with the excitation cage system. Position the assembled camera atop a 2D mechanical stage (LNR25M_M, Thorlabs), ensuring the camera's aperture is concentrically aligned with the tube lens for optimal detection efficiency.

Software installation and hardware synchronization ● Timing 2–3 h

Step 7. The computer specifications we used for running this software are as follows: 1) NVIDIA GeForce RTX 3090 graphics card, 2) 128 GB RAM, 3) 2 TB solid-state drive (SSD), 4) 144 Hz monitor, alongside standard compatible components. The software is designed to facilitate real-time data transfer from the buffer cache directly to the SSD, minimizing RAM usage. For extended imaging sessions, the integration of a Network Attached Storage (NAS) system is strongly recommended for efficient long-term data management. Upon configuring the computer, proceed with the installation of essential software and drivers: 1) Install Visual Studio, CMake, and OpenCV. 2) Install the NVIDIA GPU driver and CUDA Toolkit 9.1. 3) Install LabVIEW and NI DAQmx for data acquisition support. 4) Install MATLAB for data analysis and visualization. Next, download the Supplementary Software package. Before extracting the contents, ensure to disable the virus and threat protection feature in Windows Security to prevent any interference. After unpacking, initiate the setup by running the 'sLFdriver.exe' executable. This comprehensive setup ensures the system is fully equipped to handle the software's demands, allowing for seamless operation and data processing.

Step 8. Configure the camera and synchronization settings, including the exposure time, imaging velocity, and scanning methodology. Typically, the scanning configuration is adjusted to a 3 × 3 matrix for the majority of specimens. Within Light Field Microscopy (LFM) operations, scanning cessation is achievable by setting the Nshift and k parameters to 1 within the software interface. Adjust the trigger delay time to a minimum of 1 ms to ensure adequate stabilization time for illumination transitions and piezo scanning activities. The loop delay feature accommodates experiments not requiring rapid imaging techniques. Introducing a temporal gap between distinct volumetric scans can aid in mitigating phototoxic effects. Activate the live mode for real-time multiview visualization by selecting the 'OpenCam' option and marking the 'realign' checkbox to pinpoint the desired field of view (FOV). To enhance channel visualization, adjust contrasts automatically by clicking the 'auto' button adjacent to each channel. Input the desired quantity of scanning light-field images in the 'Image Num' field. Deactivate live mode by selecting the 'CloseCam' button. Engage the data-saving feature,

which also supports real-time multiview rendering, by clicking the 'SaveStart' button after specifying file names in the 'Save Name' input area. The software automatically appends the scanning mode, camera exposure details, and laser channel information to the file name to facilitate post-processing and automatic pixel realignment. Additionally, a video skim of the central view from the raw light-field data, showcasing low-resolution average intensity projections, is saved to offer immediate experimental feedback to users.

Calibration of scanning voltage of the 2D scanner ● Timing 1 h

Step 9. Position a resolution chart on the microscope stage as a typical sample. Apply the minimum and maximum control voltages to the first channel of the 2D scanner, maintaining constant voltage on the second channel, to gauge image shifts in both the X and Y axes. Subsequently, administer the minimum and maximum control voltages to the second channel of the 2D galvanometer scanner, this time keeping the first channel's voltage steady, and measure the image displacement in the X and Y directions once more.

Step 10. Derive the specific 2D voltages necessary to effectuate a one-pixel image shift in both the X and Y orientations. Utilize the displacement measurements from the preceding steps to formulate the equation for calculating shifts that correspond precisely to one camera pixel.

Step 11. Employ the voltages ascertained in the previous steps to conduct scanning light-field imaging.

Apparatus for stimulus delivery and behavioral tracking in mouse neural imaging

Visual and somatosensory stimuli were controlled via a pre-programmed pulse table generated by National Instruments DAQ cards in the experiment control PC. Drifting grating video was generated with PsychToolbox-3.[75] For whisker stimulation, an Arduino microcontroller with a motor shield and servo motor was employed to move a brush forward and backward over the animals' whiskers at time intervals indicated by the stimulation protocol. The brush size and its proximity were chosen to stimulate all whiskers simultaneously (as opposed to stimulation of specific whiskers), and stimulation was applied contralaterally to the hemisphere being recorded by the microscope.

All rodents were head-fixed on a home-built treadmill with a rotation encoder affixed to the rear axle (Broadcom, HEDS-5540-A02) to measure the relative position of the treadmill during the recordings. Treadmill position, the microcontroller clock value, and the onset of a whisker stimulus were streamed to the control computer via a serial port connection and logged with a separate data logging script. The data logging script also read out frames from a camera (Logitech 860-000451) in order to capture additional animal behavior during recordings. Motion energy for manually defined regions of interest (e.g., front paws, nose tip) were computed from the behavior videos using the Facemap Python package[83] as the magnitude of the difference between each frame and a block wise mean frame.

Data management and hardware of RUSH3D computational pipeline

Data was acquired from the camera onto a control workstation (AMD EPYC 7H12 CPU 2.60 GHz, 64 cores, 1 TB RAM, Windows 10) configured with a 7.6TB SSD (SN260 SSD ULTRASTAR), using a custom data acquisition application written in VisualC#.NET. The single frame can be read out at 20 fps, resulting in a raw data rate of ~2.5 GB/s. At the end of each imaging session, the raw data was transferred via 10 Gbit/s network links to a network-attached storage server (Synology RS3618xs). The RUSH3D computational pipeline was run on the same computers equipped with an RTX 3090 GPU.

Running the RUSH3D analysis (15-minute recording) took a total of 19.6 CPU core-hours and 9.2 GPU-hours, as tracked using the pidstat command. For each reconstruction cycle, it took approximately 5 minutes, utilizing 20.0 GB of GPU memory, 12.5 GB of workstation memory, and an average of less than 10% CPU usage. The peak memory consumption reached 20 GB RAM. Note the time includes loading the raw data from the network-attached storage server, which accounts for about 25% of the total run time and can be accelerated by holding data on local SSD disks. The full analysis run was completed within 19 hours and 36 minutes.

QUANTIFICATION AND STATISTICAL ANALYSIS

Statistical analysis

All the statistical tests were performed by Matlab R2021a (Mathworks). Normally distributed data were presented as mean values together with the standard deviation. All of the statistical details of experiments, specifically the size and type of individual samples, *n*, were indicated and specified in the figure legends.

Data throughput comparison

We juxtapose the data throughput of RUSH3D against a spinning disk configuration outfitted with a 2048 × 2048-pixel camera operating at 100 Hz, supplemented by an objective of 20x NA 0.4 (e.g., ACH N POL 20x Objective, Olympus). The rationale behind the selection of this specific objective is its capacity to generate a comparable axial resolution (6.3 μm) to that of RUSH3D (6 μm). To bridge the resolution gap between the confocal system and RUSH3D, the camera would necessitate 2 × 2 binning, yielding an approximate lateral sampling of 2 μm, contrasted against the RUSH3D's figure of roughly 2.6 μm. Under such parameters, the spinning-disk system operates at a frame rate of 200 Hz with a FOV of approximately 1.3 mm × 1.3 mm.

In this context, the spinning disk setup would require 2130.2 scans to access a single volume that a single RUSH3D frame (8 × 6 × 0.4 mm^3) could cover. Given that RUSH3D operates at a frame rate of 20 Hz, it is approximated that the spinning disk system's imaging speed would be slower by a factor of 213 when covering the same volume as the RUSH3D.

We further benchmark the data throughput of various mesoscopes. We computed the effective spatial-bandwidth product (ESBP) employing the following mathematical formulation tailored for a 2D imaging system:

$$\mathrm{ESBP} = \frac{\mathrm{FOV}}{\left[\max\left(s_{xy}, \frac{\lambda}{4NA}\right)\right]^2} \quad \text{(Equation 8)}$$

And accordingly, for a 3D imaging system:

$$\mathrm{ESBP} = \frac{\mathrm{FOV}}{\left[\max\left(s_{xy}, \frac{\lambda}{4NA}\right)\right]^2} \cdot \frac{\mathrm{DOF}}{s_z} \quad \text{(Equation 9)}$$

where DOF is the depth-of-field, s_{xy} and s_z are the lateral and axial sampling size. For our RUSH3D system, the s_{xy} and s_z values were calculated based on averaged resolution across the whole imaging volume. Consequently, the effective pixel or voxel acquisition rate is determined by multiplying the ESBP by the frame rate.

Correlation score

We used Pearson's correlation coefficient as the temporal metric to monitor the similarity between inferred neuronal activities and ground truths. The ground truth activities were available for simulation data. Pearson correlation coefficient (R) was used as the performance metric, which is formulated as

$$R = \frac{E\left[(x - \mu_x)(y - \mu_y)\right]}{\sigma_x \sigma_y} \quad \text{(Equation 10)}$$

where x and y are the denoised data and corresponding high-SNR data, respectively; μ_x and μ_y are the mean values of x and y; σ_x and σ_y are the standard deviations. The operator E represents arithmetically averaging. Pearson correlation was used for both images and fluorescence traces. All performance metrics were implemented with custom Matlab scripts and built-in functions.

Neuron extraction scores

In simulation data, a customized script in MATLAB automatically evaluated segmentation by the following rules: a candidate is a correct segment (true positive, TP) if the minimal distance between this candidate with any ground truth segments is less than 8 μm, and the Intersect over Union (IoU) score between this candidate and that ground truth segment is larger than 0.2. Otherwise, the segmentation candidate will be rejected as a false positive (FP). Segments that appear in ground truth labeling but are not recognized by the algorithm will be marked as false negatives (FN). The segmentation accuracy (F score, $F1$) is defined as

$$F1 = \frac{2TP}{2TP+FP+FN} \quad \text{(Equation 11)}$$

The segmentation precision score is defined as

$$Presicion = \frac{TP}{TP+FP} \quad \text{(Equation 12)}$$

The segmentation sensitivity score is defined as

$$Sensitivity = \frac{TP}{TP+FN} \quad \text{(Equation 13)}$$

Signal-to-background ratio

We calculated the signal-to-background ratio (SBR) of a neuron by computing the average activity of the neuron area (signal intensity) over the average activity of its neighboring area (background intensity) across all temporal frames. The neuron area is defined by a circle that had a radius of 10 μm and is centered at the centroid of a segment. A neighboring area is defined by a ring with an inner radius of 10 μm and an outer radius of 20 μm at the same center of the corresponding neuron area while masking out all other neuron areas. Then, the SBR is calculated by

$$SBR = 10\log_{10}\frac{Signal\ Intensity}{Background\ Intensity} \quad \text{(Equation 14)}$$

Signal-to-noise ratio

We quantitatively evaluate the performance of RUSH3D in noisy conditions. The noise scale is measured by signal-to-noise ratio (SNR), which is calculated by

$$SNR = 10 \cdot \log_{10} \frac{\|x\|_2^2}{\|x - y\|_2^2} \quad \text{(Equation 15)}$$

where x is the denoised data, and y is the ground truth.

Structure similarity (SSIM)

SSIM is a widely used full-reference metric for assessment of visual quality of images and remote sensing data. We called ssim function in MATLAB to calculate the similarity between PSFs from different spectrums or similarity between reconstructed images and ground-truth images.

Peak-signal-to-noise-ratio (PSNR)

PSNR is an engineering term for the ratio between the maximum possible power of a signal and the power of corrupting noise that affects the fidelity of its representation. We called psnr function in MATLAB to calculate the similarity between reconstruction images and ground-truth images.

Quantification of neural activities

To screen stimulus or running state selective neurons (Figures 4A–4F and S6A–S6F), we first computed trial-average activity of all neurons. Trials were aligned to the stimulus onset or the running onset (transition time point in which running speed is over 1 cm/s). We first selected neurons with activity that is significantly different from the baseline (by comparing activity before (-2 $\sim$ 0s) and after (0s $\sim$ 2s) onset, $p<0.05$, Wilcoxon rank sum test). Neurons were further divided into the activated or suppressed neuron groups based on whether their activity was increased or reduced compared with the baseline. To identify neurons with stimulus response modulated by running (Figures 4G, 4H, and S6E), we compared stimulus-evoked activity between the stationary (running speed < 1 cm/s) and running (running speed ≥ 1 cm/s) conditions. This comparison was performed on trials with unisensory or multisensory stimulus for each neuron using the same statistical protocol. Locomotion modulation index was calculated using activity on running trials (R_{loc}) and on stationary trials (R_{quiet}) as

$$Modulation\ index = \frac{R_{loc} - R_{quiet}}{R_{loc} + R_{quiet}} \quad \text{(Equation 16)}$$

To examine the stability in neural response to each moving grating stimulus, we clustered neurons into 4 groups (g1-g4, Figures 5E–5L and S6H) with increasing response stability (g1: responsive in 20-25 trials, g2: 25-30 trials, g3: 30-35 trials, g4: 35-40 trials, n = 66, 53, 50, 44, 72, 54, 63, 70 trials for each orientation in 3 days). OSI of responsive neurons was calculated by comparing the response in the preferred orientation (R_{pref}) and that in the orthogonal orientation (R_{orth}):

$$OSI = \frac{R_{pref} - R_{orth}}{R_{pref} + R_{orth}} \quad \text{(Equation 17)}$$

The correlation coefficient (Figure 5G) was calculated between the subsets of the odd and even trials on each recording session. The consistency of visual response within a day (r_{within}) for each neuron was calculated as the Pearson correlation between the averaged visual firing patterns from odd trials and those from even trials. The consistency of visual response across days (r_{across}) was calculated as the Pearson correlation of the firing patterns between the reference recording session (the first day of recording in our analysis) and the following sessions. To compare r_{within}, r_{across} and a random level of response, the order of orientation was randomly shuffled, and the $r_{shuffle}$ of each neuron was calculated as the Pearson correlation between the average randomized visual firing patterns from odd and even trials.

Granger causality analysis

To infer the causal relationship in activity along the anterior-posterior (AP) axis, we divided the cortex-wide neuron population into 10 uniform bins along the AP, and analyzed the Granger causality among these 10 groups of neurons (Figure 4E). The multivariate Granger causality toolbox (version mvgc_v1.2) was used for Granger causality analysis[48] (https://github.com/SacklerCentre/MVGC1/). The input matrix, encompassing three dimensions, is formulated from the regressed activity (derived from the principal component of temporal sequences) of neurons activated during running. This matrix pertains to each bin observed during running trials, spanning a time frame from -2s to 2s, synchronized with the onset of running. This multivariate Granger causality toolbox computes Granger causality based on vector autoregressive modeling. The number of time lags (model order) was estimated by Akaike information criteria with the maximum set to 20. Pairwise conditional causality was then calculated. The pairwise causality contains directional information: the direction 'from' an X module 'to' a Y module indicated that the activity in the X preceded that in Y. Granger causality values that reached $P < 0.05$ (Granger F test) after using the false discovery rate for multiple-comparison correction are shown in Figure 4E.

Motif analysis

We used the seqNMF algorithm[49] (MATLAB toolbox from https://github.com/FeeLab/seqNMF/) to capture the anterior-posterior activity motifs during the station-locomotion transition. This method uses convolutional nonnegative matrix factorization with a penalty term to facilitate discovery of repeating sequences. We first collected running trial activity (-2s - 2s, aligned to running onset) of all running activated neurons, and split them into two halves for calculating motifs or quantifying significance with Bonferroni correction (SeqNMF test significance, $p < 0.05$). Thus, the input matrix and test matrix were N (neurons) $\times$ T (repeated time sequence of running

trials). This matrix can be factorized into a set of K smaller matrices of size $P \times L$ representing repeated sequences ('motifs'), which structured a tensor termed $W\ (K \times P \times L)$. Here, P represented the weights of neurons at frame L of motif K. In our study, the K value was set as 10 (10 motifs), and L was set to 60 frames (4 seconds). We further calculated the mean value L of neurons in each anterial-posterial (A-P) bins at each frame. Frame-wise normalized mean value of each bin during -2s- - 0.8s was shown in Figure 4F. The motif matrix W was found using a multiplicative update algorithm with over 100 iterations.

Computation of d' for neural responses to multisensory stimuli

To evaluate the information encapsulated by the dynamics of the neural ensemble pertaining to either the visual or whisker stimulus, we employed the partial least squares analysis (PLS).[4] This supervised method facilitated dimensionality reduction, which was subsequently followed by optimal linear decoding within the context of this reduced dimensionality. This process allowed us to ascertain d'—a metric indicative of the precision with which the two stimuli could be differentiated based on the activity trajectories of the neural ensemble. The computation of d' predominantly adheres to the methodology delineated in prior literature.[4]

Demixed principal component analysis (dPCA)

We used the Demixed PCA[50] (MATLAB toolbox from https://github.com/machenslab/dPCA) to derive the response pattern of visual and whisker stimulus (Figure 4K). The objective is to deconstruct the neuronal response data into latent components (dPCs) that (a) are readily interpretable about the various stimuli modulation, and (b) maintain the integrity of the original data, ensuring no pivotal information is discarded. Neurons showcasing marked differences ($p<0.05$, using the Wilcoxon rank sum test) between their baseline activities (-2s to 0s) and their responses to both visual and whisker stimuli (0 s to 2 s) were earmarked as pertinent neurons. Subsequently, we collated the activity from the stimulus trials (spanning 0s to 3s, synchronized to the stimulus onset) pertaining to these pertinent neurons. From this, we derived the dPCA components, which encompass visual-stimulus-dependent components, whisker-stimulus-dependent components, and components dependent on both visual and whisker stimuli (Figures 4K and S6G).

Cross-session neuron registration

Our methodology entailed a dual-phase spatial registration process for datasets stemming from discrete imaging sessions.

Initially, we computed the spatial cross-correlation functions between specific image patches (each measuring 200 μm × 200 μm) within the maximal projection images extracted from the Calcium videos from the inaugural imaging session and its succeeding ones. The subtle day-to-day shifts in each patch's coordinates were ascertained by identifying, for each session, the displacement value resonating with the peak amplitude in the cross-correlation function. Progressively relocating the patch's position across the field of view, and calculating the spatial cross-correlations for each such alteration, facilitated the formation of maps delineating spatial shifts throughout the imaging domain. Subsequently, neurons from ensuing sessions were accurately mapped to the primary session.

During the subsequent phase, we discerned a spatial affine transformation, aligning the segmented neuron 3D coordinates, utilizing the point-set registration method in MATLAB. To appraise the efficacy of our spatial registration, we deployed the deduced affine transformation to the refined maximal projection images from the first phase, proceeding to determine each cell's displacement across sessions. This was achieved by examining image patches centralized on every individual cell for each experimental day, and subsequently computing the spatial cross-correlation functions in a manner analogous to the first step. Our scrutiny revealed that a majority of the cells manifested negligible displacement across days (Figure 5D). For cross-session analysis, we retained only those cells demonstrating day-to-day shifts that were ≤ 3 pixels.

Population decoding capability

We used Uniform Manifold Approximation and Projection (UMAP) algorithm[74] to investigate neuron population decoding capability of 8 orientation s, and compared the difference between population in visual areas and in non-visual areas (Figures 5K and 5L). For all three sessions, we calculated activity amplitude of all responsive neurons (g1-g4, see quantification of neural activities) for all orientation s. Thus, we got a population response matrix of T (trial activity ampitude) × N (neurons). After applying UMAP algorithm, N dimensions were regressed to 2 and each dot represented regressive information of a single trial belonging to a certain orientation (Figure 5K). The clustering efficiency implied population decoding capability. We further calculated clustering efficiency by introducing an index termed 'orientation distance index (ODI)'. ODI is computed through

$$ODI = \frac{CD - \frac{1}{N_{dir}}\sum ICD}{CD + \frac{1}{N_{dir}}\sum ICD} \quad \text{(Equation 18)}$$

where ICD is the Euclidean distance from each direction trial to their centroid, CD is the euclidean distance from each orientation centroid to their centroid, and N_{dir} is 8 as there are 8 orientations in our experiment.

CellPress
OPEN ACCESS

Supplemental figures

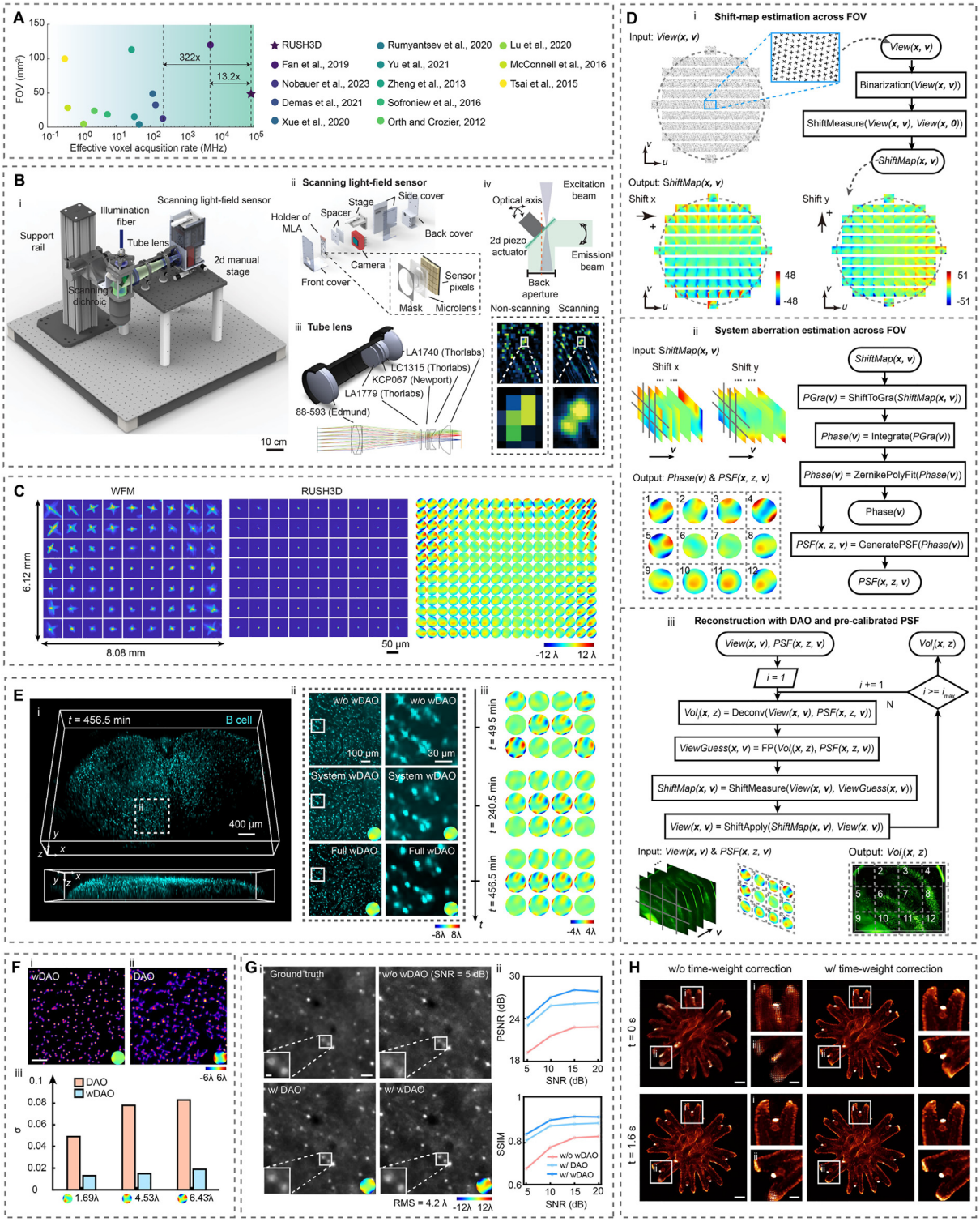

(legend on next page)

Figure S1. Schematic and data processing pipeline of RUSH3D with wDAO, related to Figure 1 and STAR Methods

(A) Comparative analysis of RUSH3D with other mesoscopes in effective voxel acquisition rates (STAR Methods). The acquisition rates were all derived from explicit or displayed parameters in the cited reference paper. The computation of acquisition rates of RUSH3D has considered the differential lateral and axial resolutions throughout the entire depth of field.

(B) Design and assembly of RUSH3D. (i) Overview of RUSH3D system. (ii) Annotated exposure rendering of the scanning light-field sensor. (iii) Annotated rendering of a customized tube lens. The tube lens was made of 5 off-the-shelf components whose vendors are labeled. (iv) Schematics of the scanning of the dichroic mirror. A two-dimensional piezo actuator (P33_T2S, Coremorrow) was centrally positioned on a 50 × 70 mm^2 dichroic mirror (ZT405/488/561/640, Chroma) to manipulate the dichroic for emission beam scanning for scanning light-field detection. The excitation beam was strategically placed off the optical axis of the objective to avoid obstruction by the piezo actuator. Right panel exhibits comparisons of non-scanning (left) and scanning (right) light-field detection.

(C) Characteristics of aberrations across the 8 × 6 mm^2 FOV by showing the maximum intensity projections (MIPs) of 0.5-μm fluorescence beads captured by WFM (left) and RUSH3D (middle). Right, corresponding estimated optical aberrations across the whole FOV in a fine grid.

(D) Processing pipeline of wave-optics digital adaptive optics (wDAO) in RUSH3D. See also STAR Methods in detail.

(E). Aberration correction through wDAO. (i) 3D rendering of inguinal lymph nodes captured by RUSH3D in two perspective views (top and bottom) utilizing wDAO. (ii) Comparison of the white dashed box in (i) among without wDAO (w/o wDAO, top), correction with only system aberrations (system wDAO, middle), and correction with both system and environmental aberrations (full wDAO, bottom). Additional zoom-in panels are exhibited in the right. The estimated full wavefront errors are depicted in the bottom right corner. (iii) Inferred sample aberrations (without system aberration) during imaging the inguinal lymph nodes at three representative time points, at 12 FOV tiles.

(F) Comparisons of wDAO and DAO. (i and ii) Reconstruction of fluorescent beads with wDAO (i) and geometric DAO (ii) under 6λ RMS aberrations in simulation. The residual of estimated wavefront aberrations is exhibited in the bottom right corner. (iii) Residual wavefront errors σ versus different RMS of aberrations under different methods (wDAO and DAO), where σ is calculated through the ratio of the residual phase RMS to the peak-to-valley value of the added aberration.

(G) Quantitative characteristics of imaging quality improvement by wDAO. (i) Simulated neuronal imaging results under 5-dB signal-to-noise ratio (SNR) and 4.2λ wavefront aberrations by different methods, including reconstruction without wDAO (w/o wDAO), reconstruction with DAO (w/DAO), and reconstruction with wDAO (w/ wDAO). Estimated wavefronts are exhibited in the bottom right corners. (ii) Characteristics of peak-signal-to-noise ratio (PSNR, top) and structure similarity index (SSIM, bottom) under different noises (5, 10, 15, and 20 dB) by different methods with 4.2λ wavefront aberrations.

(H) Motion artifacts correction for RUSH3D in jellyfish imaging. Left column: MIPs of a freely moving jellyfish across an FOV of 2.42 × 2.42 × 0.44 mm^3, without any correction (w/o time-weighted correction). The right column exhibits the motion-corrected reconstructions through time-weighted correction. Zoom-in panels are listed.

Scale bars: 50 μm (C, F, and G), 400 μm (i in E), 100 μm (ii in E and zoom-in panel in H), 30 μm (ii in E), 10 μm (zoom-in panel of G), 250 μm (H).

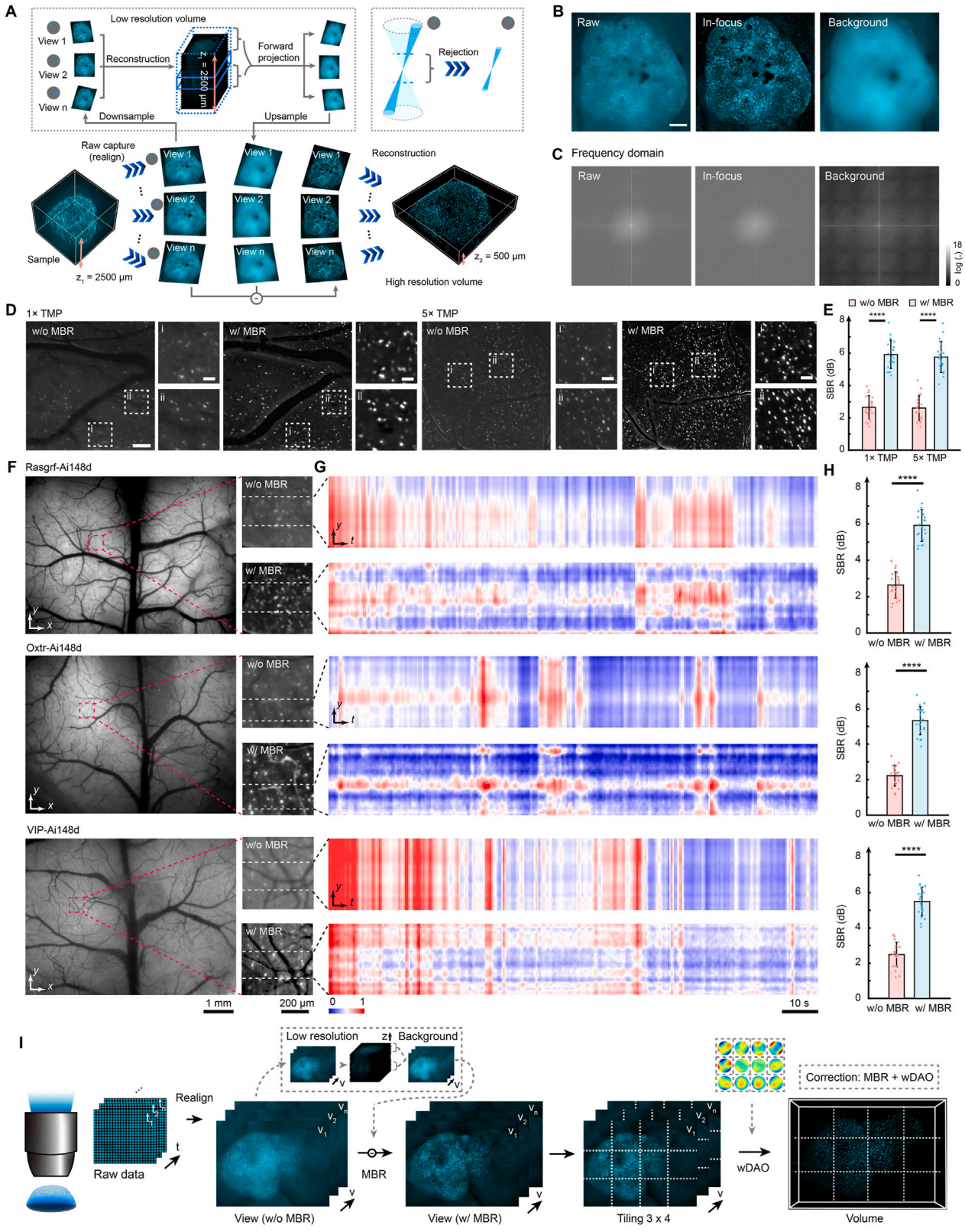

(legend on next page)

Figure S2. Schematic and evaluation of multiscale background rejection in RUSH3D, related to Figures 1 and 2 and STAR Methods

(A) Pipeline illustration of MBR. Different views obtained by RUSH3D are spatially down-sampled (left of upper left box) and engaged in an axially extended reconstruction (middle of upper left box). Within this reconstruction, the background signals are extracted on either side (dashed blue lines in the upper left box), which are later back-propagated into the light-field space, and up-sampled, resulting in background-only views (right of the upper left box). Following this, these background-only views are subtracted from the raw measurement, yielding background rejection.

(B) Examples of MBR left to right, raw center-view without MBR, center view after MBR, and corresponding background signal estimated through MBR.

(C) Spatial spectrums of (B). Color intensities are represented on a logarithmic scale.

(D) Results without MBR (w/o MBR) and with MBR (w/ MBR) over different neuron densities. Rasgrf2-2A-dCre mice (JAX 022864) crossed with Ai148 (TIT2L-GC6f-ICL-tTA2)-D (JAX 030328) transgenic mice were used with two levels of trimethoprim (TMP, 0.25 mg per g [1×] and 1.25 mg per g [5×], respectively).

(E) Statistical characteristics of signal-to-background ratio (SBR) improvements of MBR over different neuron densities. $n = 20$ neurons. Height of bar: mean. Error bar: SD. $^{****}p < 0.0001$, two-sided Wilcoxon rank-sum test.

(F) Evaluation of MBR in calcium imaging over multiple lines of animals. Top to bottom, Rasgrf2-2A-dCre mice (JAX 022864) crossed with Ai148 (TIT2L-GC6f-ICL-tTA2)-D (JAX 030328), expressing GCaMP6f mainly in excitatory neurons of cortical layer-2/3; Oxtr-2A-dCre mice (JAX 031303) crossed with Ai148 (TIT2L-GC6f-ICL-tTA2)-D (JAX 030328) that drives expression in both excitatory and inhibitory neurons in layers 2/3, 4, and 5; Vip-IRES-Cre mice (JAX 031628) crossed with Ai148 (TIT2L-GC6f-ICL-tTA2)-D (JAX 030328), with expression of GCaMP6f in vasoactive intestinal polypeptide (VIP) positive GABAergic interneurons.

(G) Kymograph (y-t plots) comparison of raw captures (top) and MBR-enhanced captures (bottom) in (F).

(H) Statistical characteristics of SBR improvements with MBR over multiple lines of animals. $n = 20$ neurons. Height of bar: mean. Error bar: SD. $^{****}p < 0.0001$, two-sided Wilcoxon rank-sum test.

(I) Schematic of the complete RUSH3D image processing pipeline. Initially, the collected data are realigned into a multi-view format, followed by the execution of MBR processing for background reduction. Subsequently, the image is reconstructed utilizing wDAO.

Scale bars: 500 μm (B), 200 μm (D and zoom-in panels of F), 50 μm (zoom-in panels of D), 1 mm (F).

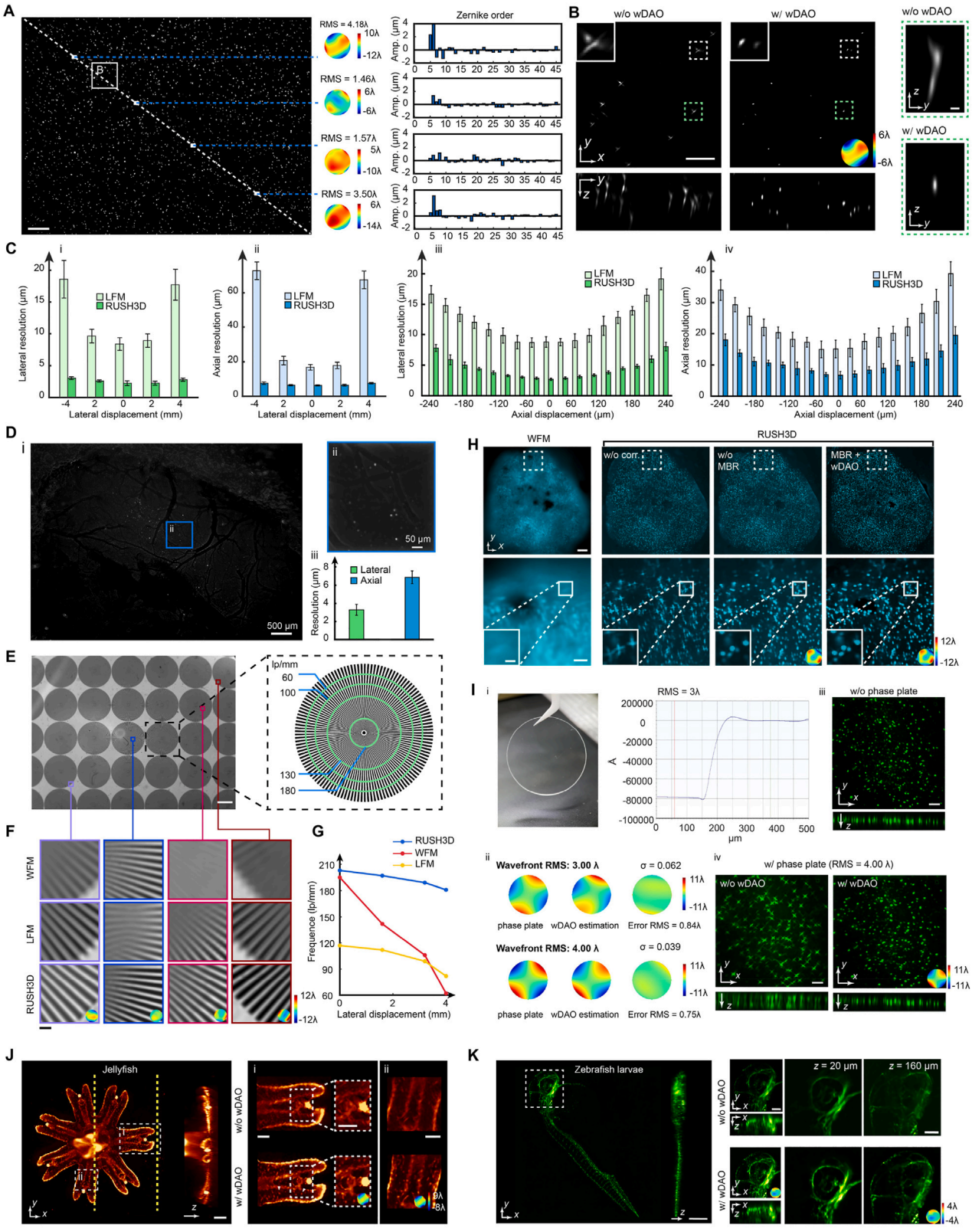

(legend on next page)

Figure S3. Quantitative evaluation of resolution and aberration-correction capability of RUSH3D, related to Figure 2 and STAR Methods

(A) Global resolution characteristics of RUSH3D by imaging 500-nm fluorescence beads. Left: *xy* MIPs. Middle: estimated wavefront aberrations at four positions. Right: Zernike coefficients of the estimated wavefront aberrations.

(B) Comparison of resolution with and without wDAO (w/ DAO and w/o wDAO) of a local region. Left, orthogonal MIPs. Right, yz MIP of a single fluorescence bead obtained by both methods.

(C) Characteristics of lateral resolution (i and iii) and axial resolution (ii and iv) of RUSH3D with comparisons to LFM across lateral displacements (i and ii) and axial displacements (iii and iv). For each site, n = 10 fluorescence beads were randomly chosen for estimation. Gray dashed lines represent the diffraction limit. ***$p < 0.001$, two-sided Wilcoxon rank-sum test. Height of bar: mean. Error bar: SD.

(D) Imaging of the fluorescence beads injected in the mouse cortex surface by RUSH3D *in vivo*. (i) MIP. (ii) Zoom-in panel. (iii) Bar plots of lateral (left) and axial (right) full widths of half maximum over 10 beads. Symbols as in (C).

(E) Characteristics of the modulation transfer function (MTF) of RUSH3D. Left, the Siemens star charts captured by RUSH3D. Right, zoom-in view of a single Siemens star pattern, with different radii representing different spatial frequencies.

(F) Comparisons of the resolution charts imaged by WFM (top), LFM (middle), and RUSH3D (bottom) at different lateral positions. The estimated wavefront aberrations are labeled in the bottom right corner.

(G) Comparison of the attainable spatial frequency of WFM, LFM, and RUSH3D across different lateral positions when the contrast reached 0.3.

(H) Step-by-step enhancement of RUSH3D illustrated by B cells in the inguinal lymph node (GFP labeled, depicted in cyan). From left to right: WFM, RUSH3D without MBR and wDAO (w/o corr.), RUSH3D with wDAO and without MBR (w/o MBR), and RUSH3D with both MBR and wDAO (MBR + wDAO). The second row exhibits the zoom-in panels. Estimated wavefront aberrations are depicted in the bottom right corner. Sample aberration RMS = 2.44λ.

(I) Evaluation of the RUSH3D's aberration-correction capability with customized optical phase plates placed at the pupil plane. (i) Photograph of the customized phase plate via lithography. Two variants are fabricated, one with an RMS wavefront error of 3 wavelengths and the other of 4 wavelengths. (ii) Known phase, estimated phase, and residual phase are exhibited in three columns to show the quantitative assessment of wDAO by imaging with the phase plate over immunostaining brain slices. The estimated phases were derived by subtracting the originally estimated system aberrations. (iii) MIP of the immunostaining brain slice without the phase plate. (iv) MIPs of the immunostaining brain slice with the phase plated obtained without wDAO (w/o wDAO) and with wDAO (w/ wDAO).

(J and K). Orthogonal MIPs and zoom-in slices of freely swimming jellyfish (J) and zebrafish larvae (K) obtained by RUSH3D with and without wDAO.

Scale bars: 500 μm (A and i in D and E), 100 μm (B, I, and zoom-in of J and K), 4 μm (y-z MIP of single fluorescence bead in C), 30 μm (F), 50 μm (ii in D and the second row of K), 300 μm (the first row of H and K), 25 μm (zoom-in panels of the second row of H), and 200 μm (J).

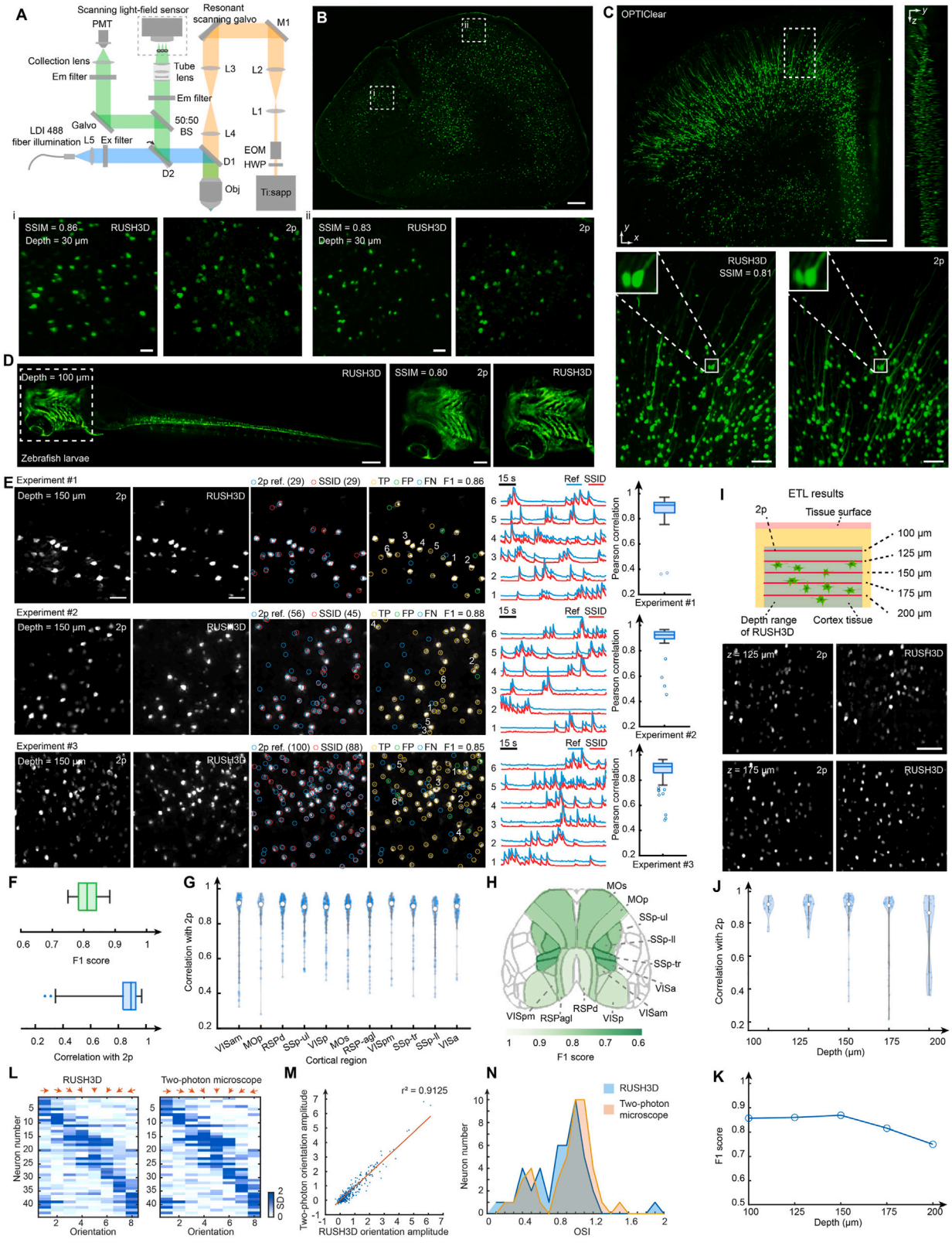

(legend on next page)

Figure S4. Experimental validation of RUSH3D with synchronized two-photon imaging, related to Figure 3 and STAR Methods

(A) Schematic of the hybrid RUSH3D and local two-photon imaging setup used for validation. Ti:Sa, titanium:sapphire laser; HWP, half-wave plate; EOM, electro-optical modulator; L, lens; M, mirror; D, dichroic mirror; BS, beam splitter; Em filter, emission filter; Ex filter, excitation filter. The D1 dichroic (DMLP650L) separates photon excitation beam with two-photon excited fluorescent photons, RUSH3D excitation, and RUSH3D emission photons. The D2 dichroic (DMLP505L, Thorlabs) for GFP detection is attached to the RUSH3D piezo scanner.

(B–D) Validation of RUSH3D with two-photon ground truth by imaging the same immunostaining brain slice (C), cleared brain (B), and *in vivo* zebrafish larvae (D). Multiple zoom-in panels are exhibited for comparisons. The structure similarity index (SSIM) is labeled using two-photon data as ground truth.

(E) Evaluation of neuronal imaging fidelity of RUSH3D with functional ground truth obtained by two-photon microscopy. Simultaneously captured two-photon and RUSH3D images are presented in the first two columns. The third column exhibits overlaid neuron segments in two-photon (red) and RUSH3D (processed by SSID, blue). The fourth column further exhibits segments of true positives (TP, yellow), false negatives (FN), and false positives (FP). The fifth column presents randomly selected calcium traces by two-photon microscope (red) and RUSH3D (processed by SSID, blue). The two-photon traces are intentionally shifted for clarity. The sixth column presents boxplots of correlation scores between two-photon microscopy and RUSH3D. Central line inside the box: median. Box: interquartile range. Whiskers: maximum and minimum. Outliers: individual data points. n = 3 recordings across 3 brain positions are presented in 3 rows.

(F) Neuronal detection F1 score (top) and correlation score (bottom) of RUSH3D compared with two-photon ground truth data across 3 animals and 3 imaging sessions. Boxplot symbols as in (E).

(G) Neuronal correlation scores of RUSH3D compared with two-photon ground truth data in different cortical regions. White circle: median. Thick gray vertical line: interquartile range. Thin vertical lines: upper and lower proximal values. Transparent disks: data points. Transparent violin-shaped areas: kernel density estimate of data distribution.

(H) Distribution of neuronal-detection capability of RUSH3D indicated by F1 scores in Allen CCF brain atlas.

(I) Illustration of experiment to validate neuronal-detection ability of RUSH3D across different cortical depths. The two-photon detection plane was shifted using an electrically tunable lens, while RUSH3D detection volume remained stationary. Two representative depths (out of a total of five) are displayed, including the standard deviation plots of interleaved recordings from two-photon microscope and RUSH3D, respectively.

(J) Evaluation of neuronal correlation scores achieved by RUSH3D at different cortical depths. Violin plot symbols as in (G).

(K) Evaluation of neuron-detection accuracy (F1 scores) achieved by RUSH3D at different cortical depths.

(L) Heatmap of stimuli-evoked activity for paired visual-tuned neurons by RUSH3D (left) and two-photon microscope (right).

(M) Scatterplot of orientation amplitude between RUSH3D and two-photon microscope, calculated from the averaged stimulus-evoked activities over preferred orientation. The thick red line represents the linear regression, with r^2 = 0.9125.

(N) Orientation selection index histogram acquired by two-photon (red) and RUSH3D (blue).

Scale bars: 500 μm in (B and C), 100 μm in (I and zoom-in panel of C and D), 200 μm in (D), 50 μm (E and zoom-in panel of B).

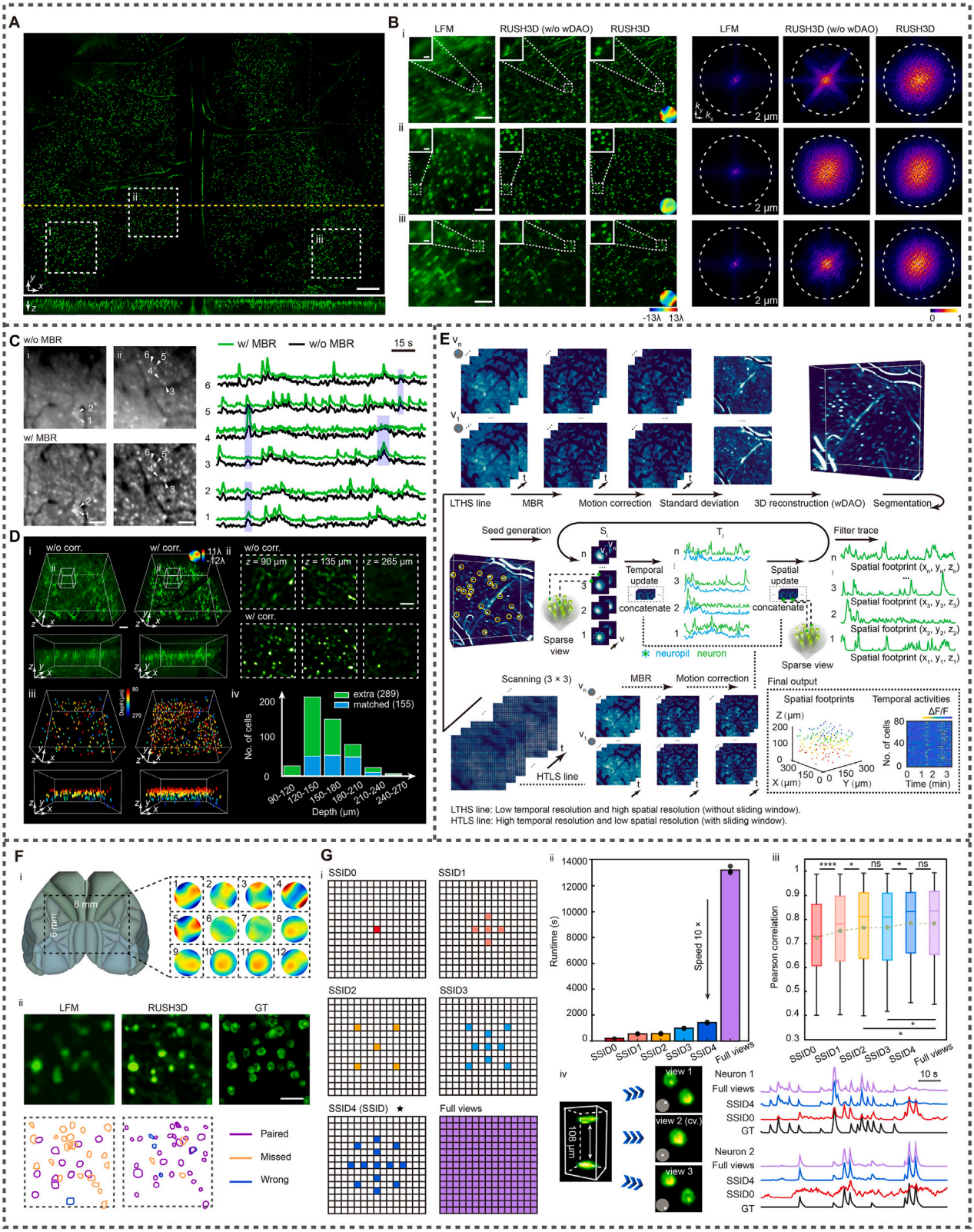

(legend on next page)

Figure S5. Efficient high-fidelity large-scale 3D neuronal extraction with RUSH3D, related to Figure 3 and STAR Methods

(A) Orthogonal MIP of the standard deviation of 2,000 frames of calcium imaging in mouse cortex obtained by RUSH3D.

(B) Three zoom-in regions marked in (A) obtained by LFM, RUSH3D without wDAO (w/o wDAO), and RUSH3D with wDAO. Estimated wavefront aberrations are exhibited in the bottom right corner. Right, spatial spectrum of corresponding left panels. White dashed circles represent the spatial frequency of 2 μm.

(C) Comparisons of reconstructions without MBR (w/o MBR, top) and with MBR (w/ MBR, bottom) in two positions. Right, visualization of MBR enhancement in exemplary neurons marked in by white arrows. Green lines for MBR-enhanced traces and black lines for raw traces. MBR traces are intentionally shifted for better visualization. Blue shadows indicate the elimination of crosstalk.

(D) wDAO and MBR improve neuronal segmentation and activity inference. (i) Comparison of 3D reconstructions without correction (w/o corr., without applying wDAO and MBR, left) and with correction (w/ corr., applying wDAO and MBR, right). (ii) Comparison of reconstructed slices at different depths (90, 135, and 265 μm) without correction (first row) and with correction (second row) in a patch outlined by the white dashed box in (i). (iii) Comparison of neuron segmentation on reconstructions without (left) and with correction (right). Segmented neurons are represented by ellipsoids with colors coded by depths. (iv) Histogram of neuron detection across varied imaging depths. Blue (matched) denotes neurons identified in both corrected and uncorrected reconstructions. Green (extra) represents neurons exclusively identified in corrected reconstructions.

(E) Illustration of the SSID workflow in two segments: initial seed generation and ensuing iterative demixing.

(F) Evaluation of wDAO through NAOMi simulator. (i) Simulated wavefront aberrations across the whole FOV of 8 mm × 6 mm. (ii). Comparison of reconstructions through LFM (left) and RUSH3D (middle) against the ground truth (right). Segmentation of SID in LFM (left) and proposed SSID in RUSH3D (middle) are exhibited in the second row. The purple circle marks the paired segments with the ground truth, the yellow circle marks the missed segments, and the blue circle marks the wrong segments.

(G) Quantitative evaluation of calcium extraction ability of SSID with different numbers of views used. (i) Illustration of the sparse iteration in SSID. The 15 × 15 grids represent 15 × 15 views of RUSH3D. SSID optimized the patterns of view utilization to minimize computing costs while preserving high-temporal fidelity. SSID4 pattern (marked by a star) was chosen in this work. (ii and iii). Quantitative evaluation of computing time (ii) and temporal fidelity (iii) of SSID with different view patterns used. $n = 3$ movies. $^{*}p < 0.05$, $^{***}p < 0.001$, ns, not significant. Two-sided Wilcoxon rank-sum test. (iv) Left, a pair of representative neurons that are largely overlapped in x-y plane but separated in y-z plane. As a result, these two neurons are separated in views 1 and 3 (marginal views) but overlapped in view 2 (the central view [cv.]). Right, recovered neuronal signals of these two neurons through various view pattern setups.

Scale bars: 500 μm (A), 200 μm (zoom-in panel of i, ii, and iii in B), 100 μm (C), 50 μm (i and ii in D), and 20 μm (ii in F).

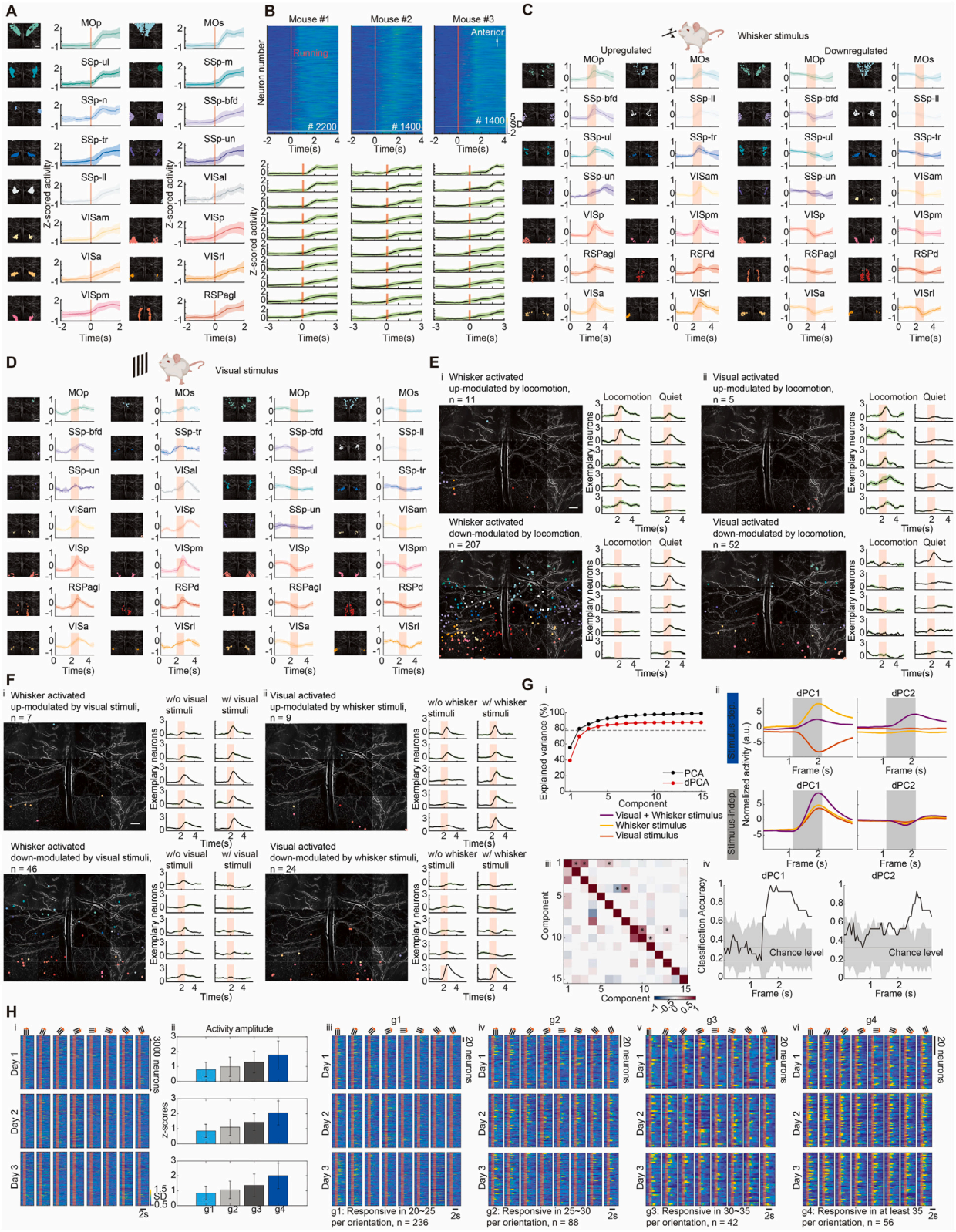

(legend on next page)

Figure S6. Large-scale neural responses during preparatory processing, multisensory input, and cross-day visual representational drift, related to Figures 4 and 5

(A) Distribution of locomotion up-modulated neurons in selected cortical areas (left) and the corresponding average neural activities (right). Red lines indicate the onset of locomotion. Thick line: mean. Error bar: SD of neural activity.

(B) Activity of locomotion up-modulated neurons during state transition for 3 mice. Upper: *Z* scored activity of up-modulated neurons. Neurons are sorted by anterior-posterior (A-P) positions. Red lines indicate the onset of locomotion. Bottom: average activity of neurons from 10 A-P bins.

(C) Distribution of whisker stimulus upregulated (left) and downregulated (right) neurons in different cortical areas and the corresponding average neuron activity. Shaded red rectangles mark the stimulus epoch. Other symbols as (A).

(D) Same as (C), but for visual stimulus-evoked neurons.

(E) Stimulus-evoked neuronal activities regulated by motion. (i) Distribution of whisker stimulus-evoked neurons that were up-modulated (top) or down-modulated (bottom) by locomotion. The neurons were selected by Wilcoxon signed rank test with a significance $p < 0.05$. Right: neuronal activities of 5 representative stimulus-evoked neurons. The red shaded bar indicates a fixed period of running or stationary states (1 s). Other symbols as (A). (ii) Same as (i), but for visual stimulus-evoked neurons that were regulated by running.

(F) Stimulus-evoked neuronal activities regulated by multisensory interaction. (i) Distribution of whisker stimulus-evoked neurons that were up-modulated or down-modulated by simultaneous visual stimulus. The neurons were selected by Wilcoxon signed rank test with a significance $p < 0.05$. Right: neuronal activities of 5 representative stimulus-evoked neurons. The red shaded bar indicates the period of visual stimulus. Other symbols as (A). (ii) Same as (i), but for visual stimulus-evoked neurons regulated by simultaneous whisker stimulus.

(G) Demixed principal-component analysis (dPCA) analysis of neuronal responses to whisker and visual stimulus in various cortical areas. (i) Cumulative variance explained by PCA and dPCA components. The dashed line marks the fraction of signal variance. (ii) Demixed principal components (dPCs). In each subplot, there are 3 lines corresponding to 3 conditions. Shadows mark the stimulus onset. (iii) Upper-right triangle shows dot products between all pairs of the first 15 demixed principal axes, bottom-left triangle shows correlations between all pairs of the first 15 demixed principal components. (iv) Cross-validated time-dependent classification accuracies of linear classifiers (black lines) given by the first two stimulus dPCs (columns). The classifiers were trained to classify 3 stimuli conditions (visual stimulus, whisker stimulus, and visual + whisker stimulus). Shaded gray regions show the distribution of classification accuracies expected by chance as estimated by 100 iterations of the shuffling procedure.

(H) Characteristics of neuronal activity in response to moving grating stimuli across days. (i) Heatmap of trial-averaged activities in 3 consecutive days. The shaded red bars mark the period of visual stimuli. Fluorescence change scaled for clarity. SD, standard deviation. (ii) *Z* scored activity amplitude of 4 groups (g1–g4, STAR Methods) of neurons across 3 consecutive days. Height of bar: mean. Error bar: SD. (iii–vi) Heatmap of trial-averaged activity for the 4 groups of neurons. Same format as in (i).

Scale bars: 1,000 μm in (A, C, and D), 500 μm in (E and F), 20 neurons (H iii–vi), 2 s (H iii–vi).

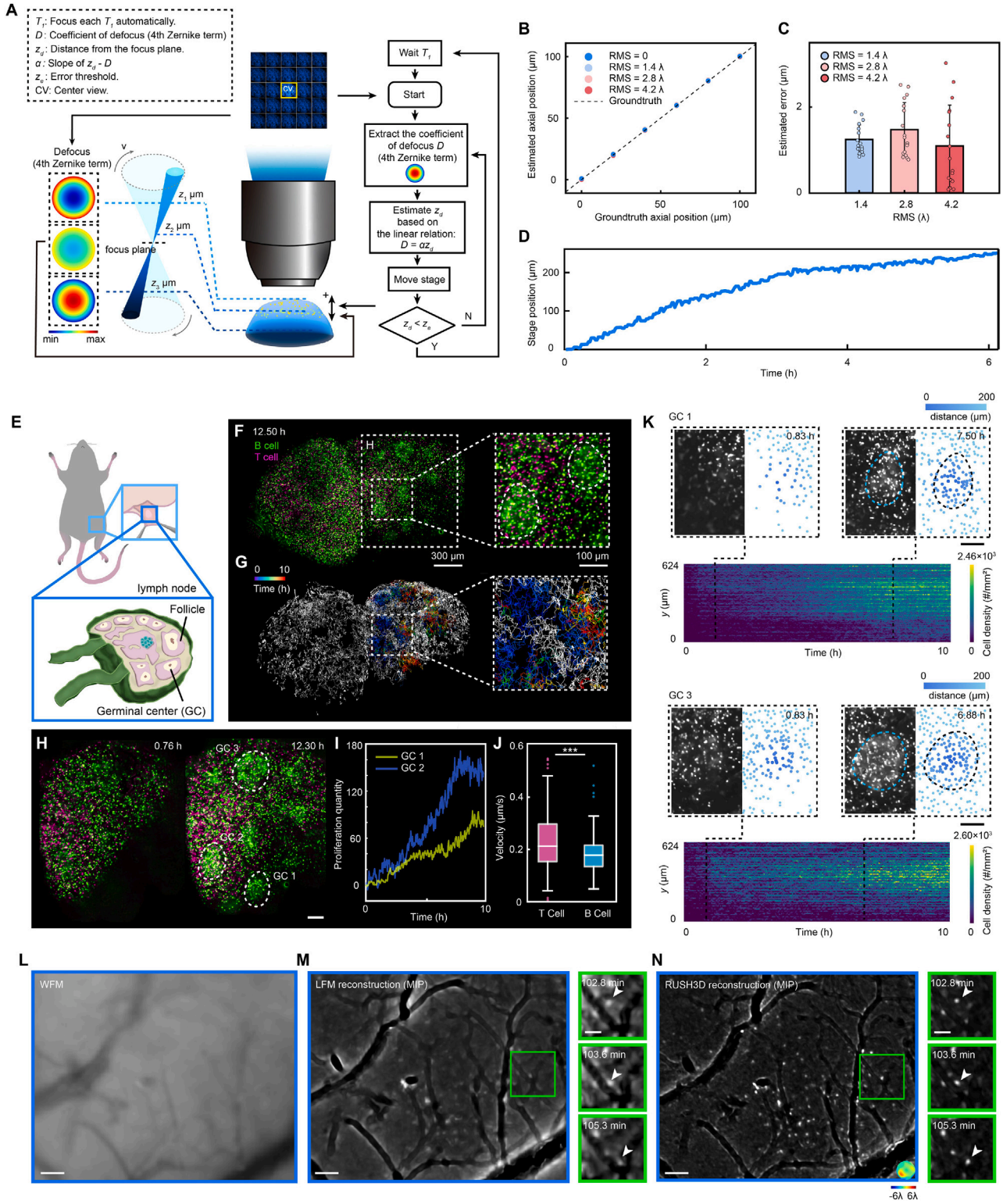

Figure S7. Large-scale 3D monitoring of immune cells at the organ scale with automatic focus by RUSH3D, related to Figures 6 and 7

(A) Illustration of the automatic-focus module in RUSH3D with feedback control of the sample stage based on the estimated defocus distances based on the light-field measurements.

(B) Characteristics of the accuracy of focus position estimation across 100-μm range under various wavefront aberrations.

(legend continued on next page)

(C) Bar plots of focus estimation error under different aberrations. The average focal estimation error is less than 4 μm when RMS of wavefront aberration ranges within 4.2λ.
(D) Stage movements over 6-h continuous imaging of lymph node with auto-focus.
(E) Illustration of the inguinal lymph node structure within a murine model.
(F) MIP of the lymph nodes by RUSH3D, discerned after a continuous 12.5-h recording, with both B cell and T cell labeling. A zoom-in panel (indicated by the small white dashed enclosure) is displayed on the right.
(G) Trajectories of tracked B cells. The white lines represent the trajectories of cells that do not flow over a germinal center (GC). Other trajectories are temporally coded with different colors. The same zoom-in region as in (F) is exhibited in the right.
(H) Inspection of GC formation in a zoom-in region (marked by the large white dashed box in F) at different time points (left and right).
(I) Characteristics of cell proliferation quantity in two GCs. The GC regions are outlined by white dashed lines in (H).
(J) Characteristics of cell flow speed of tracked T cells and B cells flow over GC 2. n = 204 B cells and n = 253 T cells are tracked. Central line inside the box: median. Box: interquartile range. Whiskers: maximum and minimum. Outliers: individual data points. ***$p < 0.001$, two-sided Wilcoxon rank-sum test.
(K) Illustration of B cell clustering during the formation of GCs. The kymography of selected ROIs (GC 1 and GC 3 in H) is plotted at the bottom, and cell distributions at two time points are enlarged at the top. The dots are distance (from GC center) coded with different colors. For each time point of each GC, the left panel in the top represents the MIP of the GC (marked by cyan dashed lines), and the right panel in the top represents the segmentation and GC area marked by black dashed lines.
(L–N). Comparisons of MIP obtained by WFM (L), LFM (M), and RUSH3D (N) of neutrophils in mouse brain with the TIS window. All microscopes have the same objective with NA 0.5. Zoom-in views are displayed for detailed comparisons. Estimated wavefront aberrations are marked at the bottom. Scale bars: 300 μm (F) and 100 μm (H, K, and zoom-in panel of F and L–N), and 50 μm (zoom-in panel of M and N).